Enhancing Portability, Modularity, and Optode Density in Translational Diffuse Optical Imaging

A Dissertation Presented
by

Morris Dwight Vanegas

to

The Department of Bioengineering

in partial fulfillment of the requirements
for the degree of

Doctor of Philosophy

in

Bioengineering

Northeastern University
Boston, Massachusetts

December 2022

ABSTRACT

Enhancing Portability, Modularity, and Optode Density in Translational Diffuse Optical Imaging

by

Morris Dwight Vanegas

Doctor of Philosophy in Bioengineering

Northeastern University, December 2022

Dr. Qianqian Fang, Adviser

The use of diffuse optical imaging (DOI) in medical applications is growing at a rapid pace due to its non-invasive, non-ionizing, and potentially portable nature. DOI's ability to provide functional assessments in various areas of the body has accelerated our ability to diagnose malignant breast lesions and measure brain functions. Some of these accomplishments have been achieved through the use of highly-sensitive and bulky equipment that, unfortunately, has made these systems complex to build, costly to maintain, and difficult to transport. Additionally, the large number of individual sources and detectors needed not only make each measurement time-consuming but also introduces coupling variations that make data analysis difficult. Designing increasingly powerful, versatile, and at the same time, sophisticated optical imaging systems requires careful consideration of numerous trade-offs between multiple competing factors, including fabrication, ergonomic, environmental, safety, usability, mechanical, and data communication considerations. Recently, in order to scale the application of near-infrared (NIR) optical imaging, the field has trended towards architectural designs that allow for both faster acquisition times and use in naturalistic environments. In this dissertation, we investigate and further advance a number of emerging DOI instrument design methodologies to tackle a series of challenges in the clinical translation of DOI. These include

the design of low-cost and ultra-portable mobile-phone-based spectroscopic tools to facilitate disease diagnosis in resource-poor regions, a modular and wearable optical brain imaging system for understanding brain functions in natural settings, and a wide-field high-density optical breast imaging system for cancer diagnosis. We leverage innovations in computational methods, advanced electronic sensors, and ubiquitous devices to demonstrate the potentially broad application of NIR imaging across populations and settings. We particularly focus our intent on the scalability of diffuse optical imaging through improving architectural attributes such as portability, modularity, and optode density to provide real-life examples of ways to address the current challenges of developing, evaluating, and optimizing portable high-performance DOI systems.

To my future self.

Enlightenment was and is formed by a desire to grasp the abstract.

ACKNOWLEDGEMENTS

If you want to go fast, go alone; if you want to go far, go together.

African proverb

This doctoral journey has been a far one. Although a Ph.D. degree is supposed to test your ability to be an independent researcher, it would be naive to think this journey was made without support. I am indebted to so many wonderful souls that intentionally (and unintentionally) crossed paths with me during this journey of mine.

My first debt of gratitude goes to my advisor, Dr. Qianqian Fang. My journey has been filled with both academic and personal challenges and he has been immensely accommodating and supportive to both. From painstakingly reading every one of my manuscripts to pair programming with me, his attention to detail is unmatched. Notably, he has done a fantastic job allowing me to be a beginner, beautifully balancing when to strongly suggest advice and when to let me struggle in the name of growth. Despite his technological arbitrage, he also demonstrated a sincere amount of empathy when it seemed that the universe's goal was to bombard me with personal challenges to prevent the completion of this work. For this, for letting me explore, and for constantly helping me pivot, I need to say that I appreciate you. Thank you, Qianqian Fang. Truly.

My two other committee members also deserve much praise. Dr. Mark Niedre has been part of this process ever since my qualification exam. I thank you for your guidance, lectures, and incredibly valuable suggestions to address my challenges. Your down-to-earth attitude made you incredibly easy to talk to. I'd also like to thank Dr. Meryem Yücel. Though our interactions were limited, they were impactful. From participating in your workshops at MGH to seeing you present at fNIRS conferences, your approach, talent, and intellect are something to be praised. Thanks for being an example for me to attempt to emulate.

A very special thanks to Dr. Stefan Carp, whom I met early in my Ph.D. journey, and who collaborated with me on all three of my major projects for this work—your vast technical capabilities and experience saved me hours of research. You have a rare gift to be able to make the most complex concepts easily digestible. I must also acknowledge Dr. Jeffrey Ruberti for providing guidance, re-framing, and reality checks in a way that makes you want to improve the world around you. Thanks for being a great mentor.

I also hold lots of gratitude towards my lab mates, who made this highly independent experience a social one. Dinners, outings, and analyzing World Cup matches made this journey much more enjoyable. A special thanks to my lab mate, Edward Xu, for acquiring and providing me with subject data for the OMCI section of my dissertation. Additionally, I'd also like to highlight Dr. Miguel Mireles Nuñez, a post-doc in my lab who brought an immense amount of knowledge and diligence to anything he worked on. You taught me that success is where opportunity meets preparation.

A special thanks needs to be reserved for the motley crew of innovators that make up the diffuse optics community in the Greater Boston area. They include the great minds at Boston University, the MIT Media Lab, and the Martinos Center at MGH. These researchers have taught, challenged, and collaborated with me. I appreciate having a community composed of people who are driven by the curiosity and the beauty of the subject itself. Similarly, a heart-filled thanks goes out to all the patients in these centers that volunteered their time and themselves to my pilot studies in the name of science. Additionally, I've been fortunate and blessed to have all my work funded, a rarity in this day and age. Thank you to the Bill and Melinda Gates Foundation, the National Institutes of Health (NIH) National Cancer Institute, and the NIH BRAIN Initiative for funding these ideas. I'm humbled to have had the opportunity to turn my thoughts into tangible contributions.

I'd also like to thank the unsung heroes that I am sure are part of everyone's Ph.D. journey. The local baristas, knowledgeable librarians, concerned campus police that safely escorted me on snowy nights, local museums that let me mindfully wander, and the army of bus and train conductors that got me to and from the lab year-round. Thank you.

Outside of the academic circles, there are special groups of people that not only helped with but also witnessed my Ph.D. journey. These groups taught me that classes should never get in the way of my education. They have now become friends, mentors, advisors and advisees, and the best people to dream big with. Thank you to the lifelong connections I've made at TDC Theta Deuteron. I will never find a better set of daydreamers and night thinkers. A huge thanks to my

Dent The Future community who never allowed my growth to stagnate by constantly exposing me to new people and experiences. It is a rare find to have a community excited by bold ideas, not just academic hierarchy. And of course, a thank you to the members of RisOn, who help me thrive, self-reflect, and challenge me to continually question whether I am using my influence in the most positive impactful way.

And then there is family. Thanks to my parents—my tenacious, tireless cheerleaders. Thank you to my dad, Rene, from whom I inherited receptivity, curiosity, and patience. And thank you to my mom, Maria, who taught me to be "suficientemente desmadroso," a trait that was surprisingly useful in pushing the boundaries of science. To my sister, Pamela, and brother-in-law, Hugo, thank you for keeping my spirits up with pictures of my nieces and nephews and for cooking the most amazing holiday dinners imaginable. Those emotional anchors got me through some very frustrating times. A very special "woof" to the good girl that is my dog, Chuli. Rain, shine, or snow, she never hesitated to go for a run with me to help maintain my sanity. A special thanks to the hipsters, hustlers, and hackers at heart that is my wife's Cuban family. Their laughter and energy have taught me to dance through any of life's storms. Also, I'd like to thank Christopher Jesus Gonzalez and Catherine Michelle Peña for visiting, hosting, and letting me feed off of their passions. You two entertained my thoughts, ramblings, and complaints. I appreciate being able to share stories of our journeys into professional realms where advice from those that look like us is limited.

And finally, to my wife, Jessica. I've learned enough from you for 10 whole Ph.D. degrees! Few people can learn as deeply and think as widely as you do. No ambition has ever been too lofty and no goal too high in your eyes. You have encouraged me to follow my heart and feed my soul throughout this journey. You taught me to be a true explorer—someone that investigates hard what truly interests them in the most artistic, playful, and original way possible. Thank you for letting me explore this world with you.

TABLE OF CONTENTS

LIST OF FIGURES

LIST OF TABLES

LIST OF ACRONYMS

AC alternating current

ADC analog-to-digital converter.

AFE4490 analog front-end.

CCD charge-coupled device.

CMOS complementary metal-oxide semiconductor.

CSF cerebral spinal fluid.

CT computed tomography.

CW continuous-wave.

DAC digital-to-analog converter.

DBT digital breast tomosynthesis.

DC direct current.

DE diffusion equation.

DICOM Digital Imaging and Communications in Medicine.

DOI diffuse optical imaging.

DOS diffuse optical spectroscopy.

DOT diffuse optical tomography.

EEG electroencephalogram.

EM extrusion multiplier.

EMCCD electron-multiplying charge-coupled device.

EVM evaluation module.

FD frequency-domain.

FDM fused-deposition modeling.

fMRI functional magnetic resonance imaging.

fNIRS functional near-infrared spectroscopy.

FPC flexible printed circuit.

GM gray matter.

GPU graphical processing unit.

GUI graphical user interface.

HbO oxygenated hemoglobin.

HbR de-oxygenated hemoglobin.

HbT total hemoglobin.

HR heart rate.

HRF hemodynamic response function.

I^2C inter-integrated circuit.

IMU inertial measurement unit.

IR infrared.

IRB Institutional Review Board.

ISP in-service programmer.

JST Japan Solderless Terminal.

LASER Light Amplification by Stimulated Emission of Radiation.

LED light emitting diodes.

LMIC low- and middle-income countries.

MBLL modified Beer-Lambert law.

MC Monte Carlo.

MCX Monte Carlo eXtreme.

MEG magnetoencephalography.

MGH Massachusetts General Hospital.

MOBI Modular Optical Brain Imager.

MOCA Modular Optode Configuration Analyzer.

MOXI Mobile-phone-based Oximeter.

MRI magnetic resonance imaging.

MSE mean squared error.

NIR near-infrared.

NIRS near-infrared spectroscopy.

OMCI Optical Mammography Co-Imager.

OD optical density.

P2P peer-to-peer.

PCB printed circuit board.

PET positron emission tomography.

PETG polyethylene terephthalate glycol.

PLA polylactic acid.

POC point-of-care.

PPG photoplethysmogram.

PTFE polytetrafluoroethylene.

PW path width.

PWM pulse-width modulation.

RF radio frequency.

ROI region-of-interest.

RR ratio-of-ratio.

RTE radiative transfer equation.

SD source-detector.

SDS source-to-detector separation.

SLI structured-light illumination.

SMG spatial multiplexing group.

SMR spatial multiplexing ratio.

SNIRF Shared Near Infrared Spectroscopy Format.

SNR signal-to-noise ratio.

SPECT single-photon emission computerized tomography.

SPI serial-peripheral interface.

SO_2 blood oxygen saturation.

SpO_2 peripheral blood oxygen saturation.

SS short-separation.

STL standard tessellation language.

StO_2 tissue oxygen saturation.

TCGA The Cancer Genome Atlas.

TTL transistor-transistor logic.

USB universal serial bus.

WF wide-field.

WM white matter.

CHAPTER 1

Introduction

Modern medical imaging has made a profound and transformative impact on clinical diagnosis, monitoring, and treatment of diseases [1]. It has served as an invaluable research tool to advance our knowledge of human physiology, disease pathology, and intervention methods. X-ray radiography [2], one of the first medical imaging modalities, continues to play an important role in today's cancer screening, diagnosis, and surgical guidance. However, its intrinsic limitations, such as the use of ionizing radiations and morphology-centered imaging contrasts, have also been widely recognized. For example, in the field of breast cancer imaging, the overlapping tissues resulting from x-ray-based mammography scans obscure the diagnosis of small and early-stage cancers [3], resulting in both missed cancer diagnoses and a high rate of false-positives. Despite exciting progress made in recent years, including significantly lowered radiation dose due to the use of iterative image reconstruction methods [4] and dual-energy techniques [5], structure-oriented x-ray imaging continues finding its hindrance in meeting emerging medical needs. Using breast imaging as an example, the rapid emergence and maturity of digital breast tomosynthesis (DBT), which employs multiple low-dose x-ray scans to produce a volumetric rendering of the breast [6], has shown promise in enhancing breast cancer diagnosis. Its lack of functional assessment motivates researchers to continue the journey of seeking safe, low-cost, functional, and portable alternatives.

The advancement of the medical imaging field has accelerated due in part to the increasing availability of relatively inexpensive computational resources [7]. In this process, we have witnessed successful clinical translations and expanded utilities of alternative imaging technologies such as nuclear medicine [positron emission tomography (PET) and single-photon emission computerized tomography (SPECT)], ultrasound imaging, and magnetic resonance imaging (MRI) [8]. Nuclear medicine relies on the detection of injected radioactive isotopes that attach to biochemi-

cally active substances in the body [9]. Similar to computed tomography (CT), nuclear medicine can generate 3-D images from a series of slices through multiple projection views. MRI is also non-ionizing, using high-field magnets to obtain tissue information from changing spin properties of subatomic particles [10]. It is one of the most versatile modalities as its scanning sequence can be "programmed" to obtain a wealth of tissue-related information, achieving spectroscopic, diffusion, and dynamic scans using the same instrument. Its capability can be further expanded when used in combination with dynamic contrast agents. Ultrasound imaging uses high-frequency sound waves that are reflected back due to different acoustic impedances of tissues and collected to form an image [11]. Not only is it highly portable, but its sound-based technology makes it particularly useful for imaging structures in motion. These contemporary imaging modalities have improved on the traditional approach of x-ray imaging, and thus, have begun taking center stage in routine clinical use more frequently.

Despite their contributions, each of our modern-day diagnostic approaches still possess some disadvantages. For example, despite working with low doses, the largest man-made source of radiation exposure comes from radiation due to medical examinations [12]. Nuclear medicine exposes patients to small radiation doses which limits its use for specific subject populations, such as pregnant women. MRI systems are relatively expensive, and require the subject to be immobile during scanning. Such limitations hinder its broad access and utilities in many practical investigations. Despite being able to image internal organs and soft tissue, ultrasound's image quality is greatly affected by the degradation of signals at deep imaging depths as well as by the highly sound-reflective bones [13]. Its difficulty with anatomical and orientation information makes ultrasound imaging heavily dependent on the experience of the user, calling into question its diagnostic accuracy [14]. To address the high cost, bulky, and in some cases, invasive nature of modern imaging techniques, the imaging community has started paying increasing attention to diffuse-optics-based imaging and spectroscopy techniques in recent decades.

Diffuse optical imaging (DOI) is a non-invasive, non-ionizing method that uses visible and near-infrared (NIR) light to probe the molecular function of deep (over a few centimeters) tissues [15, 16], as opposed to various microscopy techniques that probe tissues at shallow depths (less than hundreds of microns). Although some optical imaging methods use exogenous contrast agents (such as fluorescence and phosphorescence imaging [17]), in this dissertation, we specifically focus on non-invasive DOI techniques that target intrinsic (endogenous) tissue contrasts [18]. Optical imaging can be used for both spectroscopic and tomographic measurements, providing unique functional contrasts, such as oxy-hemoglobin, deoxy-hemoglobin, and metabolism in terms of oxygen

saturation, that complement the capabilities of other more established modalities. Despite its advantages, DOI instruments face a number of unique challenges as the community continues advancing its clinical translation and addressing emerging needs. The relatively bulky-size, high manufacture cost, and lengthy measurement time of contemporary DOI instrument designs are among the top of such challenges.

Just like advances in computational methods made modeling the complex interactions between light and tissue a simpler task, we must now further explore emerging aspects of imaging system architectures to properly scale the advantages of DOI. While it is well agreed upon that conventional imaging techniques have fundamentally improved our understanding of human brain functions [19], certain patterns and dynamics are only apparent when measured in natural environments [20]. Thus, recent advances in optical imaging have focused on wearability to directly address the limitation of immobility during use of traditional techniques [21, 22]. Similarly, trends towards highly portable systems have led the community to adopt modular architectural designs made of repeating elementary optical modules [23, 24, 25]. These modular architectures not only lower fabrication costs but also facilitate the design of long-term wearable systems, allowing researchers to investigate broader paradigms in unrestricted environments. Finally, the inherent disadvantage of low spatial resolution of DOI systems, caused largely by the high scattering properties of biological tissues [16], has been recently addressed through wide-field illumination and fast detection strategies that enable tomographic imaging of large tissue volumes at high acquisition speeds [26, 27, 28]. Investigating how to improve on these three architectural attributes—portability, modularity, and optode density—can further advance our understanding of ourselves by allowing us to expand past the limited types of stimuli and interactions currently imposed on us by contemporary DOI systems [20].

This dissertation will show the potential of DOI to address a variety of current application, user, and setting-specific challenges through the development of multiple imaging systems. The first challenge is raised by the global health community to address the heightened high-risk period for babies from the onset of labor through 48 hours after birth in low- and middle-income countriess (LMICs), which accounts for 54% of neonatal deaths annually [29]. Developing portable, miniaturized low-cost spectroscopy methods that can be used in conjunction with a mobile phone could offer life-saving diagnostic tools for front-line clinicians in many resource-poor regions. For the second challenge, we turn toward the brain. Nearly all of our current knowledge about human brain functions was characterized using immobile imaging scanners in a lab environment; these lab settings are drastically different from the free environment outside of the lab, where humans spend

the most time interacting with each other. To study human brains in natural environments, we have to design lightweight and mobile imaging systems that can be worn and carried by the subject; they also need to offer flexibility to probe different brain regions over different, or even multiple, subjects. In this dissertation, we will develop a wearable optical neuroimaging system with features tailored toward use in naturalistic environments. And finally, we will address the challenge of improving breast cancer diagnosis through the development of an optical mammography system that augments existing x-ray mammography systems and scans. In this work, we will explore implementations of architectural attributes to make imaging and spectroscopy systems suited to address all three aforementioned challenges.

The three imaging systems described in this dissertation will vary in attributes of portability, modularity, and optode density. To address the challenges above, some systems we design will leverage computational improvements of light propagation models while other systems will integrate technological advancements in sensors to improve existing techniques. In all systems, we will take a translation-focused lens to ensure what we are building is addressing the needs of users. By demonstrating use cases and designs across a variety of medical imaging attributes, we hope to help the medical community at large address challenges of non-invasive DOI methodologies and demonstrate ways to translate and scale these technologies outside of research settings.

This dissertation is separated into five high-level aims. The first three aims refer to the development of three individual portable and/or wearable near-infrared imaging systems. We will present the design, fabrication, and characterization of these systems as well as measurements on human test subjects. The fourth and fifth aims refer to frameworks and workflows developed to facilitate the analysis of complex modular-architecture-based systems [30] and build repeatable phantoms for the validation of new DOI systems. While this introductory chapter sets the challenge and scope of the research for this dissertation, Chapter 2 gives necessary background into the basics of optical imaging and details the imaging techniques used in this work. Chapter 3 shows how we address the first challenge through the development of a mobile-phone-based pulse oximeter that leverages the sensors inside already ubiquitous mobile phones in LMICs. The second challenge of advancing neuroimaging is separated into two chapters detailing software and hardware solutions. We first describe a software workflow that helps design new modular-architecture-based functional near-infrared spectroscopy (fNIRS) systems (Chapter 4) before describing the hardware development of a wearable functional brain imaging system with features tailored towards its use in natural, unrestricted environments (Chapter 5). The third challenge is addressed in Chapter 6. By leveraging off-the-shelf mini-projectors and universal serial bus (USB) cameras, we can create accurate breast

surface acquisition systems that improve stand-alone optical imaging reconstructions, all without exposing a patient to more ionizing radiation. Chapter 7 discusses the use of additive manufacturing in the development of geometrically complex optical phantoms used to characterize new DOI systems, including all three systems in the first three aims. Finally, in Chapter 8, we highlight lessons learned and remaining challenges and conclude with the significance of this work.

CHAPTER 2

Background

In this chapter, we will first introduce the basics of optical imaging components, including how light interacts with tissue. The second part of this chapter discusses how light propagation is modeled. Finally, in the last section, we describe the imaging techniques leveraged in this dissertation.

2.1 Basics of Optical Imaging

Optical systems are composed of three elementary blocks: a source that radiates light, a sample through which light propagates, and a detector that measures the light intensity after photons have traveled through the sample [31]. Here, we first describe the fundamental interaction between light and tissue before highlighting the various types of sources and detectors used in the optical systems developed for this dissertation. We end this section with a short discussion on optical phantoms—fabricated materials with optical properties designed to mimic those of tissues.

2.1.1 Light-tissue interactions

Biological optical imaging has the capability to detect biological structure, function, and molecular characteristics based on photon interactions with tissue [32]. The interaction of light with tissue is governed primarily by three processes: reflection, absorption, and scattering [33].

The index of refraction, n, is a unitless number that describes how fast light travels through material [32]. It is used to determine how much the path of light is bent upon transitioning

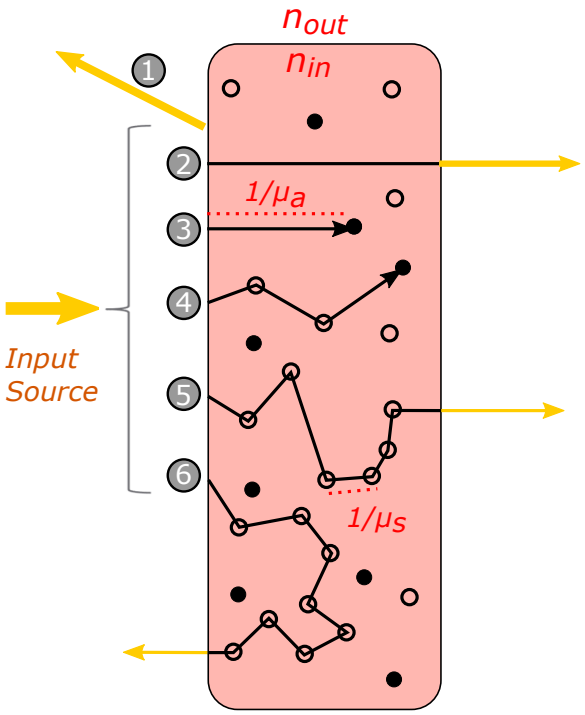

Figure 2.1: Possible interactions when light interfaces with tissue. The pink rectangle represents tissue. White circles are scatterers. Black dots are absorbers. (1) Specular reflection: light reflects without entering the tissue. (2) Ballistic transmission: light exits without interacting. (3) Absorption: light immediately gets absorbed. (4) Scattering: light scatters multiple times before being absorbed. (5) Diffuse transmission: light scatters multiple times before exiting the tissue on the opposite side it entered. (6) Diffuse reflection: light scatters multiple times but exits on the side it entered.

from one material to the next. This is governed by Snell's law of Refraction [32],

$$n_1 sin\theta_1 = n_2 sin\theta_2 \tag{2.1}$$

which define the angle of incidence, θ_1, and angle of refraction, θ_2, based on two media with indices of refraction n_1 and n_2. Thus, from Snell's law, we can also determine the amount of light that is reflected when reaching an interface (path 1 in Figure 2.1).

Once photons enter a media, they move in all directions and may be scattered or absorbed. If the media is absorbing only, some photons may be absorbed by the tissue while others may travel ballistically until they exit the other side (paths 2 and 3 in Figure 2.1). The absorption coefficient, μ_a $[cm^{-1}]$, is defined such that, when a photon propagates over an infinitesimal distance dx, the probability of absorption is $\mu_a \cdot dx$ [33]. By this definition, the amount of light intensity I attenuated can be described by $dI/I = -\mu_a dx$. Integrating this equation leads to the Beer-Lambert law [34], defined as

$$I(x) = I_0 e^{-\mu_a x} \tag{2.2}$$

where I_0 is the light intensity at $x = 0$.

Absorption depends on the chromophore concentrations of tissue [35]. In the visible to near-infrared wavelength range, the primary absorption components include hemoglobin, water, melanin, and lipids [36, 37]. The absorption coefficient depends on the molar extinction coefficient of a given chromophore, ϵ $[cm^{-1}M^{-1}]$, and its Molar concentration, c. Thus, the absorption coefficient per wavelength is

$$\mu_a(\lambda) = ln(10) \sum_{i=1}^{t} \epsilon_i(\lambda) c_i. \tag{2.3}$$

where t is the total number of absorbing components in the tissue. From this, we deduce that $1/\mu_a$ is the average path length traveled by a photon before being absorbed.

Turbid media such as tissue possess many scattering components. In addition to absorption events, light entering tissue can also undergo scattering events, events during which directionality changes occur due to biological structures within the media (paths 4, 5, and 6 in Figure 2.1). In the visible to infrared wavelength range, the primary scattering components in biological tissue are protein, fat, and mitochondria [36, 37]. Analogously, the scattering coefficient, μ_s, is defined such that, when a photon propagates over an infinitesimal distance dx, the probability of scattering is $\mu_s \cdot dx$ [33]. Additionally, we model the probability distribution of scattered photons using a phase function. For biological tissues, the most commonly used phase function is the Henyey-Greenstein phase function [38]. In this phase function, a scalar between -1 and 1, known as the anisotropy

factor g [32], denotes the directionality of the scattering angular distribution. A g value close to 1.0 g represents strong forward scattering; a g value close to 0 denotes isotropic scattering. To account for this anisotropy factor, we define the reduced scattering coefficient, $\mu_s^{'}$, as $\mu_s^{'} = \mu_s(1-g)$ [32]. The average distance traveled by a photon between scattering events is $1/\mu_s$. Additionally, since we treat absorption and scattering events as independent events, we can define the optical transport coefficient (μ_t), also referred to as the total interaction coefficient, as $\mu_t = \mu_s + \mu_a$. Analogously, the transport mean free path, the average distance between interaction events, is the reciprocal of μ_t.

2.1.2 Source and detector components of optical measurement systems

We can determine the biological structure and function of tissue based on how light interacts with tissue. In order to do that, we must illuminate the tissue with a light source as well as measure the diffuse light exiting the tissue.

Light emitting diodes (LED)s are compact, inexpensive, and energy-efficient semiconductor-based light sources (diodes) that can effectively convert electric energy to light [31]. They are ubiquitous in modern electronics and produce light spanning across a range of wavelengths. In our MOXI system, we leverage the white LEDs used for flash photography present in most smartphones. Our MOBI system uses dual-wavelength LEDs chosen to optimize propagation within the brain layers. Our OMCI system uses an LED projector (LEDs in conjunction with digital micromirrors) to shine patterns to scan the surface of the breast. For many spectroscopic measurements, it is important to have a light source that is monochromatic—meaning that the light irradiated has a single wavelength. In such cases, a Light Amplification by Stimulated Emission of Radiation (LASER) based light source is often used. Laser sources often have a low angle of divergence, making it easy to couple into precise optical components such as lenses and fiber optics. In OMCI, we use a laser diode to couple light into a projector to project wavelength-specific patterns onto the breast for wide-field trans-illumination.

Detectors are devices used to measure light. Photodiodes are the reverse of LEDs—they convert light into electrical current [31]. Their cost tends to be relative to their sensitivity. MOXI and MOBI use inexpensive photodiodes chosen to be sensitive to the wavelengths of their associated LEDs. OMCI uses cameras to detect the reflection and transmission of projected patterns. These cameras capture light through a small lens using a tiny array of microscopic detectors.

2.1.3 Optical phantom fabrication

Phantoms are objects made of stable materials with optical properties that mimic those of human tissues [37]. They are commonly used for characterizing and evaluating the performance of DOI systems [37]. To simulate NIR light propagation within biological tissues, phantoms typically contain scattering materials to provide the desired reduced scattering coefficient ($\mu_s^{'}$) and absorbing materials to simulate the wavelength-dependent absorption coefficient (μ_a) in biological tissue [39]. Traditionally, these phantoms are created using recipes that involve a mix of scattering agents and absorbing pigments with a base [40, 41]. The geometry of the phantom is typically created using either mold casting [42, 43] or spin coating [44].

2.2 Light Propagation Modeling

Light is a form of electromagnetic radiation, and thus can be modeled using Maxwell's equations. Although considered the most accurate, this model is typically only computationally feasible with tiny volumes spanning no more than a few dozen wavelengths. In turbid media such as tissue, the complex and frequent interactions between photons and media make it nearly impossible to directly apply this approach for effective modeling.

When simulating large, turbid, or random media, we often model light propagation as a collection of individual photon packets that interact with a background that has scattering and absorption properties. This model is called the linear transport theory [45], and it is modeled using the radiative transfer equation (RTE) [46]. The RTE is an integral-differential equation based on radiance conservation. It balances the total number of photons entering with the total number of photons exiting an infinitesimally small volume. Radiance, the power per unit area and unit solid angle [$J/(mm^2 sr)$], is defined by three spatial dimensions ($\mathbf{r} = \{x, y, z\}$), two dimensions defining the angular direction ($\hat{\Omega} = \{\theta, \phi\}$), and a temporal dimension (t). If we use the notation $L(\mathbf{r}, \hat{\Omega}, t)$ for radiance, then the RTE equation is:

$$\frac{1}{\nu}\frac{\partial L(\mathbf{r}, \hat{\Omega}, t)}{\partial t} + \nabla \cdot L(\mathbf{r}, \hat{\Omega}, t)\hat{\Omega} + \mu_t L(\mathbf{r}, \hat{\Omega}, t) = \mu_s \int_{4\pi} f(\hat{\Omega}, \hat{\Omega}')L(\mathbf{r}, \hat{\Omega}, t)d\hat{\Omega}' + Q(\mathbf{r}, \hat{\Omega}, t) \quad (2.4)$$

where ν is the speed of light in the medium, $f(\hat{\Omega}, \hat{\Omega}')$ is the scattering phase function, $Q(\mathbf{r}, \hat{\Omega}, t)$ is the radiance source function, and μ_t is the optical transport coefficient defined in subsection 2.1.1.

The left side of Equation 2.4 represents the photons leaving an infinitesimally small volume element due to absorption, scattering, and divergence. The right-hand side balances the equa-

tion by representing the photons being scattered from all directions into direction $\hat{\Omega}$ and the photons entering the volume that come directly from the photon source. The difficulty with using the RTE is two-fold. First, because the equation involves both integrals and derivatives of radiance, obtaining a closed-form analytical solution is difficult save for simple scenarios. Second, numerical approaches are computationally intensive due to the need to discretize and store the high-dimensional quantities of space, angle, and time [47].

One numerical method that has taken on this computationally demanding challenge is the Monte Carlo (MC) method [48, 49]. Rather than a model-based approach, MC simulates millions of photon trajectories to converge to a steady stochastic solution. By defining each trajectory with a simple set of rules based on physical laws, MC is an embarrassingly parallel workload method that can leverage computational hardware improvements such as graphical processing units (GPUs) [50].

However, in certain scenarios, such as when the media is highly scattering, we can simplify the RTE to gain even more computational efficiency compared to an MC approach. In highly scattering media such as the breast, we can assume that the reduced scattering coefficient is much greater than the absorption coefficient ($\mu_s' \gg \mu_a$), and thus ignore the angular dependency of photon radiance. By considering the photons to scatter isotropically, we can approximate the radiance as the fluence, or $\Phi(\mathbf{r}) = \int_r \int_{\hat{\Omega}} L(\mathbf{r}, \hat{\Omega}, t) d\hat{\Omega} dt$, allowing us to reduce the RTE to a quadratic partial differential equation that is relatively simple to solve. We call this equation the diffusion equation (DE) [51, 52], defined as:

$$-\nabla D(\mathbf{r}) \nabla \Phi(\mathbf{r}, t) + \mu_a(\mathbf{r}) \Phi(\mathbf{r}, t) + \frac{1}{\nu} \frac{\partial \Phi(\mathbf{r}, t)}{\partial t} = S(\mathbf{r}, t) \tag{2.5}$$

where $S(\mathbf{r}, t)$ is the isotropic source term and D is the diffusion coefficent defined as $D = \frac{1}{3(\mu_a + \mu_s')}$.

An in-house MC-based light simulator, Monte Carlo eXtreme (MCX) [53], can incorporate geometrically-accurate boundaries into simulations to study diffuse optics in complex shapes. Another in-house tool, Redbird-m [54], is a diffusion-based tool for analyzing large scattering media. In the following chapters, we will run MCX-based forward models for designing our MOXI and MOBI systems and will use the diffusion solver Redbird-m for the forward modeling related to OMCI due to the larger target tissue volume.

2.3 Imaging Techniques

Light propagating in biological tissue is in the diffusive regime, meaning that photon propagation loses directionality after extensive scattering events. DOI is the general imaging modality

that uses measurements of diffuse light to investigate tissue characteristics. Diffuse optical spectroscopy (DOS) is the method of using diffuse light to infer scattering and absorption. In biological tissue, we typically use the NIR range due to its low absorption by tissue, and thus, DOS is often referred to as near-infrared spectroscopy (NIRS). When we apply DOS to generate 2-D or 3-D volumetric distributions of tissue optical properties, we are creating tomographic images. We refer to this implementation of DOI as DOT. One exception among the imaging techniques investigated in this work is SLI. It utilizes reflected light from the tissue's surface, instead of diffusive photons, to acquire 3-D geometrical shapes.

Figure 2.2 sets the context for this dissertation by overlaying the imaging techniques and relevant anatomies used in our three systems over the light-tissue interactions seen in Figure 2.1. Although traditional pulse oximeters use diffuse transmission interactions [dashed line in Figure 2.2(a)], MOXI performs DOS from diffuse reflected light [solid line in Figure 2.2(a)]. MOBI leverages diffuse reflected light to perform NIRS [Figure 2.2(b)]. fNIRS systems may also perform DOT when an array of sources and detectors are used. In OMCI, we perform DOT from illumination using a wide-field pattern and detector from a camera [Figure 2.2(c)]. Additionally, OMCI also uses SLI from reflected light to determine the breast shape [Figure 2.2(d)]. An introduction to these four imaging techniques follows.

2.3.1 Pulse Oximetry

Pulse oximetry is used to measure oxygen saturation of hemoglobin in arterial blood and is so widely prevalent it is regarded as the fifth vital sign in medical care [55]. It is based on two principles. The first is that oxygenated hemoglobin (HbO) and de-oxygenated hemoglobin (HbR) absorb red and infrared (IR) light differently [56]. Because of this, pulse oximeters tend to emit only two wavelengths of light. Traditional (finger-clip) pulse oximeters place light sources and detectors on opposite sides of the finger [Figure 2.2(a)]. Expanding Equation 2.3, we can use two wavelengths λ_1 and λ_2 to obtain the molar concentrations of oxygenated and de-oxygenated hemoglobin, c_{HbO} and c_{HbR}, by simultaneously solving the following [32]:

$$\mu_a(\lambda_1) = ln(10)\epsilon_{HbO}(\lambda_1)c_{HbO} + ln(10)\epsilon_{HbR}(\lambda_1)c_{HbR} \tag{2.6}$$

$$\mu_a(\lambda_2) = ln(10)\epsilon_{HbO}(\lambda_2)c_{HbO} + ln(10)\epsilon_{HbR}(\lambda_2)c_{HbR} \tag{2.7}$$

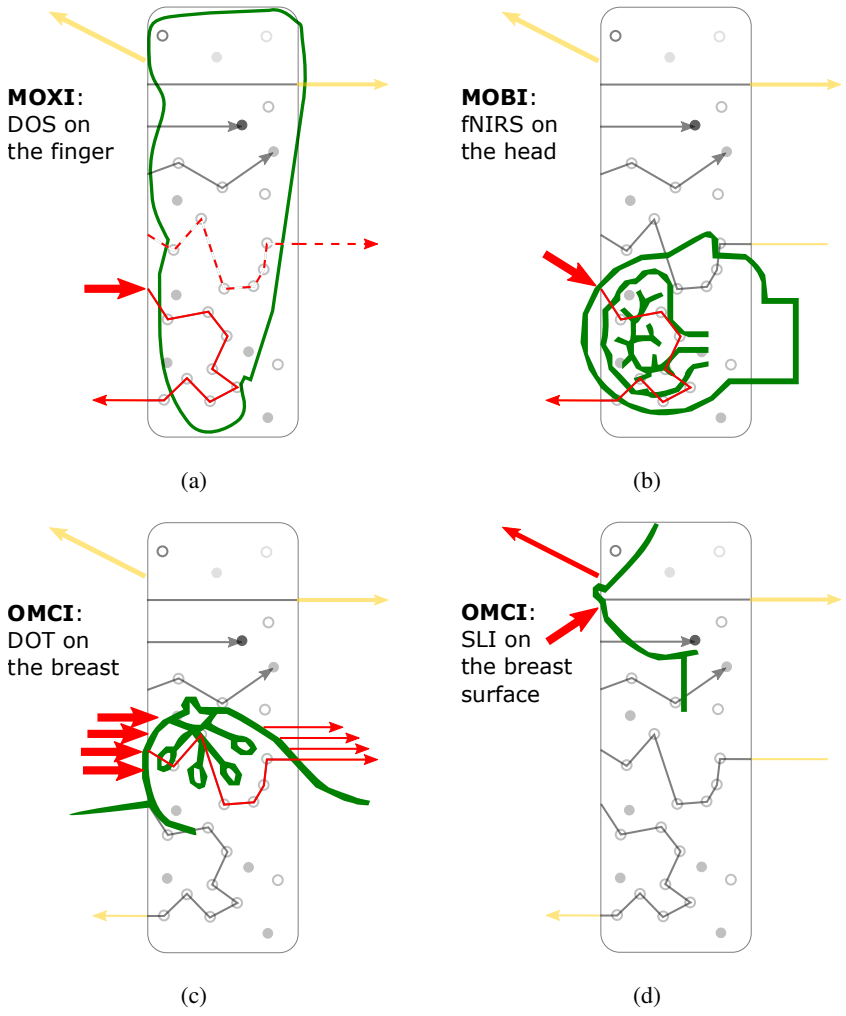

Figure 2.2: Relevant anatomies (finger, head, breast) for the three imaging systems (MOXI, MOBI, OMCI) overlaid on light-tissue interactions in Figure 2.1. Red light paths highlight the type of interaction used in each imaging system and technique. (a) MOXI uses diffuse reflected light measured at the finger. (b) MOBI uses diffuse reflected light measured at the scalp. (c) Our OMCI system performs DOT on the breast using trans-illumination. (d) Reflected light is used for SLI measurements on OMCI. Anatomies in green are representative and are not to scale.

The total hemoglobin concentration, c_{HbT}, can then be calculated simply by $c_{HbT} = c_{HbO} + c_{HbR}$ [35]. We can then obtain blood oxygen saturation (SO_2) using

$$SO_2 = \frac{c_{HbO}}{c_{HbT}} \tag{2.8}$$

The second principle of pulse oximetry is that arterial blood volume fluctuates with the cardiac cycle while blood volume in veins, capillaries, skin, fat, and bone remains relatively constant [57]. Thus, light that propagates through the finger and is detected by the detector has two components during temporal measurements of the cardiac cycle—a relatively stable and non-pulsatile direct current (DC) component from the constant volume in veins and capillaries, and a pulsatile alternating current (AC) component from the volume fluctuation of the arteries [58]. This detected time trace is called a photoplethysmogram (PPG) [57]. Traditional pulse oximeters use the amplitudes of PPG signals from red and IR light to calculate oxygen saturation. Technically, pulse oximetry measures peripheral blood oxygen saturation (SpO_2), which is a measure of oxygen saturation measured at the finger. SpO_2 is calculated from the ratio of the AC to DC components of the red and IR light. The ratio-of-ratio (RR) is defined as

$$RR = \frac{A_{red,AC}/A_{red,DC}}{A_{IR,AC}/A_{IR,DC}} \tag{2.9}$$

where A is the amplitude of the PPG trace. At low oxygen saturation, the increased presence of HbR leads to a larger relative change in amplitude of red light due to the pulse compared to IR absorbance ($A_{red,AC} > A_{IR,AC}$), resulting in a higher RR value. SpO_2 is calculated from a calibration curve mapping RR to SpO_2 generated from empirical measurements of RR in healthy volunteers with altered saturations [59].

2.3.2 Functional Near-Infrared Spectroscopy

An emerging neuroimaging technique that uses low-power near-infrared light to measure hemodynamic changes due to brain activities is fNIRS [60]. It is based on three fundamental principles. The first is the same as pulse oximetry, which is that human tissue is relatively transparent to light in the near-infrared range allowing photons to propagate. Secondly, hemoglobin has unique absorbing characteristics that allow for oxygenation-dependent quantification of NIR light absorption [61]. The third is the theory of neurovascular coupling, which states that the brain's demand for oxygen is altered by neuronal activation. FNIRS assumes that changes in hemoglobin concentrations are indicators of brain activity [60].

In fNIRS, multiple sources and detectors are placed on the scalp over a region-of-interest (ROI) [62]. The photons travel through the head being scattered and absorbed by the different tissue types [63] (scalp, skull, cerebrospinal fluid, and neuronal tissue) until the non-absorbed components of the scattered light are detected by a detector [64, 65] [Figure 2.2(b)]. The complication with light traveling in the head is the highly scattering nature due to multiple tissue types makes it difficult to estimate the actual photon distance traveled. Thus, we need to modify the Beer-Lambert law to better account for the pathlengths of photons [66]. Using Equation 2.2, we can define optical density (OD) in the Beer-Lambert law as $OD = -log_{10}(I/I_0) = -\mu_a \cdot X$. The modified Beer-Lambert law (MBLL) extends the Beer-Lambert law to include G, a parameter that accounts for light intensity loss due to scattering. The intensity of the light detected will change due to the concentration changes of HbO and HbR induced from local brain activity [65, 67], which change the absorption rate of neuronal tissue. The MBLL is expressed as

$$OD(t,\lambda) = -log_{10}\left(\frac{I(t,\lambda)}{I_0(t,\lambda)}\right) = \sum_i \epsilon_i(\lambda)c_i(t)DPF(\lambda)d + G(\lambda) \tag{2.10}$$

where d is the distance between the source and detector on the scalp, and DPF is the differential pathlength factor, a unitless variable that accounts for the increased distance that light travels in the brain. Finally, if we make the assumption that G is time-invariant and only absorption properties change with brain activity, we can relate changes in light measurements to changes in tissue absorption by simply comparing a baseline to a perturbed state, resulting in

$$\Delta OD(\lambda) = \left[\sum_i \epsilon_i(\lambda)\Delta c_i(\lambda)\right] \cdot DPF(\lambda) \cdot d \tag{2.11}$$

Equation 2.11 allows for the calculation of c_{HbO} and c_{HbR} from two wavelengths. However, we can extend this approach to use multiple wavelengths to calculate the concentration changes of multiple chromophores.

2.3.3 Diffuse Optical Tomography

DOT is a non-invasive imaging technique for 3-D functional tissue characterization [16]. This is done through the illumination of tissue with an array of light sources and the measurement of the exiting light with an array of detectors [68] [Figure 2.2(c)]. Typically, a source in the array is turned on and the light is measured by all detectors for that source. This is repeated sequentially for each source. We can leverage photon propagation techniques to simulate the expected measurements of exiting light. Herein lies the problem: we must know the optical properties of the tissue

in order to simulate the forward problem, but the determination of those unknown scattering and absorption coefficients is precisely what we are trying to derive [52]. Therefore we must "invert" our model. The image reconstruction problem, also known as the inverse problem, seeks to determine volumetric distributions of optical properties that can best fit the measurement data taken at the surface of the domain.

Although conceptually simple, the solution to the inverse problem is notoriously difficult due to DOT being non-linear, ill-posed, and generally underdetermined, making it difficult to find a unique and reliable solution. Typically, we formulate the inversion as a parameter optimization problem and use a regularization approach where we add a second term to be minimized to obtain a meaningful solution [69], such as

$$\hat{\mathbf{x}} = \underset{\mathbf{x}}{\operatorname{argmin}} \left\| \mathbf{y} - \Gamma \cdot \Phi(\mathbf{r}) \right\|^2 + \lambda \left\| \mathbf{x} - \bar{\mathbf{x}} \right\|^2 \tag{2.12}$$

where λ is the regularization parameter. The first term is quantifying our measurement data, where $\mathbf{y}$ is the measured fluence by our detectors and Γ is a spatial-sampling matrix used with our forward simulation, $\Phi(\mathbf{r})$. The second term, $\left\| \mathbf{x} - \bar{\mathbf{x}} \right\|^2$, attempts to penalize solutions and stabilize the inversion of our forward model. It is composed of our unknown vector of optical properties, $\mathbf{x}$, and a vector of known (or assumed) initial guesses, $\bar{\mathbf{x}}$. The regularization parameter is essentially balancing our need to fit the solution to the measured fluence by enforcing how reasonable our solution should behave (in our case, reasonable behavior is a solution that stays as close as possible to our prior knowledge). Both the approach to the inverse problem as well as methods for picking the regularization term are active areas of investigation [15, 70, 71].

2.3.4 Structured-Light Imaging

One method of improving DOT image reconstructions is to further constrain the inverse problem through highly accurate breast surface estimations to provide geometric boundaries used in light propagation models. An emerging, non-invasive 3-D surface imaging technique is SLI. SLI works by illuminating an object with 2-D spatially varying patterns and using an imaging sensor (e.g. a camera) to capture the illuminated object [72] [Figure 2.2(d)]. The distortion of the specially designed patterns informs of the geometric properties of the object. Calibration of the projector-camera system is easily done by capturing images of a known planar pattern [73]. With the ability to use off-the-shelf components, its use with a single projector and camera, and a robust and simple calibration method, SLI is positioned to be an accurate, fast, and cost-effective breast surface imaging system.

CHAPTER 3

Mobile-phone based oximeter (MOXI)

In this chapter, we establish the feasibility and accuracy of three smartphone-based approaches to monitoring oxygenation. Compared to a traditional finger-clip-based pulse oximeter, all three devices in this chapter improve on the portability attribute of this spectroscopic-based instrument by using either phone-powered boards, wrist-worn designs, or the use of ultra-low-cost components. Additionally, features like non-contact measurements and a mobile application to control multiple devices all facilitate the potential scaling of the use of NIRS. Here, we detail the design, fabrication, and evaluation of three distinct NIRS devices, each with distinct advantages for use in LMICs.

In order of decreasing the complexity of hardware, the first device (D1) is a Bluetooth wireless oximeter board with a dedicated pulse oximetry chip [green square in Figure 3.1(b)]. The second device (D2) measures tissue oxygen saturation (StO_2). It functions by imaging light attenuation in tissue through a slit on a circuit board carrying LEDs [yellow square in Figure 3.1(c)]. The third device (D3) is a paper filter covering half of the field of view of a smartphone camera [Figure 3.1(b)]. All three devices utilize our in-house developed mobile phone application [Figure 3.1(a)] to monitor heart rate (HR) and SpO_2. The three devices, along with a screenshot of the mobile phone application, are seen in Figure 3.1. Although we include details on D1 and D2 for completeness, when we refer to the MOXI system, we are referring to the colored-paper-based D3 design.

Table 3.1: Barriers to adoption of new medical devices in LMICs

Rank	Barrier to Adoption
1	Acquisition Costs
2	Spare Parts
3	Consumables
4	Reliable Power
5	Infrastructure
6	Training

3.1 Introduction

Every year, nearly 3 million newborns die within the first 4 weeks of life in LMICs [74]. Respiratory complications, such as birth asphyxia, and congenital heart defects, such as Tetralogy of Fallot (which results in Blue Baby Syndrome – a condition caused by low tissue oxygenation), are among the major causes of death at birth for neonates. In addition, over 17% of the post-neonatal child deaths are caused by childhood pneumonia and other acute respiratory infections, accounting for 4 million deaths per year for children under age 5 [75]. These conditions often lead to low arterial and tissue oxygenation [76]. Many of these complications are easily screened, diagnosed, and continuously monitored in most facilities in developed countries using a pulse oximeter, a device to measure SpO_2 levels using low-power light based on NIRS.

Finger-clip-based pulse oximeters, however, are difficult to use on small fingers. Newborn-specific pulse oximeter probes, often sold as disposable parts, can cost up to $100 USD, and require a more expensive oximeter system to read and display results [77, 78]. These designs thus have an extremely limited presence in first-level clinics in LMICs. In recent years, portable NIR devices have been reported, but they generally have high costs dues to sensitive charge-coupled device (CCD) cameras and stand-alone image acquisition software [79], or still require the use of a finger-clip [80, 81]. Many factors, primarily high acquisition and maintenance costs (Table 3.1), have hindered the adoption of portable diagnostics tools [82].

In 2018, the Pew Global Research Center reported that smartphone ownership in LMICs rose from 21% to 45% between 2013 and 2018, making smartphone networks the fastest growing infrastructure in LMICs [83]. By capitalizing on the ubiquitous presence of smartphones worldwide, we aim to develop phone-camera-based and phone-communication facilitated NIRS devices to measure arterial and tissue oxygenation, directly addressing the barriers to adoption in Table 3.1. These smartphone-based devices can address the current limitations of conventional pulse oximeters, in-

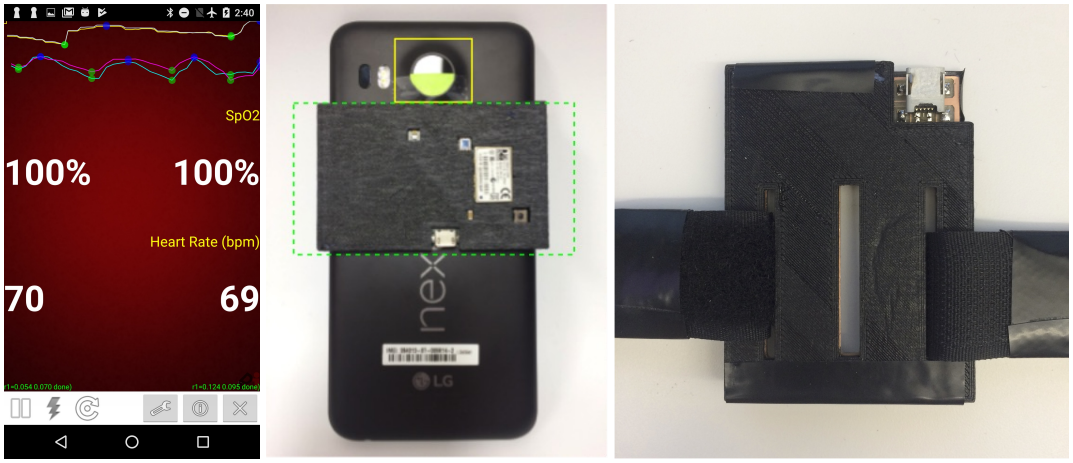

(a) (b) (c)

Figure 3.1: (a) Screenshot of Moximeter mobile application simultaneously capturing D1 and D3 data. (b) D1 (green, dashed) and D3 (yellow, solid) mounted on a smartphone phone. (c) D2 board with cover.

cluding newborn-unfriendly clip designs, acquisition and maintenance costs of disposable probes, and the need for frequent disinfection due to direct skin contact. Leveraging smartphone features such as cameras, LEDs, and wireless communication along with their power and computation will pave the way for point-of-care (POC) smartphone-based diagnostic tools.

3.2 D1: Bluetooth Reflectance Pulse Oximeter

3.2.1 D1 hardware

The D1 design works similarly to a clinical-quality pulse oximeter, except the optodes are placed on the same side of the finger. A photodiode captures the diffuse reflected light emitted from two onboard LEDs (640 and 940 nm) in order to estimate SpO_2. This reduced form factor, non-finger-clip design makes pulse oximetry measurements more newborn-friendly. The D1 board makes use of a low-cost ($3.5 USD) dedicated analog front-end (AFE4490) pulse oximeter signal-processing chip (AFE4490 Integrated Analog Front-End, Texas Instruments, USA) and a microcontroller (ATMega32u4, Atmel, USA) communicating via the serial-peripheral interface (SPI) communication protocol. The 40x40 mm^2 rigid printed circuit board (PCB) can be battery-powered or powered by a mobile phone using a male-to-male USB cable.

(a) (b)

Figure 3.2: (a) D1 phone mount. (b) Simultaneous capture of D1 and D3.

3.2.1.1 Optode settings for neonates

In diffuse reflectance measurements, the distance between the sources and detector determines the depth of photon propagation. Given the larger fingers of adults compared to neonates in our initial studies (Massachusetts General Hospital approval is for use on adults with subsequent tests on neonates), the current reflectance board has optodes optimized for an adult finger by using a large source-detector distance of 17 mm. This was empirically chosen based on sweeping the source-detector (SD) distance from 2.54 to 15.24 mm in 2.54 mm increments (0.1 inches to 0.6 inches in 0.1-inch increments based on the breakout board). The highest signal-to-noise ratio (SNR) at this distance was obtained when driving the LEDs at 25 mA. Both 10 and 50 mA resulted in smaller amplitudes of the AC component of the signals due to low photon detection and photodiode saturation, respectively. The same trend is seen with the SD distance where being too close or too far leads to weak signals or photodiode saturation. Although set to 17 mm for the pilot rests with adults, when used on neonates, the SD distance should be decreased to account for their smaller finger sizes.

3.2.1.2 Phone mount

The D1 board is placed over a Nexus 5X smartphone using a custom mount [Figure 3.2(a)]. The mount not only holds the D1 board onto the phone but also prevents users from touching the active electronics of the PCB. The mount is 3-D printed out of polylactic acid (PLA). The side

panels that grip onto the phone have gaps designed to avoid accidentally pressing the volume and power buttons on the sides of the smartphone. The D1 board is press fit onto two small round tabs on the inside of the mount, eliminating the need for extra tools. The flat side of the mount is 0.2 mm thick to allow maximum surface contact of the optodes with the finger. Holes on the mount allow access to the reset button of the board, as well as allow the Bluetooth chip to protrude outside for better signal quality. The D1 board is mounted off-center to the smartphone to accommodate the longer length of the middle finger compared to the index finger. This allows both fingers to lay comfortably flat during simultaneous capture of D1 and D3 signals [Figure 3.2(b)]. The D1 board is powered by a USB male-to-male cable connecting the board to the smartphone's battery.

3.2.2 D1 software

An Android phone application called Moximeter, written in Java, was developed to process the received signals from the D1 and display the results on the phone. Register values of the AFE4490 were set to 25 mA for each optode and a 500 Hz corner filter was applied post-amplification. A long pulse repetition frequency of 250 Hz allows for dynamic averaging of 16 samples per data point by the analog-to-digital converter (ADC) to increase SNR. Bluetooth communication transmits data between the D1 board and the phone. The phone application displays the signals for the red and IR channels at the top of the screen. The signal sample-per-second (in Hz) is dynamically estimated and the PPG waveforms are processed in real-time using embedded C-code for maximum efficiency to obtain the oxygen saturation values. The real-time signal processing includes a built-in signal filtering algorithm, a peak detection algorithm, an algorithm to estimate HR, and an algorithm to compute SpO_2 using a transmission pulse oximeter calibration model [84]. The real-time HR and SpO_2 values are displayed in the Moximeter graphical user interface (GUI) [Figure 3.1(a)].

3.2.2.1 Noise removal

Unlike a transmission finger clip where the optodes and finger are coupled, a reflectance-based measurement is more prone to noise and artifacts since the finger being sampled can move independently of the optodes. To reduce this noise, 16 readings of red and IR readings are sampled by the AFE4490 prior to sending an average value to the Moximeter phone application. The sampling is done onboard to maintain our 60 Hz sampling rate. Additionally, a 5 ms delay has been added between the SPI transfer calls by the microcontroller to allow the AFE4490 to stabilize. This

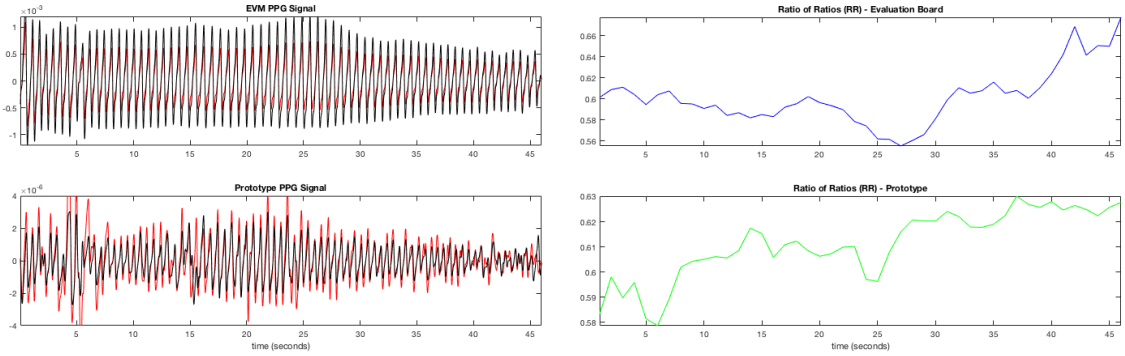

(a) (b)

Figure 3.3: (a) Photoplethysmogram signals from evaluation module board and D1 design. (b) Ratio-of-ratios in blue (evaluation module) and green (D1 Device).

stabilization prevents the loss of data and decreases the likelihood of garbled measurements. As an added precaution, our processing of data workflow now incorporates a mean filter in addition to our bandpass filter to remove any unwanted "chirps" or spikes in data.

3.2.2.2 Independent source control

The receiver channel of the board is made up of a differential current-to-voltage transimpedance amplifier followed by a current digital-to-analog converter (DAC). The amplifier has programmable a feedback resistor (R_F) and a capacitor (C_F) to form a low-pass filter for the input signal current. The output voltage of the amplifier includes the AC component and a component resulting from ambient light leakage. The DAC attempts to amplify only the AC component of the PPG signal. By systematically varying R_F, C_F, and the transmitter reference voltage for each optode, we are able to determine the AFE4490 configuration that maximizes the AC components of both red and IR PPG signals, independently. Since the RR is based on the amplitude of the AC component of the PPG signals, increasing the AC range with optimized AFE4490 configurations allows for more sensitivity in RR calculations and thus more accuracy in SpO_2 readings.

3.2.3 D1 results

To evaluate the D1 prototype, we compared the obtained signals from our device against simultaneously acquired signals from an evaluation module (EVM). The EVM captures PPG sig-

(a) (b) (c)

Figure 3.4: (a) Top side of D2 circuit showing USB connector and microcontroller. (B) Bottom side of the D2 circuit showing deep red (top) and red (bottom LEDs). (C) D2 board powered by a smartphone and an on-the-go USB cable.

nals through transmission via a finger flip on the middle finger. The index finger of the same hand was placed over the optodes on the D1 device. The PPG signals in Figure 3.3(a) were simultaneously captured from the D1 device and from the AFE4490 EVM during a 46-second breath-holding procedure. Signals were band-pass filtered using a sixth-order zero-phase Butterworth filter to remove out-of-bound noise (0.2 to 5 Hz). As shown in Figure 3.3(b), RR (Equation 2.9) increases as SpO_2 decreases due to the larger difference between extinction coefficients of HbO and HbR at red versus IR light. The pairwise linear correlation coefficient, R, between the two ratio-of-ratio signals in Figure 3.3 is 0.4856.

3.3 D2: Single Slit Oximeter

3.3.1 D2 hardware

The D2 design is a compact, low-cost, non-contact, and wearable LED-based illumination module to quantitatively measure StO_2. The D2 design is made from a 53x28 mm^2 circuit board with a 2x20 mm^2 imaging window (the "slit") [Figure 3.4(a)]. Two LEDs (640 and 730 nm) are mounted facing the skin at opposite sides of the long dimension of the slit [Figure 3.4(b)]. A 730 nm wavelength was chosen because IR light is not visible in the smartphone complementary metal-oxide semiconductor (CMOS) sensor. Moreover, HbO shows a similar absorption at the two wavelengths and HbR has a higher absorption at 640 nm than at 730 nm.

A micro-USB connector is added to provide power while a microcontroller (ATtiny85, Atmel, USA) controls the LED timing [Figure 3.4(c)]. Four of the eight pins on the microcontroller are used by the in-service programmer (ISP) to program the board using the Master-In-Slave-Out (MISO), Master-Out-Slave-In (MOSI), Serial Clock (SCK), and reset (RST) pins. Power and ground each have a dedicated pin, leaving two analog pins available for the red and deep red LEDs. The use of analog pins allows us to use pulse-width modulation (PWM) to drive the LEDs. By varying the pulse width, we can control the time an LED is on and control its intensity. The microcontroller has a max output of 40 mA per pin, allowing the LEDs to be connected without the need for resistors. The board is programmed by holding the ISP pins onto the pads without soldering, allowing us to remove the programming pins after programming and reducing the board thickness. In total, the only four components on the D2 milled circuit board are the two LEDs, the microcontroller, and a USB female header for power.

The D2 design is made of two milled copper boards placed back-to-back. This has two main advantages. First, it allows the ability to easily swap out any broken LEDs if they break during use without having to mill out all the traces. Secondly, the LEDs are soldered directly to the underside of the board, allowing them to be in direct contact with the skin to minimize specular reflection. The entire board is encased inside a 3-D printed PLA cover. Velcro straps on the edges of the milled board allow the D2 design to be comfortably worn [Figure 3.1(c)].

3.3.2 D2 software

The microcontroller is programmed to cycle between three stages at one-second intervals. After securing the module with an elastic Velcro strap and powering the board with a USB cable, the microcontroller automatically begins cycling between the red LED on, deep red LED on, and no LEDs on, each for one second, indefinitely. The one-second interval with no LEDs on is used to capture background data. The diffuse reflection profile across the slit of both wavelengths can be measured directly by taking a video of the slit opening using the smartphone camera controlled by our Moximeter application. The three intervals from the video stream are automatically detected by comparing intensity values at the ends of the slit. A moving bin average is used to estimate StO_2 changes.

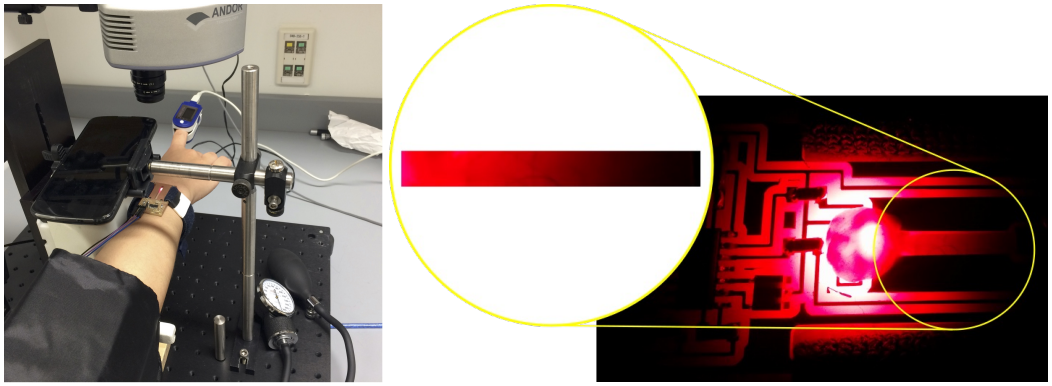

(a) (b)

Figure 3.5: (a) Nexus and Andor camera experimental setup. (b) Example cropped slit image for analysis.

3.3.3 D2 results

Here, we propose to use the linear slope of the log-scaled image intensity along the slit as a surrogate marker to correlate with tissue oxygenation changes. This slope can be easily computed in real-time on low-power devices such as mobile phones.

3.3.3.1 Protocol and setup

A Nexus 5 Android phone and an Andor electron-multiplying charge-coupled device (EMCCD) camera (Luca-R, Andor, UK) were both mounted above the slit region and used to acquire video recordings simultaneously [Figure 3.5(a)]. The cameras recorded at 10.8 (Andor) and 30 (Nexus) frames per second while the red and deep red LEDs alternated every second. Data were captured in a dark room with the phone screen brightness set to the lowest setting. The subject held onto a handle during data gathering to minimize motion artifacts. An example of the acquired image (cropped using MATLAB) can be seen in Figure 3.5(b). Slit images were analyzed frame by frame for each camera. A blood occlusion experiment was performed using a standard pressure cuff. Prior to data capture, the pressure was increased to 200 mmHg and held for 20 seconds. After 20 seconds of data capture, the pressure was released.

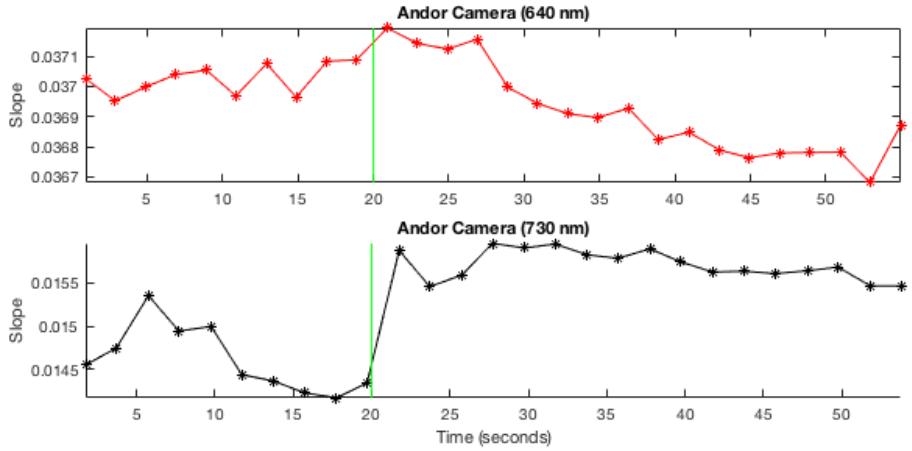

(a)

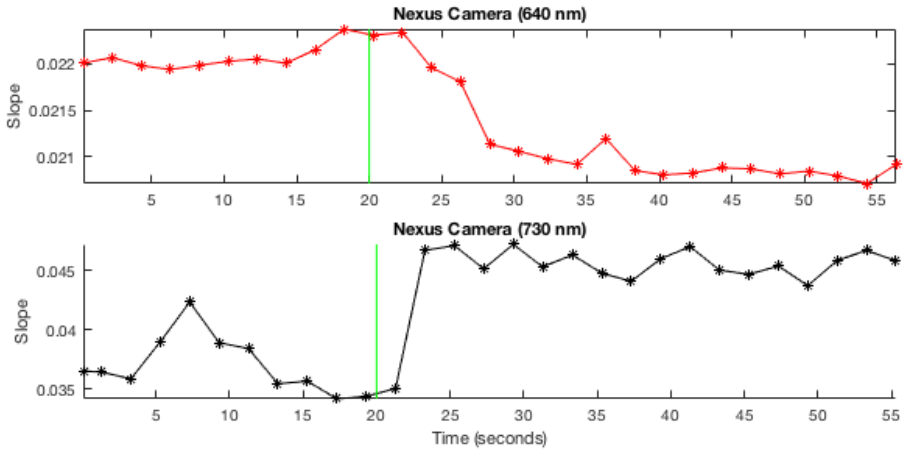

(b)

Figure 3.6: Intensity attenuation slopes for the Andor (a) and Nexus (b) camera data. Top (640 nm) and bottom (730 nm) rows show the averaged attenuation slope of the log-scaled light intensity over time within a selected window. The vertical green lines mark the point at which pressure from the cuff was released.

3.3.3.2 Benchtop results

The linear slope time courses obtained from the Andor and Nexus cameras for 640 and 730 nm are shown in Figure 3.6. Each marker in the plot is obtained by averaging the frames during the 1 second a particular LED is on. The vertical green line indicates the point of pressure release. The overall shape of the slope profile from the Nexus camera is similar to the Andor camera in both 640 and 730 nm. The pairwise linear correlation coefficients, R, between the two cameras are 0.8627 (640 nm) and 0.7986 (730 nm). The increase in slope immediately following the pressure release is expected due to the higher absorption coefficient of the total hemoglobin that rushes in. These results suggest that a low-cost phone camera is capable of capturing blood volume and oxygenation changes in tissue.

3.4 D3: Paper Filter Pulse Oximeter (MOXI)

The D3 design is a broadband diffuse reflection pulse oximeter that utilizes a smartphone's embedded flash LED as the source and the smartphone's camera as a detector. An ultra-low-cost paper filter covering half of the camera's field of view manipulates the original spectra by attenuating certain wavelengths (Figure 3.7(a)). The hypothesis is that when a finger is placed over the phone's camera and LED, the observed spectra differences combined with the tissue absorption spectra will make it possible to make spectroscopic measurements. Point-of-care devices like these that require no or minimal attachments provide a much greater impact on the accessibility of such devices in resource-poor regions by directly addressing the acquisition and maintenance costs that hinder technological adoption (Table 3.1).

3.4.1 Photon propagation simulations

3.4.1.1 MCXlab simulations

A previously segmented, high-resolution, 7 Telsa realistic 3-D finger model was used for the photon propagation simulations [85] [Figure 3.7(c)]. The original 15 components were combined to represent six tissue types: dermis, epidermis, arteries, veins, fatty tissue, and bone. We ran a series of GPU-based Monte Carlo simulations using MCX [53] using 5×10^9 photons in both transmission and reflectance mode. The detector diameter was set to 3 mm, and the source-detector distance in reflectance mode was set to 10 mm, as measured from the mobile phone's dimensions. To simulate broadband light, the optical properties of the finger tissues were swept between the

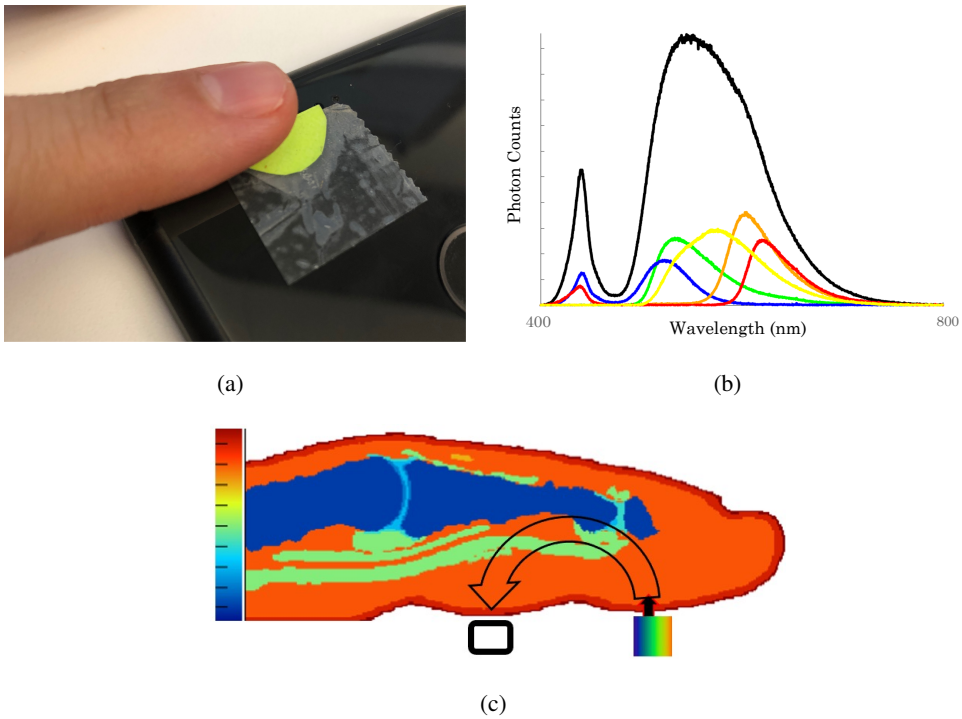

Figure 3.7: (a) D3 design in use with a finger placed over the camera after a paper filter is taped over the bottom half of the mobile phone camera. (b) Broadband spectra (black) and resulting spectra after manipulation using colored paper filters. The color line refers to the color of the paper filter. (c) Simulation setup showing finger model with six tissue types.

wavelength band of 350 to 1000 nm in 1 nm increments, with intensity based on the measured spectrum of an Android Pixel 2's LED. The filtered broadband light was then further attenuated by the ratio between unfiltered and filtered spectra. The intensity was estimated by fluence.

3.4.1.2 Optical properties

The optical properties of the six tissue types were compiled from literature. The absorption and scattering coefficients of oxygenated whole blood, de-oxygenated whole blood, water, and melanosome were obtained from the MCXYZ.c light transport program [86]. Bone optical properties were digitized from published results [87]. Dermis and epidermis tissue optical properties were created from blood [88], water [89], fat [90], and melanosome [91] volume fractions from literature [92]. Blood was assumed to have a hematocrit value of 45%. The remaining 55% is plasma, which is typically composed of 92% water and 8% food, protein, and other solids [92], but was simplified to 100% water for these simulations. Venous blood was assumed to have 70% SpO_2. SpO_2 levels ranging from 85% to 100% are simulated by adjusting the corresponding optical properties of blood resulting from the volume fractions changes of the arteries.

3.4.1.3 Attenuation spectra of paper filters

A spectrometer (Flame VIS-NIR, Ocean Insight, USA) was used to measure the spectrum of an Android Pixel 2 flash LED. Transmission spectra from paper filters of various colors, which further alter the light source spectrum, were also measured [Figure 3.7(b)]. Broadband spectra were scaled to a max arbitrary unit of 1. The green paper filter was chosen due to its capability of blocking near-infrared light while still not attenuating the original broadband light significantly. This provides a means to differentiate between the broadband light source and a filtered broadband source, which, when combined with the tissue absorption spectra, makes spectroscopic measurements using two broadband sources possible.

3.4.1.4 PPG signal generation

The PPG signal, the measured intensity by the detector, was simulated by increasing the volume of the arteries in the model using a gaussian filter until a 20% change in the detected fluence was obtained at 690 nm in transmission [93]. This artery volume increase was used for both transmission and reflection modes as well as for both traditional (two-wavelength) and broadband simulations. All other tissue volumes remained constant. The resulting fluence values for both

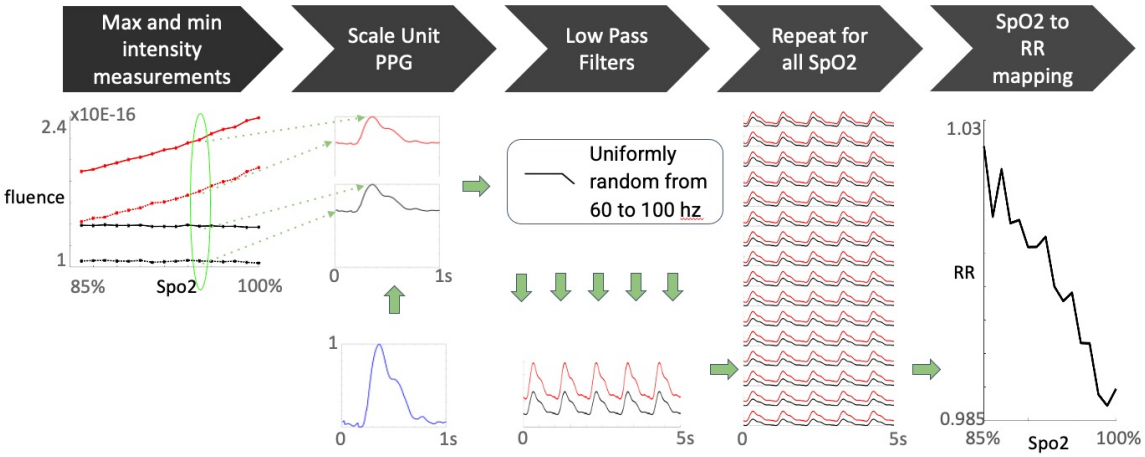

Figure 3.8: Process of creating the ratio-of-ratio to arterial blood oxygen saturation mapping in simulation. Monte Carlo simulations result in fluence measurements at various arterial blood oxygen saturation values for both wavelengths at 0 and 20% artery volume increase. An example 1 second photoplethysmogram pulse is scaled by the fluence measurements and repeated to create a time trace. Each repetition is low-pass filtered with a randomized cutoff frequency between 60 and 100 hz. The ratio-of-ratio value is then calculated from the simulated photoplethysmogram signals.

finger artery volume changes were then used to scale a discretized PPG signal [94] to create a 60 bpm oscillation optical measurement. A PPG signal was created for each SpO_2 value for each pulse oximeter mode (transmission and reflection), as well as for traditional (two-wavelength) and broadband simulations (Figure 3.8).

3.4.1.5 Ratio-of-ratio for broadband spectroscopy

The traditional calculation of RR in Equation 2.9 was altered slightly to account for broadband light. For this device, RR is defined as

$$RR = \frac{A_{BB,AC}/A_{BB,DC}}{A_{FB,AC}/A_{FB,DC}} \tag{3.1}$$

where A is the amplitude, BB refers to the broadband PPG signal, and FB refers to the filtered broadband PPG signal of our simulations.

3.4.2 Simulation validation results

The RR values calculated from the fluence values at the detector locations from the MCX simulations are shown in Figure 3.9. Traditional two-wavelength transmission simulations showed a

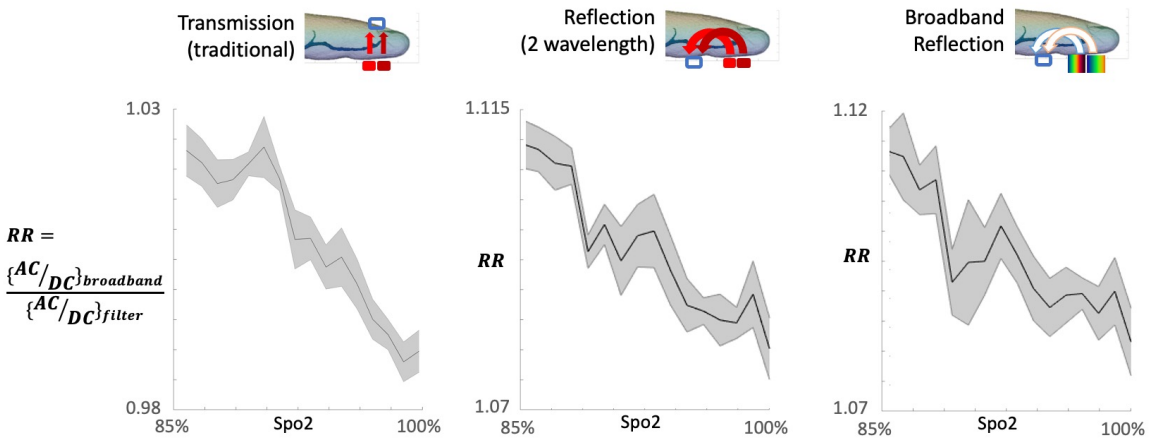

Figure 3.9: Results of ratio-of-ratio mapping to arterial blood oxygen saturation based on Monte Carlo simulations. The curves are shown for two-wavelength simulations in transmission, two-wavelength simulations in reflection, and broadband simulations in reflection.

typical linearly decreasing relationship between RR and SpO_2 as expected. The difference between the maximum and minimum RR is 0.0795. In traditional two-wavelength reflection mode, the range of RR dropped to 0.0519. This indicates that transmission mode is more sensitive to changes in RR, and thus to changes in SpO_2, than reflection mode.

For broadband simulations, the range of RR was 0.013 for transmission mode, dropping by nearly six times as compared to traditional transmission simulations. The difference between RR ranges in traditional and broadband simulations in reflectance mode was about an order of magnitude, with a maximum RR range of 0.005 for broadband reflectance simulations.

Despite the sensitivity of a traditional two-wavelength transmission pulse oximeter simulation being fifteen times higher than the broadband reflectance simulation, the broadband reflectance simulation relationship between RR and SpO_2 is still linear. These results validate our hypothesis that our smartphone-based pulse oximeter can differentiate between SpO_2 values using the embedded broadband light from the smartphone's LED, as long as the sensitivity of the smartphone camera is large enough. Additionally, extra care must be taken to block ambient light and reduce motion artifacts to be able to decouple physiological changes from environmental ones.

3.4.3 Pilot clinical testing

A clinical study was designed to simultaneously capture measurements from our mobile phone low-cost paper filter broadband pulse oximeter (MOXI) and a reference device (Rad87, Masimo, USA). The study was conducted on twenty-nine healthy volunteers at the Massachusetts General Hospital Translational Clinical Research Center.

3.4.3.1 Breath-holding procedures

The clinical pulse oximeter finger clip was attached to the middle finger of the right arm while the index finger rested on the lens of the Pixel 2 smartphone modified to carry a paper filter that partially covers the lens. Measurements were collected simultaneously using our in-house developed mobile application, Moximeter. Subjects were asked to exhale and hold their breath for as long as they comfortably could. This was repeated three times, with two minutes to recover in between. Subjects were told to begin breathing immediately if their oxygen saturation according to the clinical pulse oximeter device dropped below 90%.

3.4.3.2 Data processing

The Moximeter application controlled the smartphone's LED flash and sampled the camera view at 15 Hz. The average pixel intensities of the top and bottom quarter of the camera's image were used to generate the broadband and filtered broadband PPG signals. The Moximeter mobile phone application then applies a Chebyshev Type II filter to remove the non-systemic heart rate signal. The PPG signals are then band-pass filtered using a sixth-order zero-phase Butterworth filter to remove out-of-bound noise (0.2 to 5 Hz). RR is calculated over a 1-second sliding window along the entire time trace. In order to directly compare with the Masimo pulse oximeter, which only outputs SpO_2 readings every second, data from the mobile application needed to be converted to SpO_2 values. This was done using Dr. Hossein Hakim's conversion [84]: $SpO_2 = 110 - 25 \times RR$. This conversion assumes a transmission pulse oximeter. Our clinical dataset was fit to the Masimo pulse oximeter to generate a new SpO_2 calibration curve of $SpO_2 = 109.59 - 54.69 \times RR$. Readings were averaged within 1-second bins to directly compare to the 1 Hz Masimo SpO_2 values.

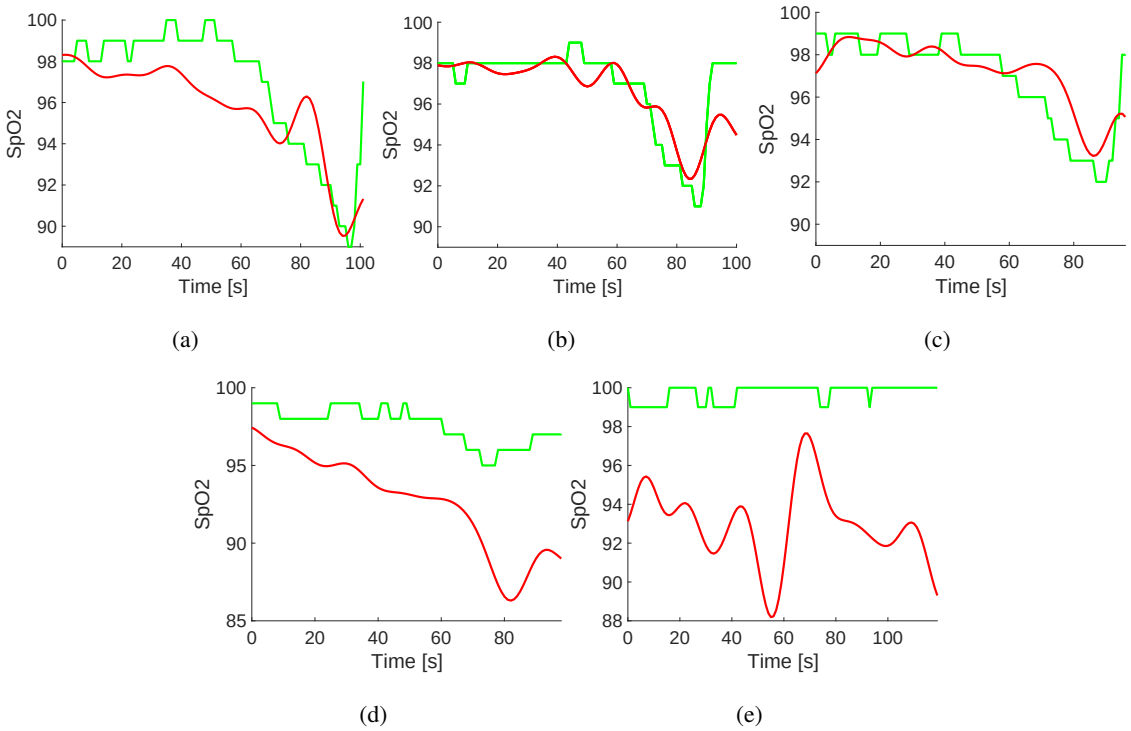

Figure 3.10: Results from comparison of MOXI, our broadband reflectance-based oximeter, with a clinical grade pulse oximeter. Green lines indicate clinical pulse oximeter readings sampled at 1 Hz. Red lines indicate calculated arterial blood oxygen saturation measurements using our broadband oximeter.

3.4.3.3 Pilot test results

Selected results from this MOXI pilot study are shown in Figure 3.10. In many cases [Figures 3.10(a), (b), and (c)], we observe a strong overall correlation between SpO_2 readings from our paper filter (red lines) and the finger-clip style Masimo clinical grad pulse oximeter readings (green lines). Figure 3.10 shows that our D3 design captures the expected delay in SpO_2 drop after initial breath holding. Additionally, the D3 readings correlate well with the minimum SpO_2 values determined by the Masimo baseline.

In some cases, while the overall trends seem to agree, the range of the SpO_2 values differ between the D3 design and the finger-clip oximeter [Figure 3.10(d)]. In other cases, uncorrelated signal recordings were observed [Figure 3.10(e)]. This seems to indicate that the RR to SpO_2 conversion may need to be better calibrated or that MOXI may be highly susceptible to motion artifacts.

Due to the low-cost nature of our pulse oximeter, and the inherent motion in broadband-based oximeters, the signal variability is quite high. As a result, more advanced signal-processing techniques should be further explored and make these measurements practically useful. Nevertheless, the matching between our ultra-low-cost pulse oximeter readings to the Masimo device in some of the subjects is quite encouraging.

3.5 Discussion

The devices above all explore how leveraging mobile phones can be advantageous to scaling the use of pulse oximeters in LMICs. The D1 device leverages a mobile phone for power, display, and storage of readings. Although its implementation is the most traditional of the three devices, the D1 device does possess unique scalability advantages. Typically, finger-clip pulse oximeters display SpO_2 measurements on a small screen on the device but require a connection to a computer in order to save the readings. By leveraging mobile phones, our D1 device can not only store a history of past readings but can also easily share them with remote healthcare providers. Additionally, the Bluetooth connection allows a single mobile phone to connect to multiple devices for use in resource-starved clinics. Scalability is also achieved by the non-contact design of the D2 device since it requires very low power and can be used by multiple patients in a single site. By far, however, MOXI is the most portable, requiring merely a colored piece of paper attached to a mobile phone's camera. Although different colors of paper filters should be explored, we can reasonably

assume that using the same phone model and paper manufacturer would achieve comparable results. Scalability can be easily achieved by simply distributing and downloading a mobile application onto already ubiquitous smartphones.

CHAPTER 4

Modular Optical Configuration Analyzer (MOCA)

This chapter is part 1 of 2 of the work addressing the second challenge described in Chapter 1. This chapter will focus on Modular Optode Configuration Analyzer (MOCA), a software workflow created with the intention of simplifying the design of new modular fNIRS systems. Although a modular architecture brought about advantages such as portability and high-density probes, our investigation quickly lead to an unanticipated challenge. As we explored ways to connect modules and methods to efficiently acquire large amounts of data, we realized the vast number of potential design inputs that affect the final performance of a probe. Additionally, we did not have a standardized method to compare our designs with existing modular fNIRS designs. There was simply no way for researchers to systematically perturb the various design parameters that must be considered when designing new fNIRS systems, so we built one. In this way, the scalability of the modular architecture attribute is achieved by making our tool open-source, facilitating the comparison of existing and design of new modular fNIRS systems. This chapter will detail the MOCA platform while Chapter 5 will describe the fNIRS system built to translate neuroimaging into natural settings.

4.1 Introduction

FNIRS is an emerging neuroimaging technique to non-invasively measure brain activity using non-ionizing light [61]. Unlike functional magnetic resonance imaging (fMRI) [95] that requires high-strength magnetic fields and large scanners, fNIRS utilizes NIR light to detect brain

activation by measuring the associated hemodynamics. The portability of fNIRS positions it as a competitive imaging modality to address some of the challenges of conventional neuroimaging techniques, such as fMRI and magnetoencephalography (MEG), including a lack of wearability for continuous monitoring, limited temporal resolution, and need for subject immobility during use [22]. It has shown great promise for safe and long-term monitoring of brain activity and is increasingly used in studies for behavioral [96] and cognitive neurodevelopment [97, 98, 99, 100], language [101, 102], psychiatric conditions [103, 104], stroke recovery [105], and brain-computer interfaces [106, 107, 108].

Despite exponential growth in the number of applications [60, 109] and publications [22] in recent years, many fNIRS systems still employ fiber-based, cart-sized instrumentation [62] that place limits on both channel density and the use of fNIRS in natural environments. Although fiber-based high-density [110] and portable [111] fNIRS systems have been demonstrated, the use of fragile fiber optics cables, stationary external source/detector units [112, 113], and the need for individual and specialized headgear for specific tasks have motivated the fNIRS community to investigate more flexible modular and fiber-less designs [114, 115].

The modular fNIRS architecture is based on utilizing elementary optical source and detector circuits (modules) as repeating building blocks to form a re-configurable probe [114]. This modular architecture offers significantly improved portability, scalability, flexibility in coverage, and fabrication cost [114]. By avoiding the use of fragile optical fibers, modular fNIRS systems permit the use of light guides to directly couple light sources and detectors to the scalp, significantly reducing signal loss due to fiber coupling. The lightweight and compact modules also make wearable fNIRS and continuous monitoring in mobile environments possible [22, 20]. In addition, the ability to use both intra-module (within a single module) and inter-module (source and detector on different modules) channels allow for high-density probes with varying source-to-detector separations (SDSs) that increase measurement density and tissue depth sampling, resulting in enhanced signal quality, and easy removal of physiological noise [116].

Despite these perceived benefits, the task of designing a modular fNIRS probe can quickly grow in complexity as the number of modules increases. While parameters can be empirically determined when designing a single module, understanding the trade-offs among a large array of parameters, including module shape, module size, optode quantities, and optode locations, and each parameter's effects on the final probe can become a daunting task. Not only do most published modular fNIRS studies largely focus on the design of a single module without addressing the effect of these module- and probe-level parameters on the final probe, but the current literature also does

not provide a means to compare probes composed of different module designs.

Aside from the challenges of determining these modular probe core parameters, other factors such as mechanical, ergonomic, safety, usability, optoelectronic, and data communication considerations [114] also play important roles in achieving the desired performance. For example, mechanical features such as optical coupling and electronic circuitry encapsulation must be considered alongside ergonomic considerations such as comfort, weight, and robustness. Additionally, the use of high-density light sources in such modular probes brings about additional safety considerations, such as heat dissipation, driving voltage, and battery life. Moreover, optoelectronic considerations arise from the use of specialized optodes with narrow emission bandwidths, high gains, low noise, and fNIRS-optimized wavelengths. Not only are these specialized optodes more expensive due to their niche applications and characteristics, but they also require more complex control electronics for driving optodes and acquiring data. With such dense coverage, complex encoding strategies such as frequency multiplexing [117] become a necessity for obtaining high-density data acquisition to achieve sufficient spatial and temporal resolution. Finally, while previously reported modular fNIRS systems often employ daisy-chain communication protocols to connect multiple modules on a single bus [118, 119, 120, 121, 122], the design of physical inter-module connections [123], the synchronization method between modules [114], and the transfer of acquired data become increasingly complex with high module counts and branching connections.

Along these lines, a number of fNIRS data analysis packages exists [124, 125, 126]. However, they focus on the statistical analysis of the data [126, 124, 125] to enhance its quality and provide guidance on post-processing steps such as motion artifact correction [124]. While some other tools exist to assist in the probe design [127, 128, 129, 130], most of these tools are designed to work in a highly constrained design space, where the probe parameters are mostly pre-determined by the user. As a result, the best practices and trade-offs in modular probe design such as tessellation, connection, or re-orientation are poorly explored and understood. Therefore, the community is in great need of an easy-to-use software tool to assist the exploration of and quantitative comparisons among countless parameter choices in a modular probe design and to perform a limited degree of optimization within a well-constrained configuration.

A fully-automated probe design and optimization pipeline is impractical without application-dependent design constraints. Instead, we report a simplified, easy-to-use software toolbox to help designers navigate the vast parameter space of a modular probe. We also share a number of fundamental modular probe design strategies, discovered through our explorations via this toolbox, that are not widely recognized or previously studied. The entire workflow has been imple-

mented into an open-source, MATLAB-based toolbox called Modular Optode Configuration Analyzer (MOCA [131]). MOCA supports a list of commonly used module shapes, user-defined optode layouts, and ROI coverage, and can produce quantitative performance metrics such as distributions of SD separations, sensitivity maps, and spatial multiplexing groupings. These performance metrics also allow comparisons between different designs of modular probes. Although MOCA is not designed as a fully-automated software that produces "optimal" probes regardless of application, its unique capability to describe and sweep modular probe parameters in operator-guided interrogations offers valuable perspective to start approaching the complex modular hardware design problem and make informed comparisons between well-constrained design choices.

The remainder of the paper is outlined below. In Section 4.2, we discuss the relevant design considerations when developing a modular probe using MOCA. We specifically focus on the parameterization of the modules, processes required to assemble modules into functional probes, and related performance metrics for system characterization and comparisons. In Section 4.4, we demonstrate MOCA's capability in designing full-head probes using a variety of module shapes and compare their trade-offs regarding channel density, SD separations, and average brain sensitivities. Furthermore, we utilize MOCA to showcase potential improvements to published fNIRS probes by altering module orientations, spacing, and staggering layouts. In Section 4.5, we highlight a number of generalizable design strategies that were discovered via our experiments using MOCA, including the importance of considering module orientations, tiling strategies, and module spacing tuning, among others.

4.2 Modular Probe Parameters and Performance Metrics

A diagram showing the overall design process of a modular fNIRS system is shown in Figure 4.1. Specifically, the three parts describing MOCA's workflow are 1) the design parameters describing a single module design, 2) the processes and parameters used to assemble the modules into a probe, and 3) the derived performance metrics used to characterize the resulting probe. MOCA starts with the definition of essential module parameters (shown in the left column in Figure 4.1), applies those parameters along with probe-level constraints to a probe-generation process (center column in Figure 4.1), and derives quantitative performance metrics of the resulting probe (shown in the right column in Figure 4.1). Arrows in Figure 4.1 define dependencies between the derived performance metrics and the input parameters. For example, in order to calculate the probe's channel distribution, one must define the module geometry, ROI, and optode layout design

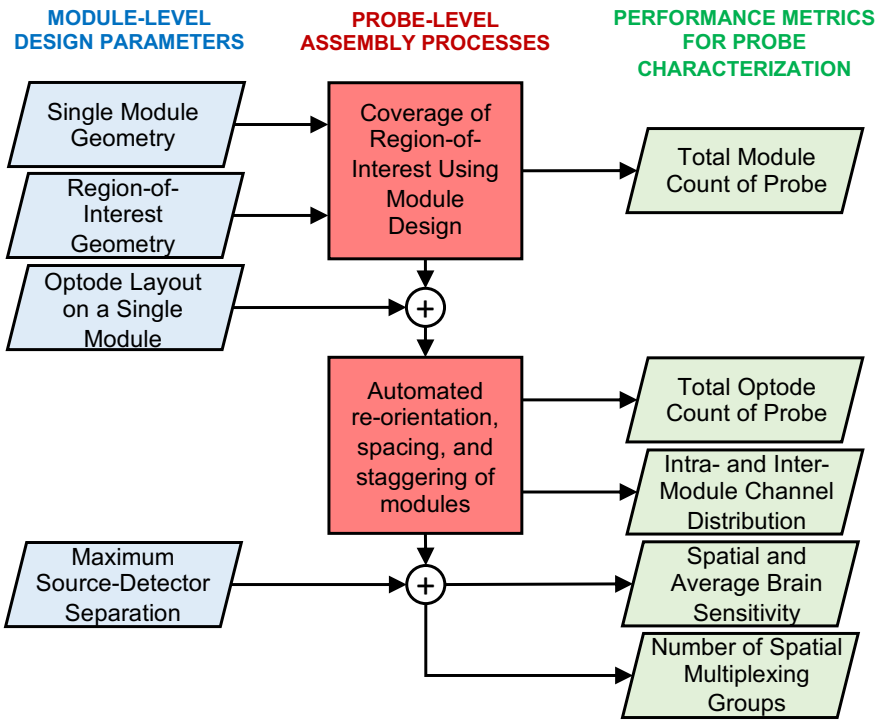

Figure 4.1: Workflow of module-level design parameters (left column; blue) used in probe-level processes (center column; red) to produce performance metrics to characterize a probe (right column; green). Performance metrics are organized top to bottom from least complex (two parameters needed) to most complex (four parameters needed). Arrows trace how parameters are used to derive specific performance metrics.

parameters.

4.2.1 Essential module-level design parameters of fNIRS modular probes

The basic building block of a modular probe is an fNIRS module. It is typically in the form of an optoelectronic circuit made of a rigid [118, 119, 122, 132] or rigid-flex [133, 134] substrate with on-board light sources, optical sensors, auxiliary sensors, microcontrollers, and other communication electronics. A modular probe is subsequently constructed by replicating and interconnecting multiple identical modules. Therefore, the design decisions regarding the module-level parameters are highly important and directly impact the functionalities and restrictions of the resulting probe.

4.2.1.1 Single module geometry

The shape of a module is one of the key parameters when designing a modular system. In the published literature, simple polyhedral shapes, especially equilateral polygons (square, hexagon, etc), are typically used due to their simplicity to fabricate, analyze, and tessellate over a target ROI. It is also possible to design probes that combine multiple polygonal shapes, such as a combination of hexagonal and pentagonal modules. Such hybrid-shape modular systems may bring advantages in tessellating curved surfaces, but they also require more complex analyses. MOCA supports a number of built-in module shapes including three equilateral polygons (triangle, square, hexagon). In such cases, the module edge length is the only shape parameter that needs to be defined. One should be aware that a small-sized module requires a large number of boards to cover a given area, thus resulting in higher fabrication costs and higher complexity in assembly and analysis. Moreover, a small module size also limits the maximum intra-module SDS. Shorter SD separations are known to be more sensitive to superficial tissues rather than brain activities. On the other hand, a small-module size provides better probe-to-scalp coupling when a rigid-board-based module is used. MOCA provides support for user-specified arbitrary polygonal modules, defined by a sequence of two-dimensional (2-D) coordinates. Subsequent analyses of these user-defined arbitrary module shapes only use the bounding box of these polygons when varying probe-level parameters.

4.2.1.2 Target regions-of-interest

An ROI refers to the area of the scalp directly above the cortex for which brain activities are expected to occur[135]. For simplicity, here we focus on designing probes based on the coverage

of a 2-D ROI. For generality, MOCA specifies an ROI geometry as a closed polygon made of a sequence of 2-D coordinates. Users need to specify at least three Cartesian coordinates to define a closed ROI. In the future, MOCA can potentially be expanded to support three-dimensional (3-D) surfaces as ROIs through the use of 3-D surface tessellation tools, such as the Iso2Mesh [136] mesh generator and 3-D photon transport modeling tools such as NIRFAST [137] and MCX [53].

4.2.1.3 Optode layout within a single module

Optode layout refers to the spatial arrangement of optical sources and light sensors within the boundaries of a single polygonal module. In MOCA, each source and detector position is defined by a set of discrete 2-D coordinates relative to the module's center. The 2-D coordinates define the center of the active area of the light-emitting-diode (LED), laser, or photodetector. The physical dimensions of the optodes as well as the size and location of electronic components needed to drive each optode are not considered. The SD separations between all combinations of SD pairs are derived based on the optode positions.

4.2.1.4 Maximum source-detector separation and maximum short separation channel

MOCA also considers the maximum SD separation (SDS_{max}) as a key design parameter. Typically, SDS_{max} is determined by the SNR of the detected signal [138]. A large SDS has low detector sensitivity due to the exponential decay of light intensity as SDS increases. This maximum separation limits the number of inter-module channels that emerge from a particular tessellation of modules over an ROI. By default, MOCA considers any SDS below 10 mm to be a short-separation (SS) channel. This threshold can be manually changed to fit any specific optode performance or probe application. MOCA uses 30 mm as the default SDS_{max} [139, 140]. MOCA bounds the SD range by the SS channel threshold and the SDS_{max}.

4.2.2 Probe-level assembly process parameters

A modular probe is constructed when multiple modules are arranged to form a non-overlapping coverage of the ROI area. The final probe is dependent on the tessellation (the number of modules and the spacing between them) and the orientation of each individual module in the probe.

4.2.2.1 Exploring module tessellation and probe spacing

MOCA provides a process to tessellate modules over a user-defined 2-D polygonal ROI, which is generally known as the "tiling" problem in computational geometry [141]. Here, a "complete tessellation" refers to the tiling of an ROI using a single module shape without overlapping or leaving a gap in coverage. Each of the three built-in polygons (triangle, square, hexagon) have the ability to cover a 2-D area [142]. MOCA performs the tessellation by first tiling the module shape along a horizontal axis starting at the lowest vertical coordinate of the ROI until the width of the row composed of adjacent modules is wider than the width of the corresponding segment of ROI the row is tiled over. It then repeats this row-generation process until the height of all the rows combined is larger than the maximum height of the defined ROI. This dimension comparison in both axes accounts for module shapes with non-vertical and non-horizontal sides. For irregular module shapes, MOCA uses the maximum width and maximum height of the defined polygon as the bounding box to create a tiling grid of the module over the ROI. Using the maximum width and height of the ROI as a guide for tiling ensures the full ROI is covered. Although MOCA offsets and flips the three equilateral polygon shapes to prevent gaps, irregular module shapes have inherent gaps between modules when tessellated. Additionally, MOCA accepts manually defined tessellations by reading a sequence of coordinates defining the center of modules to specify each individual module's location within the ROI. Following tessellation, each module is assigned a unique index and an adjacency matrix is constructed to represent which modules are next to one another.

To extend the flexibility of probe creation, users can change probe spacing, the minimum distance between adjacent modules in all directions. Additionally, a module can be manually deleted from the tessellation to allow the probe to more closely follow the boundaries of the ROI or better represent intentional empty spaces in the probe. When individual modules are removed from the probe, the adjacency matrix is re-calculated from the resulting probe.

4.2.2.2 Guiding module orientation and connection routing

Module orientation refers to the rotation of the module along the normal direction of the ROI plane. In a "complete tessellation" of the three equilateral polygon shapes, MOCA appropriately flips and translates modules to prevent gaps and overlaps. For tessellations of irregular shapes, each module is simply placed in the same orientation as it was originally defined. After probe generation, MOCA allows the user to manually change the orientation of individual modules based on their assigned indices. For asymmetric optode layouts, changing the module orientation alters the

SDS of inter-module channels, resulting in different performance metrics.

Additionally, MOCA creates a single sequential path to connect all modules to form a linear data communication bus, referred to as the "routing" process. In such a path, all modules are connected and every module is visited exactly once—a classic problem known as the Hamilton path [143] in graph theory. In most configurations, a Hamilton path is not unique, and computing such a path is known to be an NP-hard problem, i.e. problems that do not have a polynomial complexity when the node number grows. However, due to the limited module numbers commonly used in fNIRS probes, an exhaustive search of the adjacency matrix can typically identify all Hamilton paths in a given tessellation with no more than a few minutes of computation. For any computed path, MOCA then orients each module based on the angle of a vector defined by the center of the oriented module and the center of the following module in the path. The orientation angle is relative to the horizontal axis.

4.2.3 Performance metrics to characterize probes

Each metric described below changes as module- and probe-level parameters are altered either manually or through MOCA's sweeping functions. MOCA not only helps unravel the complex interplay between choices of different parameters but also guides the probe designer in making trade-offs between conflicting design targets—improving one metric may come at the risk of worsening another. We have chosen the following set of essential performance metrics due to their ability to easily inform a breadth of end-user probe requirements such as cost, weight, depth sensitivity, and sampling rate estimates.

4.2.3.1 Total module and optode counts

Based on the module design and tessellation, MOCA computes the total number of modules, n_m, needed to cover the ROI. In addition, MOCA also outputs the total number of sources (n_s) and detectors (n_d) of the final probe. All modules, sources, and detectors of an assembled probe are given unique identifiable index numbers (m_i, s_i, and d_i, respectively). Module and optode counts are performance metrics outputted by MOCA from which cost, weight, and power estimates can be deduced.

4.2.3.2 Inter- and intra-module channel distribution

For any assembled probe, MOCA generates histograms of the SD separations for all combinations of SD pairs. Particularly, it outputs separately the distribution of inter- and intra-module channels that are below the SDS_{max} previously defined by the user. These channel distributions aid the user in designing the probe based on the targeted application and population. For example, shorter channels are more applicable to infant populations. Additionally, MOCA outputs channel density, a metric commonly used for fNIRS probe benchmarking. Channel density is defined as the number of channels, $n_{channels}$, divided by the area of the ROI [114]. Furthermore, MOCA can provide a spatial plot overlaying channels on the assembled probe, allowing for visual inspection of low channel density areas within the probe.

4.2.3.3 Spatial brain sensitivity

Brain sensitivity (S_{brain}) refers to the magnitude of the measurement signal change at a detector given a localized perturbation of optical properties of brain tissue [144]. A higher S_{brain} value suggests the probe is more sensitive to the anticipated brain activation. It is calculated from the spatial probability distribution of photons scattering through complex tissue as they travel from the source to the detector [145]. Although modeling 3-D head/brain anatomies and 3-D based light simulations have been reported, including several related works from our group [136, 146, 147, 148], we deliberately chose a simplified layered-slab head model and 2-D based probe layout as default models to evaluate a modular probe in MOCA. Such a decision was largely motivated by 1) significantly faster computation and pre-/post-processing to accommodate fast sweeping of a large parameter space, and 2) avoiding another added layer of complexity when probe design is coupled with underlying brain anatomy in a 3-D head model. A comparison between S_{brain} computed by 2-D and atlas-based analyses is provided in the Results section of this chapter. Nonetheless, MOCA can export 2-D probe data to established 3-D probe modeling toolkits, such as AtlasViewer [130] and MCX [136], to perform more advanced analyses when 3-D head models are necessary.

MOCA uses a five-layer slab model consisting of tissue imitating the scalp, skull, cerebral spinal fluid (CSF), white matter (WM), and gray matter (GM) to determine the spatial sensitivity profile for each SD pair in a probe [149]. The thickness of each tissue layer in the slab is set to the average thickness of that tissue type computed using the top half of a tetrahedral brain model [150]. We define the brain region as the combination of gray matter and white matter tissues. The optical properties and resulting thicknesses for each tissue type are summarized in Table 4.1.

Table 4.1: Optical properties used in the slab model for calculating brain sensitivity. The thickness of each layer is derived by dividing the total tissue volume by the tissue's surface area from a tetrahedral five-tissue brain model. The absorption coefficient, μ_a, is the average path a photon will travel in the medium before being absorbed. Similarly, the scattering coefficient, μ_s, defines the average path length of photons before a scattering event. Anisotropy, g, is a unit less measure of the amount of forward direction retained after a single scattering event.

Tissue Type	μ_a $[mm^{-1}]$	μ_s $[mm^{-1}]$	g	Thickness $[mm]$
Gray Matter	0.020	9.000	0.89	7.25
White Matter	0.080	40.900	0.84	4.00
Cerebral Spinal Fluid	0.004	0.009	0.89	2.73
Skull	0.019	7.800	0.89	3.29
Scalp	0.019	7.800	0.89	4.23

For each SD pair in the assembled probe, 3×10^8 photons are simulated using our in-house 3-D Monte Carlo photon transport simulator, MCX [136], using a pencil beam source and a single 1.5 mm radius detector placed at the surface of the slab at its corresponding SDS. In a voxelated grid, S_{brain} is defined as a ratio dividing the region-wise summation of the sensitivity matrix in each brain tissue region by the summation of the entire sensitivity matrix for each source-detector separation [145], i.e.

$$S_{brain}(s,d) = \frac{\sum_{r\in\Omega_{GM}} J(r,s,d) + \sum_{r\in\Omega_{WM}} J(r,s,d)}{\sum_{r\in\Omega} J(r,s,d)}, \tag{4.1}$$

where the sensitivity matrix, also known as the Jacobian (J), is computed using the adjoint Monte Carlo method [26]. In addition to S_{brain}, MOCA also calculates the average brain sensitivity for the entire probe, $\overline{S_{brain}}$, based on all the SD separations above the SS threshold. SS channels are excluded in the calculation of $\overline{S_{brain}}$ because, by definition, they are designed to only sample superficial layers [145].

4.2.3.4 Spatial multiplexing groups

The density of assembled modular probes may impact the probe's temporal sampling rate when illuminating each source sequentially. MOCA introduces spatial multiplexing, an encoding strategy that can potentially accelerate data acquisition by simultaneously turning on multiple light sources at the same time. Because of the high attenuation of light in the head and brain tissues at large separations, MOCA can ignore the cross-talk of light sources that are far away for a given detector and assign sources into a spatial multiplexing group (SMG) so that all sources within an SMG can be turned on simultaneously. By default, MOCA uses the SDS_{max} as the minimal distance be-

tween sources. This distance, however, can be defined by the user. Notably, unlike frequency multiplexing, spatial multiplexing does not require extra energy-intensive hardware or post-measurement separation of combined signals.

The search for the SMG starts by randomly specifying a source position as the seed; a circle of radius SDS_{max} centered at the seed position is drawn and a random source outside of this circle that is at least $2\times SDS_{max}$ away is picked; the above process repeats until no additional source can be found. Once an SMG is identified, a new source that does not belong to any existing SMG is selected as the new seed for the next SMG, and the above process repeats until every source is allocated. The total number of spatial multiplexing groups, n_{SMG}, depends on the tessellation of the module over the ROI as well as the choice of the seed position. As with channels, the n_{SMG} are for a single wavelength. Thus, when estimating the total sampling rate of the probe using dual-wavelength sources, the control unit must cycle through each group twice (once for each wavelength).

In addition to n_{SMG}, MOCA calculates the spatial multiplexing ratio (SMR), defined as $SMR = n_s/n_{SMG}$. This ratio is interpreted as the acceleration factor of the data acquisition speed when using spatial multiplexing. For example, for a 20-source probe, an n_{SMG} of 5 can accelerate the data acquisition by a factor of $SMR = 20/5 = 4$ fold.

4.3 Additional Functionalities

MOCA was created as an exploratory tool to interrogate specific design parameters and reveal the trade-offs, within a well-constrained search space, regarding specific design decisions. MOCA possesses functions to facilitate changing probe-level parameters and exporting the desired probe for use in existing probe design tools such as AtlasViewer.

4.3.1 Parameter sweeping

4.3.1.1 Altering spacing between modules

An optional parameter during module tessellation is probe spacing—a uniform distance assumed between adjacent modules. The spacing sweep function varies the probe spacing within a user-defined range in user-defined increments. For the three built-in polygons (triangle, square, hexagon), spacing is increased between all adjacent sides of the modules within the probe. For arbitrary shapes, spacing is added to the horizontal and vertical sides of the rectangular bounding

box. The number of modules required to cover the ROI is continuously adjusted as probe spacing is varied. The performance metrics for each of the resulting probes are reported by MOCA as a function of probe spacing.

4.3.1.2 Exhaustive search of module orientations

MOCA provides a limited orientation enumeration function to re-orient modules through a predefined number of orientations. For the three built-in polygons, the default number of re-orientations per module is simply the number of sides of the polygon. For arbitrary shapes, the default number of re-orientations is four based on the bounding box. Additionally, a user can describe the number of orientations for any shape. MOCA re-orients modules in evenly spaced angle increments. An exhaustive search is performed using the number of modules in the probe and the number of user-defined orientations. Each probe resulting from each permutation of module re-orientations is characterized by MOCA and reported as a function of various probe layouts.

4.3.1.3 Staggering rows of modules

Staggering modules refers to shifting a row (or column) of tessellated modules in the x (or y) axis. Staggering is performed on tiling grid probe layouts. Adjusting this probe-level parameter is particularly useful for improving probes composed of modules with symmetrical optode layouts, where re-orienting modules does not affect SDS, or when high-density probes are needed, where probe spacing cannot be increased. A user defines both the range and increment by which to offset a particular row. Each resulting probe is analyzed and the corresponding performance metrics are calculated. MOCA then reports a plot of the $\overline{S_{brain}}$, spatial multiplexing ratio, and the number of channels for each staggered probe.

4.3.2 Exporting probes for use in AtlasViewer

MOCA performs its analysis of module- and probe-level parameters on an infinite slab model derived from the Colin27 atlas. When 3-D analysis is desired, MOCA can export the probe layout to a ".sd" file for use in "SDgui" – a built-in tool of AtlasViewer [130] used for creating and editing ".sd" files. To properly represent a modular probe layout in AtlasViewer (which treats all optodes individually without a reference to a module), MOCA first translates the module-level parameters by creating fixed/rigid springs between all optode pairs (source-source, source-detector,

and detector-detector) within each module. These fixed springs maintain the relative optode layout within each module while permitting bending at the junctions between springs. MOCA then adds fixed springs between each inter-module channel (SD pairs between modules with distances below the SDS_{max}) to translate the probe-level parameters (spacing, orientation, staggering). As an additional constraint, MOCA adds flexible springs (springs of length -1) for inter-module channels above the SDS_{max}. Finally, to register the probe to the surface of the selected atlas, MOCA adds three dummy optodes to the exported ".sd" file. All three optodes are placed at the midpoint between the minimum and maximum x coordinates of all optodes in the probe. The y coordinate of the first, second, and third dummy optodes are set to the minimum y coordinate, midpoint, and maximum y coordinate of all optodes in the probe, respectively. The first, second, and third dummy optodes are assigned to the "Fpz", "Cz", and "Oz" positions, respectively, in the standard 10-10 system. This places any MOCA-designed probe at the top of an atlas by default. A user can change the dummy optode anchors to re-position the probe on an atlas. The exported ".sd" file can then be loaded into AtlasViewer for placement on a generic or subject-specific atlas (Figure 4.2).

4.4 Results and Practical Examples

In this section, we first validate the S_{brain} derived from a simplified five-layer slab model against previously published atlas-based S_{brain} results [144]. Then we demonstrate how the module-level parameters of MOCA can be used to characterize and compare full-head probes composed of different choices of elementary module designs. Lastly, we show examples using MOCA's assembly processes as investigational tools to potentially improve existing designs by altering probe-level parameters such as probe spacing, module orientations, and the staggering of modules within an assembled probe.

4.4.1 Slab-based brain sensitivity corresponds with atlas-based sensitivity

Figure 4.3 shows S_{brain} calculated using our five-layer slab model at SD separations ranging from 1 to 60 mm in 1 mm increments (blue line). We also overlay full-head averages of S_{brain} and standard deviations at 20, 25, 30, 35, and 40 mm separations from a previously published study [144] using the Colin27 atlas.

Simulations on a five-layer slab model show an increase in S_{brain} as SDS increases. Additionally, S_{brain} for SD separations below 10 mm is less than 1.17%. At 20, 25, 30, 35, and 40 mm

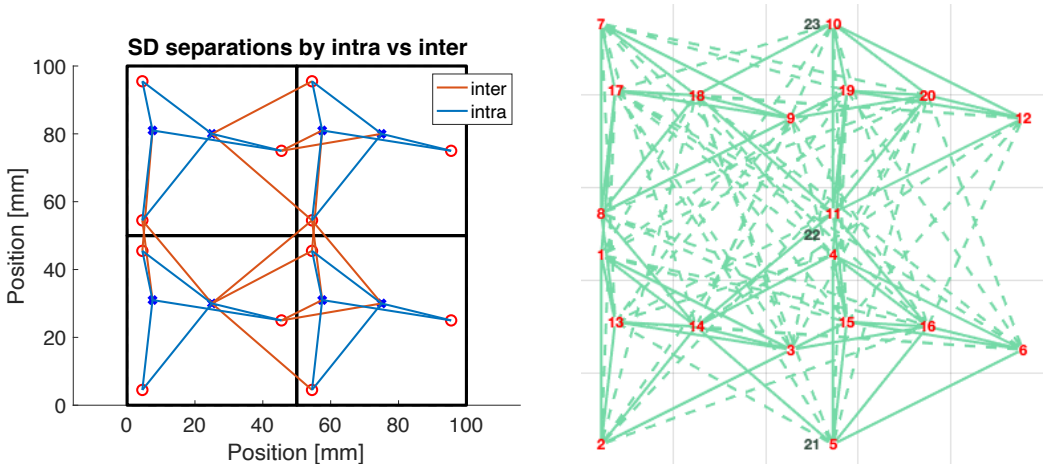

(a)

(b)

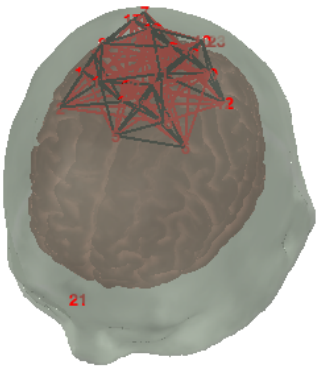

(c)

Figure 4.2: Example probe exported for use in AtlasViewer. (a) A four-module probe with three sources (red circles) and two detectors (blue crosses) plotted using MOCA. Intra- (blue) and inter-module (orange) channels are shown in solid lines. (b) Imported probe in SDgui. Solid lines represent fixed springs. Dashed green lines represent flexible springs between sources and detectors. Three dummy optodes (numbered 21, 22, and 23) are shown in black. (c) The resulting probe in AtlasViewer registered to an atlas using the dummy optodes as anchors.

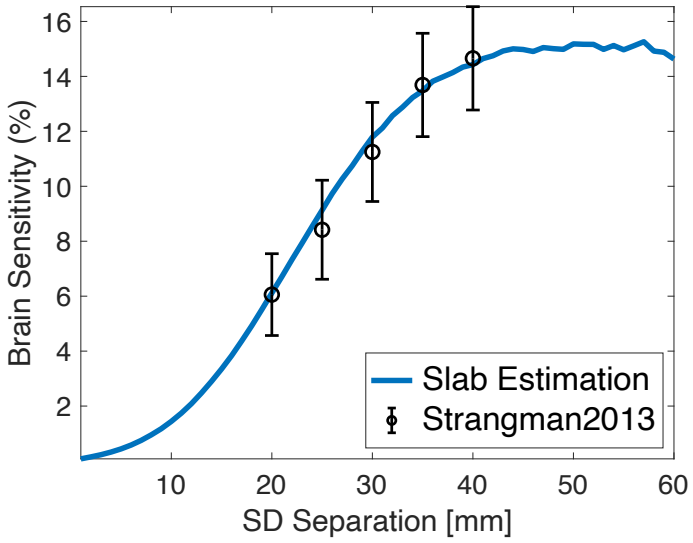

Figure 4.3: Results comparing brain sensitivity derived from finite slab models used by MOCA and atlas-based models. The blue line shows calculated brain sensitivity based on a five-layer slab model for SD separations from 0 to 60 mm in 1 mm increments. Overlaid in black are the brain sensitivity results calculated from an atlas by averaging brain sensitivity for fixed source-detector separations across nineteen locations in the international 10-20 system.

separations, the maximum difference between the atlas-based and slab-based S_{brain} values is less than 0.6%. Figure 4.3 demonstrates that using a 2-D approximation of the ROI and a layered brain structure provides a reasonable trade-off between accuracy and computational efficiency, especially for high-density probe characterization.

4.4.2 Comparison between sample modules of various shapes.

MOCA allows the comparison of a wide range of fNIRS module designs by quantifying the effects of probe-level design parameters on a probe's performance. As a showcase, here we report the results from a comparison of three equilateral module shapes (square, hexagon, and triangle) with the same optode layout tessellated over a 200×200 mm^2 ROI, derived from the average surface area of the top half of an adult male head [151]. Square [118, 119, 120] and hexagonal [121, 132, 122] fNIRS modules have been extensively studied in literature and are chosen here for a quantitative comparison. While an equilateral triangle has not been reported in published module designs, we include it here because of the potential suitability for better tessellation of a 3-D surface in future extensions. With this comparison, we want to demonstrate both the scalability

Table 4.2: Summary of quantitative performance metrics derived by MOCA when tessellating the three elementary module shapes over a 200×200 mm^2 region of interest.

Row	Performance Metric	Square-based probe	Hexagon-based probe	Triangle-based probe
1	Total modules [N]	36	42	40
2	Total optodes [N]	144	168	160
3	Total channels [N]	324	405	496
4	Intra-module channels [N]	180	237	336
5	Inter-module channels [N]	144	168	160
6	% of channels that are inter-module [%]	55.56	58.52	67.74
7	Average brain sensitivity [%]	7.52 ± 1.95	6.50 ± 2.44	8.83 ± 3.10
8	Average intra-module brain sensitivity [%]	6.44 ± 2.10	6.44 ± 2.10	6.44 ± 2.10
9	Average inter-module brain sensitivity [%]	8.82 ± 0.00	6.54 ± 2.66	9.94 ± 2.86
10	Spatial multiplexing groups [N]	9	8	13
11	Spatial Multiplexing Ratio	8	10.5	6.15

of MOCA in analyzing full-head probes and how performance metrics change across module-level design decisions.

As mentioned above, MOCA systematically tessellates the target ROI using the module geometry and assigns each module an index number. If not considering within-module optode locations, only translation is needed for both square and hexagon modules to completely cover a region. For the triangle shape, MOCA rotates every other triangle and its optodes 180 degrees to fill the ROI without leaving any gaps. No other probe-level parameter changes are made for this comparison. Probe spacing is set to zero. The default SS threshold is set to 10 mm and the SDS_{max} is set to 30 mm. The minimum distance between sources used in calculating SMGs is set to $2\times SDS_{max}$. To avoid simultaneously changing multiple parameters and only focusing on module shape, an identical optode layout made of two sources and two detectors is used in all three module designs in this example. The edge length of the square is set to 33.33 mm, determined by the average length of three previously reported square-shaped module designs [118, 119, 120]. The edge length of the hexagon and triangle is set to 20.68 and 50.65 mm, respectively, calculated to achieve the same area as the square module. The three-module designs as well as the tessellation of the hexagon-based probe over the ROI are shown in Figure 4.4. The derived performance metrics for each of the three sample probes are summarized in Table 4.2. The results that follow are only applicable to the specific module- and probe-level parameters chosen for this showcase.

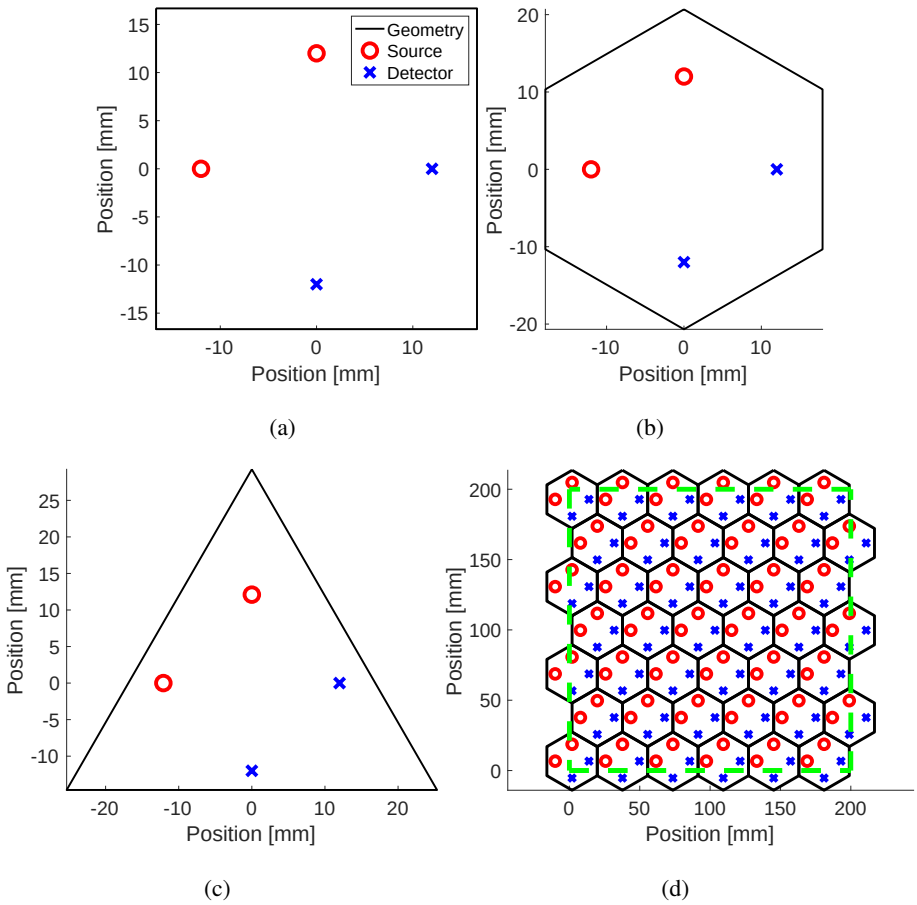

Figure 4.4: Elementary module designs used in a full-head comparison. (a), (b), and (c) show the perimeter of the square, hexagon, and triangle-based module designs, respectively. The optode layout of all three shapes is identical. Red circles represent sources while blue crosses represent detectors. (d) Tessellation of the hexagon module over an ROI. The dashed green line outlines the 200×200 mm ROI.

4.4.2.1 Effect of module shape on channel separation distributions

Figure 4.5 shows a histogram of the SD separations of the full-head (200×200 mm area) probe composed from the three selected module shapes. Table 4.2 shows that the number of modules needed to cover the ROI varies for each shape due to the complete coverage constraint enforced by MOCA for this showcase [Figure 4.5(d)]. Since each module utilizes the same optode layout, the intra-module channel distributions [blue bars in Figures 4.5(a), 4.5(b), and 4.5(c)] are simply scaled by the total numbers of modules needed to completely cover the ROI. The SDS of inter-module channels are dependent on the module shape, resulting in varying inter-module channel distributions between all three probes [orange bars in Figures 4.5(a), 4.5(b), and 4.5(c)].

For this particular example, the triangle-based probe reports both the highest number of total channels [Figure 4.5(d)] and the largest SD separations of all three tessellated probes [Figure 4.5(c)]. The hexagon-based probe appears to have the shortest inter-module channels [Figure 4.5(b)]. Due to its symmetry and given the SDS_{max} setting, the square-based probe happens to have all SD separations at 24 mm. Notably, the triangle-based probe adds the most inter-module channels, almost twice the number of intra-module channels [Figure 4.5(d)], while also requiring two fewer modules than the hexagon-based probe (Table 4.2, Rows 1-5). Figure 4.5(d) also shows that the number of inter-module channels is greater than the number of intra-module channels for all three probes.

4.4.2.2 Combining intra- and inter-module channels for brain sensitivity

The $\overline{S_{brain}}$ values derived from the three probe designs, grouped by intra-module channels, inter-module channels, and all channels, are summarized in Figure 4.6. Only channels above the SS threshold and below the SDS_{max} are used. Despite having the fewest total channels (Table 4.2, Row 3), the square-based probe results in a higher $\overline{S_{brain}}$ than the hexagon-based probe. For the square- and triangle-based probes, the use of inter-module channels increases the probe's $\overline{S_{brain}}$ as compared to simply using intra-module channels alone. For the hexagon-based probe, $\overline{S_{brain}}$ computed using only intra-module channels is similar to that when using only inter-module channels (6.44% vs 6.54%). Due to having the same optode layout, the intra-module $\overline{S_{brain}}$ is the same for all three probes.

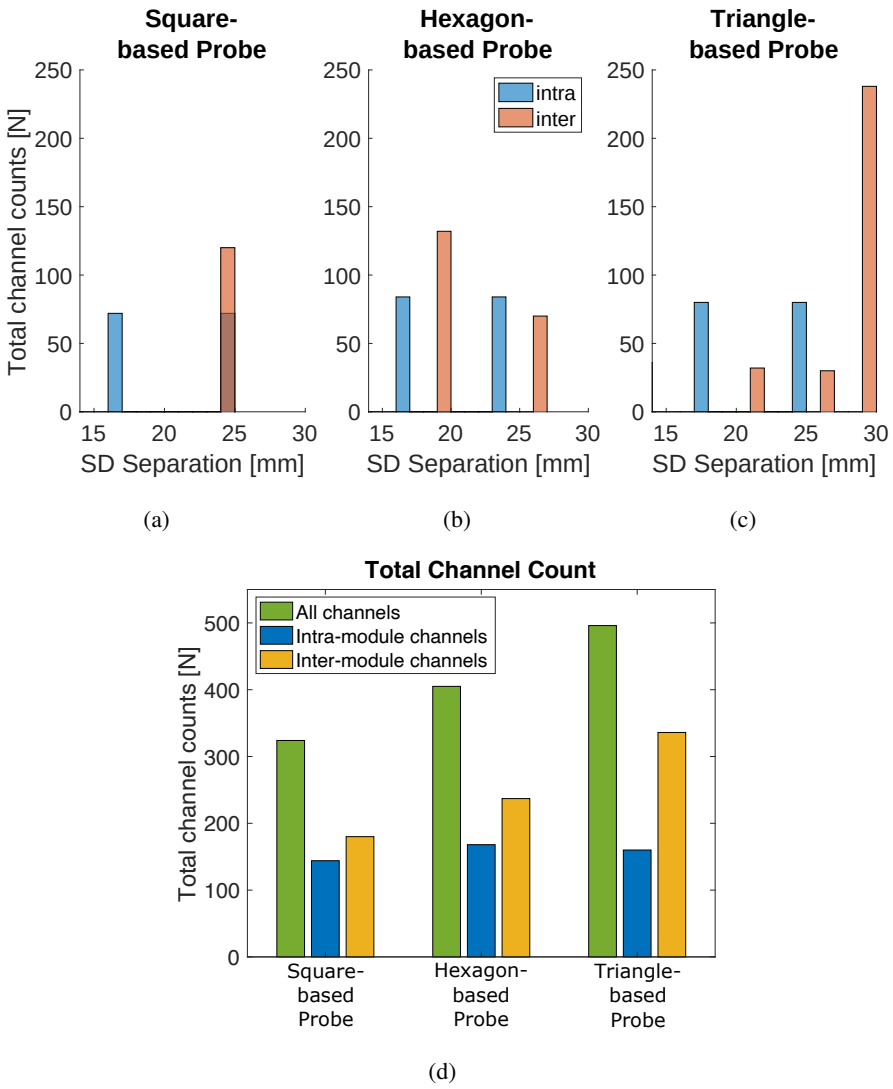

Figure 4.5: Channel distributions and total channel counts resulting from the tessellation of the three elementary module shapes over a 200×200 mm^2 region of interest. (a-c) Resulting intra- and inter-module channel distributions for square, hexagon, and triangle module-based probes. (d) The total channel count of each probe grouped by intra- and inter-module channels.

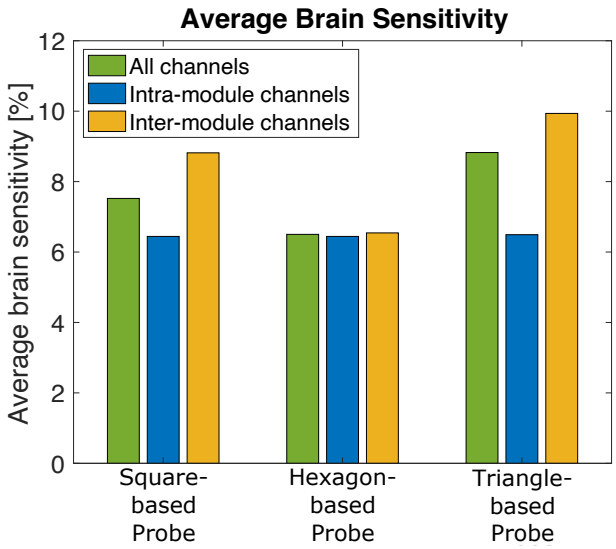

Figure 4.6: Resulting average brain sensitivity organized by intra- and inter-module channels for square-, hexagon-, and triangle-based probes tessellated over a 200×200 mm region. Short-separation channels are excluded from all calculations.

4.4.2.3 Effect of module shapes on improving sampling rate

The total n_s compared to the n_{SMG} arising from the tessellation of each module over the ROI are compared in Figure 4.7(a). The total number of sources for the square-, hexagon- and triangle-based probes are 72, 84, and 80, respectively. Figure 4.7(b) overlays the first SMG over the triangle-based full-head probe. Using the n_{SMG} for each probe (Table 4.2, Row 10), the SMR (the ratio between n_s and n_{SMG}) is 8, 10.5, and 6.15 for the square-, hexagon-, and triangle-based probe, respectively. This result indicates that the hexagon-based probe's sampling rate can benefit the most when using group-based spatial multiplexing.

4.4.3 Improving existing probes through probe-level parameter alterations

The ability to compute performance metrics from basic design parameters allows users to explore probe-level alterations and potentially improve existing probes using MOCA. Here, we simulate and alter published examples to demonstrate how even simple module layout changes such as rotating selected modules, altering probe spacing, and staggering modules can potentially improve published probe designs.

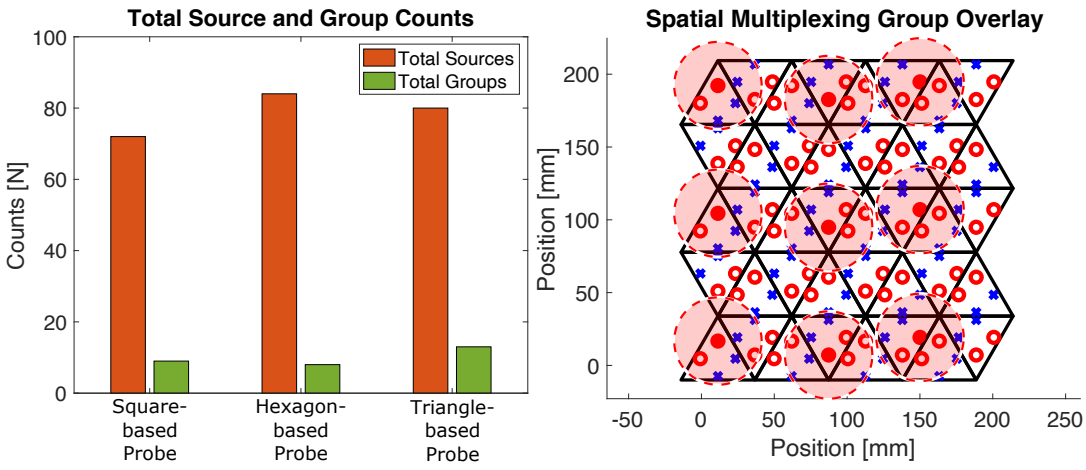

(a) (b)

Figure 4.7: Spatial multiplexing group results from the tessellation of the square-, hexagon-, and triangle-based probes. (a) Comparison of the total number of sources (orange) and the total number of spatial multiplexing groups (green). (b) The triangle-based module tessellation with sources (red circles) and detectors (blue crosses). The dashed red circles indicate the "effective" region (30 mm radius) of each of the nine sources in the first spatial multiplexing group. The nine sources turned on simultaneously in this group are indicated by filled-in red circles.

4.4.3.1 Effect of optode orientation on probe characteristics

Re-orienting modules within existing probes alters the SDS distribution and, consequently, the probe's S_{brain} and SMR. In Figure 4.8, we simulate a 36 mm^2 square module in a probe configuration inspired by the μNTS fNIRS module described in Chitnis *et al.* [118]. The modules in the initial tessellation are oriented in the same direction as in the original paper [Figure 4.8(a)]. In our investigation, the spacing between each module is set to 5 mm and the SDS_{max} is set to 30 mm. Each module has 2 sources and 4 detectors, resulting in 8 intra-module channels per module ranging from 8 to 29 mm. A total of 256 different probe configurations result from exhaustively re-orienting each module individually by 90 degrees. Without losing generality, a subset of 128 layouts are shown in Figure 4.8(b) to show the range of the variations.

Of the 256 possible layout configurations, 8 of those layouts result in a maximum average brain sensitivity of 9.87%. These 8 layouts also achieve the minimum number ($n_{SMG} = 4$) of spatial multiplexing groups. The intra- and inter-module channel distribution and channel count resulting from the MOCA analysis of the original probe layout are shown in Figure 4.8(d). Figure 4.8(c) shows the same 4-module probe but constructed with the bottom-left and top-right modules rotated

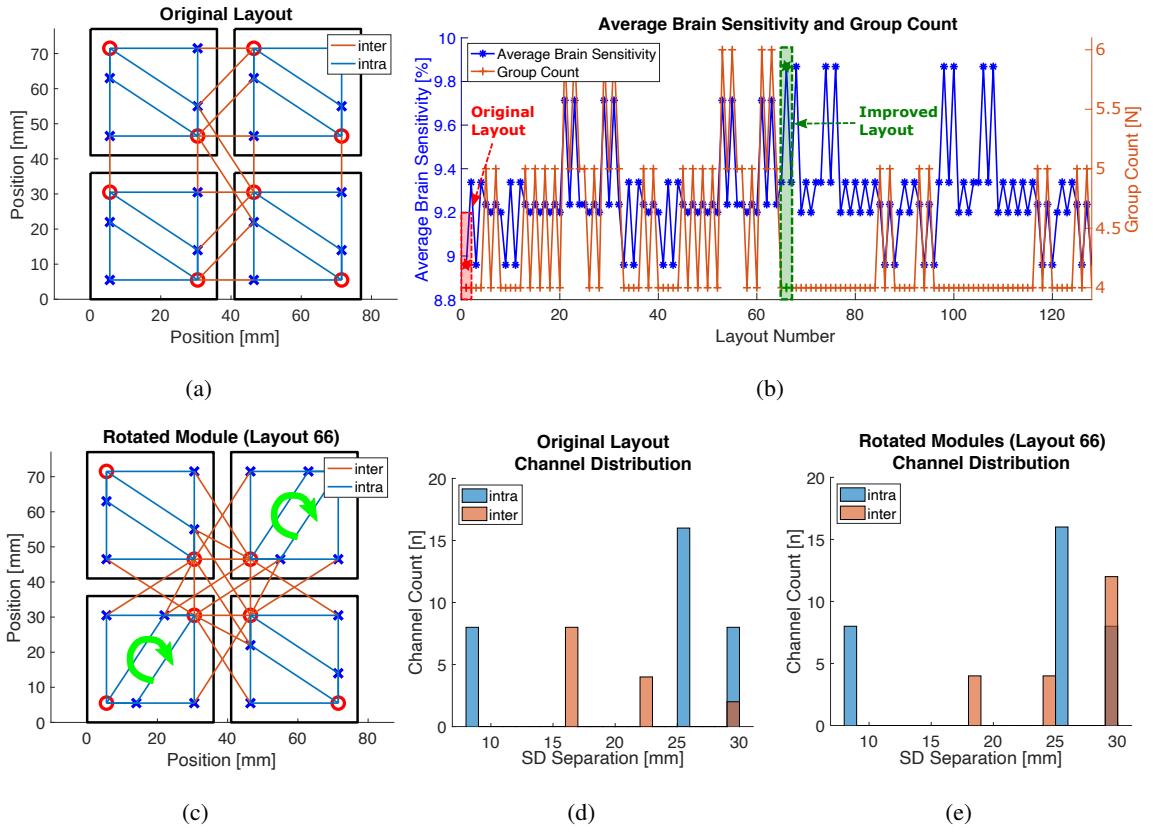

Figure 4.8: A 4-module probe simulated using MOCA. (a) All modules are oriented in the same direction. Red circles represent sources and blue crosses represent detectors. An exhaustive search of all combinations of orientations for each of the four modules results in 256 possible layouts. The average brain sensitivity and number of spatial multiplexing groups for the first 128 layouts are shown in (b). The original layout (layout number 1) is highlighted in the red square. An example layout with the maximum possible brain sensitivity (layout number 66) is highlighted in the green square. (c) A visual representation of layout 66 with the bottom-left and top-right modules rotated 90 degrees clockwise with respect to orientation in (a). Intra- and inter-module channel distribution resulting from the original layout is shown in (d). Channel counts resulting from the probe configuration in (c) are shown in (e). In both channel distribution histograms (d, e), intra- and inter-module channels are shown in blue and orange, respectively. Dark orange indicates overlapping histogram counts.

90 degrees clockwise, corresponding to layout number 66 in Figure 4.8(b). Using MOCA, the spatial channel plot overlaid onto this re-oriented probe shows a denser coverage of the center of the ROI compared to the original probe layout. The channel count distribution of this re-oriented probe is shown in Figure 4.8(e). As expected, the intra-module channels in Figure 4.8(a) and Figure 4.8(c) are identical. However, re-orienting the two modules produces a shift towards longer separation inter-module channels that are known to be more sensitive to brain tissues. The number of inter-module channels within the 10 to 20 mm range decreases from 8 to 4 and the number of 29 mm separation inter-module channels increases from 2 to 12 upon re-orienting the 2 modules. The re-orientation of modules not only allows the probe to have more long-separation channels, but it also increases the total number of inter-module channels from 14 to 20 [Figures 4.8(d) and 4.8(e)). Additionally, $\overline{S_{brain}}$ of the probe increases from 8.56% to 9.87% [Figure 4.8(b)] while the number of spatial multiplexing groups, and subsequently the probe's sampling rate, remains the same.

4.4.3.2 Effect of probe spacing on probe performance

Probe spacing—the distance between edges of adjacent modules in a probe—is a parameter that can vary the resulting channel distribution and channel density of a probe by altering the relative distances between optodes on neighboring modules. To investigate the effect of this parameter, in Figure 4.9, we simulate the probe layout described by Zhao *et al.* [122], which utilizes hexagonal-shaped LUMO fNIRS modules developed by Gowerlabs [152]. The length of each side of the hexagonal-shaped module used in our investigation is set to 18 mm and each module contains three sources and four detectors. The SDS_{max} is set to 30 mm. A uniform spacing is set between all adjacent modules. Probe spacing is varied from 0 to 30 mm in 1 mm increments.

When all modules are densely packed with a spacing of 1 mm, the probe results in 328 total channels (184 of which are inter-module channels), an $\overline{S_{brain}}$ of 5.95%, and 12 SMGs. When the probe spacing is increased to 6 mm, the number of channels and spatial multiplexing groups remain the same while the $\overline{S_{brain}}$ increases [Figure 4.9(b)]. The increase in $\overline{S_{brain}}$ arises due to the overall increased distances between sources and detectors of inter-module channels which sample deeper into the brain tissue. This results in a local maximum $\overline{S_{brain}}$ of 7.87%.

When we increase probe spacing to 8 mm, the inter-module channel separations increase to above the SDS_{max}. This decreases the number of "usable" inter-module channels and the probe's $\overline{S_{brain}}$. The SMR remains unchanged between 6 and 8 mm probe spacing. Above 11 mm, the increase in probe spacing increases the relative distance between adjacent sources, allowing more

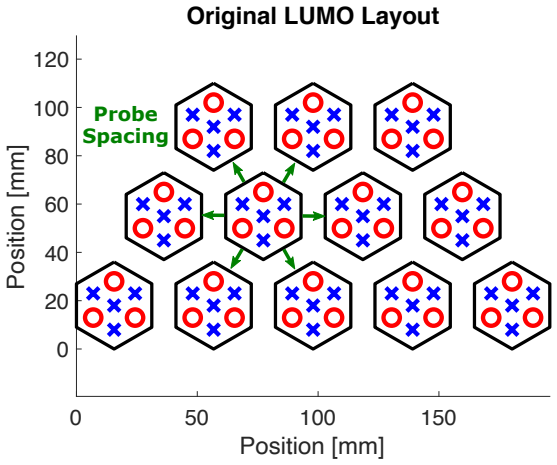

(a)

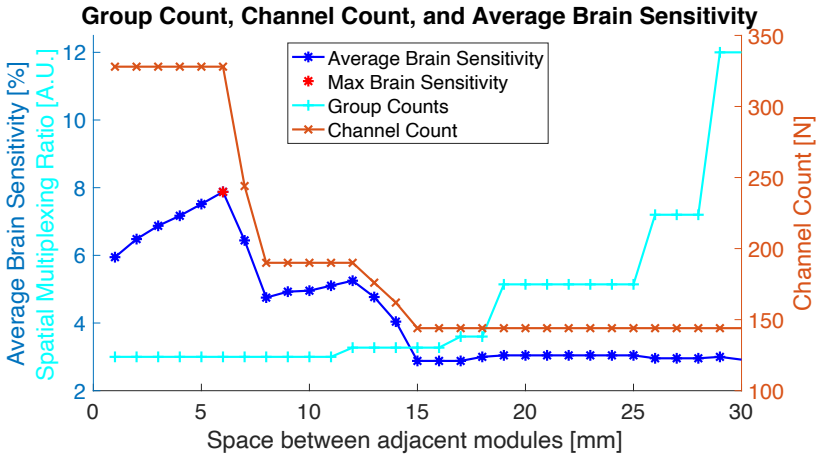

(b)

Figure 4.9: An analysis of hexagonal modules in a twelve-module probe. (a) Green arrows indicate the distances between modules as probe spacing varies. (b) The total channel count, average brain sensitivity, and the spatial multiplexing ratio at probe spacing values between 1 and 30 mm. Module orientations are held constant.

sources to be turned on at the same time and decreasing the n_{SMG} needed. This trend continues as we increase probe spacing. Consequently, the probe's $\overline{S_{brain}}$ reaches a minimal plateau of 3% at 15 mm spacing and beyond because only intra-module channels above the SS threshold remain within the SD range [Figure 4.9(b)]. Similarly, since modules are further apart, the n_{SMG} continues to drop which increases the SMR (and the sampling rate of the probe when spatial multiplexing encoding is utilized). At 29mm spacing, the SMR value is 12 due to only 3 spatial multiplexing groups needed (one for each of the 3 sources on each module).

4.4.3.3 Effect of staggering modules on probe characteristics

Staggering adjacent modules within a high-density probe can increase inter-module SD separations to improve performance. To demonstrate the effect of staggering on the resulting probe, in Figure 4.10 we simulate a 42 mm^2 square module in a 3×1 layout configuration inspired by M3BA modules [119]. Each of our simulated modules contains two sources and two detectors. The probe was staggered by translating the center module between 0 mm and 42 mm along the horizontal axis.

In Figure 4.10(a), we overlaid the intra- (blue) and inter-module (orange) channels over the three-module probe. The resulting channel distribution shows 12 intra-module channels at 28 mm and 4 inter-module channels at 14 mm SD separations [Figure 4.10(b)]. The $\overline{S_{brain}}$ of this probe using all channels is 8.79% [Figure 4.10(c)]. When analyzed separately by intra- and inter-module channels, the $\overline{S_{brain}}$ using only intra-module channels (10.75%) is larger the $\overline{S_{brain}}$ when using only inter-module channels (2.9%) since in this tessellation intra-module channels are larger and probe deeper into the tissue.

In Figure 4.10(c), we show the effect of staggering the tessellated module layout by translating the center module along the horizontal axis. This alteration increases the inter-module channel separations. Consequently, the $\overline{S_{brain}}$ due to only inter-module channels increases until the inter-module channel separations are larger than the SDS_{max}. The $\overline{S_{brain}}$ using all channels increases from 8.79% in the original tessellation to a maximum of 10.95% in the staggered tessellation at 26 mm. The n_{SMG} between the two layouts remained the same until a staggering amount of 31 mm at which point the sources are far away enough to group them together [Figure 4.10(f)].

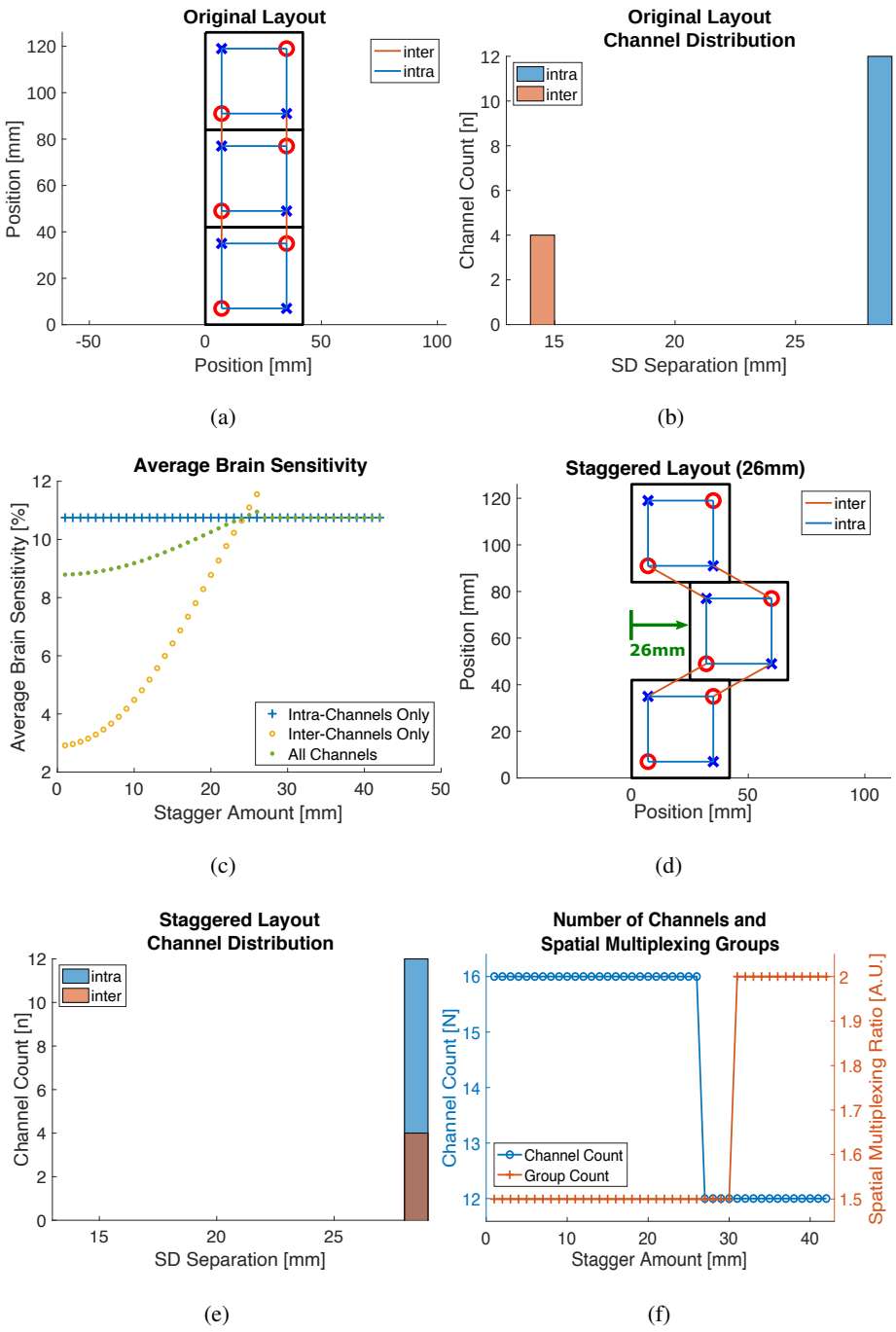

Figure 4.10: An analysis of square modules in a three-module probe. (a) A traditional three-module tessellation. Red circles represent sources and blue crosses represent detectors. (b) The resulting intra- and inter-module channel distribution from the probe layout in (a). (c) The average brain sensitivity for each layout resulting from module staggering. (d) The center module staggered by 26 mm, resulting in increased channel separation for inter-module channels, as shown in (e). (f) The total channel count and the number of spatial multiplexing groups of the probe layout as the center module is staggered.

4.5 Discussion

Through the case studies shown in the above section, we demonstrate the high complexity of designing a modular probe, where even adjusting a single parameter may have a profound impact on other parameters as well as the overall performance. Despite the fact that MOCA only permits operator-guided parameter interrogation in a well-constrained problem, the results from the above experiments did reveal a number of important design strategies that were not previously discussed in literature, including the effect of module re-orientation, fine-tuning the space between modules, and module staggering to potentially improve existing fNIRS probes.

Figure 4.5 reveals that, despite having the same optode layout, probes composed of different module shapes covering the same ROI result in different channel distributions. Although the inter-module channels are identical between modules, the resulting total number of channels is related to the number of modules needed to cover the ROI. The effect of module shape on channel distribution is complex and requires a tool like MOCA to thoroughly investigate. Certain module geometries result in optodes closer to the module's edges, effectively shortening inter-module channels in completely tessellated probes. Because the optode layout in Figure 4.4 is not completely symmetric and each module shape is an equilateral polygon, each individual module can be re-oriented without overlapping while maintaining the complete tessellation of the probe. While not altering intra-module channel distributions, these orientation configurations spatially alter channel locations and alter inter-module channel separations. The results from Figure 4.5 also show how some individual module shapes may be more appropriate for certain subject populations. For example, the high count of 19 mm inter-module channel separations in the hexagon-based probe makes it better suited for infant populations. An important takeaway is that the number of inter-module channels of an assembled probe is not a simple multiplicative factor of the number of intra-module channels. These results demonstrate the dependency a probe's derived characteristics have on module shape even when different modules have the exact same optode layout.

The results in Figure 4.6 provide a counter-example where higher channel density due to increased inter-module channels may not necessarily improve all performance metrics of a probe. Despite having fewer total channels than the hexagon-based probe, the square-based probe results in a higher average brain sensitivity ($\overline{S_{brain}}$) due to larger inter-module channel separations. This reveals the trade-offs in performance metric improvement, emphasizing the need for S_{brain} to be considered in conjunction with channel distribution when comparing probes. Additionally, this analysis reveals that the use of inter-module channels in addition to intra-module channels does

not always lead to increased S_{brain} for probes based on different module shapes. In fact, the use of only inter-module channels increases the average penetration depth for the square- and triangle-based probes due to the larger channel separations. However, for the hexagon-based probe design in this example, Figure 4.6 demonstrates that the contribution to $\overline{S_{brain}}$ from using only intra- or only inter-module channels differed by merely 0.1%. These results show that adding inter-module channels to intra-module probes will not always result in improved $\overline{S_{brain}}$. Thus, users of this particular hexagon-based probe may benefit from the simplicity and faster sampling rate of using only intra-module channels rather than implementing a potentially complex data acquisition method to capture inter-module channels. Although ignoring inter-module channels can increase the sampling rate without affecting S_{brain} for this particular probe, it does result in fewer channels and lowers the channel density of the probe. Through this complex example, we show that it is non-trivial to consider all constraints in a modular probe. MOCA is positioned as a tool to help designers challenge hypotheses, explore alternative designs, and quantify various trade-offs.

Figure 4.7 indicates that the hexagon-based probe can achieve the highest sampling rate among the three configurations if a spatial multiplexing encoding strategy is implemented. The frame rate of a sequential encoding strategy is dependent on the total number of sources (n_s) because each source needs to be turned on and sampled once. Spatial multiplexing allows multiple sources within a group to be turned on simultaneously, allowing the sampling rate to increase by a factor of n_s/n_{SMG}, defined as the SMR. Therefore, despite having the lowest sampling rate when sampled sequentially due to the highest n_s (Table 4.2, Row 1), the hexagon-based probe has the fastest sampling rate of the three probes when spatial multiplexing is used due to the low n_{SMG} [Figure 4.7(a)]. These results demonstrate that a probe's sampling rate can be increased not only through firmware changes or advanced electronics but also by using different module shapes with the same optode layout.

While MOCA's ability to change module-level parameters helps design new fNIRS modules, its ability to sweep through probe-level parameters helps potentially improve existing ones. Figure 4.8 shows how probes based on published modules can potentially improve $\overline{S_{brain}}$ at no increased cost and without re-designing modules by altering the orientations of modules that make up the probe. The orientation changes in layout 66 [Figure 4.8(c)] increase the channel density at the center of the ROI, but also increase the number of inter-module channels by 43%. The emerging inter-module channels also have larger SDS and contribute to an increase in $\overline{S_{brain}}$ without changing the SMR. The re-oriented probe in Figure 4.8(c) is only a representative case of how a 2×2 probe composed of square modules can be potentially improved and is exhaustive only because the

number of possible orientations of each of the 4 modules was limited to 4, resulting in $4^4 = 256$ probe layouts to analyze. Additionally, the re-orientation of modules causes changes to performance metrics due to the asymmetry of the optode layout within each module. If the optode layout was symmetric, re-orienting modules would have no effect on either inter- or intra-module channels.

In Figure 4.9, we investigated the effect of spacing between modules on the derived performance metrics of a probe composed of hexagonal-shaped modules. The results suggest that varying module spacing does have an impact on $\overline{S_{brain}}$. Since optodes are generally placed near the edges of the modules to maximize intra-module channel separations, dense probes with modules near one another tend to have shorter inter-module channel separations. This trend becomes more apparent as the size of the module increases. Increasing the probe spacing increases the distance between optodes on neighboring modules, thus increasing the $\overline{S_{brain}}$ in the process. This increase in $\overline{S_{brain}}$, however, has a local maximum. As shown in Figure 4.9, further increasing probe spacing leads to a drop in the number of inter-module channels as their SD separations become greater than the separation limit (SDS_{max}). Additionally, increasing the distance between modules reduces the number of multiplexing groups (n_{SMG}) which increases the SMR and consequently the probe's sampling rate. Once the probe spacing exceeds the user-specified SMG diameter, one source on each module can be turned on at the same time because each source would be outside the other's "effective" region. Because the distance between sources on the same module does not change, a different SMG is required for each source within a module. Thus, the limit to the minimum n_{SMG} is equal to the number of sources on a single module, revealing a minimum improvement in sampling rate due to spatial multiplexing encoding. Compared to a sequential sampling strategy, a spatial multiplexing encoding strategy will increase a probe's sampling rate by at least a factor equal to the number of sources on one module. Figure 4.9 shows that probe spacing can both alter n_{SMG} to help meet sampling rate requirements and alter inter-module channel separations to meet channel distribution needs.

Figure 4.10 shows that staggering a probe layout can increase $\overline{S_{brain}}$ in dense probes. Simulations using a published module shape [119] with zero probe spacing results in inter-module channels of 14 mm separations. These channels are too long to be SS channels and too short to be long-separation (LS) channels. Staggering spatially increases inter-module channel separations while maintaining the compactness of a probe [Figure 4.10(c)]. This improvement works with square or rectangular modules since staggering is done by translating user-specified modules along a horizontal or vertical axis. For module designs with symmetrical optode layouts, we recommend staggering probe layouts by translating every other module row by half of the module's maximum

width in one axis [Figure 4.10(f)]. This ensures the optodes from the translated module are well separated from modules of the adjacent rows.

The results above are derived from investigating the module- and probe-level design parameters that MOCA currently supports. However, this only represents a small subset of the general parameters previously used in evaluating a modular probe [114]. For example, user feedback-based design parameters not yet accounted for in MOCA include conformability (a module's ability to conform to a curved surface), subject comfort, and safety limits such as operating voltage and heating effects. Source output power and module weight each require external instrumentation measurements while noise-equivalent power and dynamic range calculations require lab-specific phantoms. Power consumption depends on the type of optodes used as well as the control electronics of the individual module while a probe's battery life can be adjusted using existing off-the-shelf components. Each of these design parameters are based on specific electronic or material components chosen for a particular module design. MOCA was built to easily scale and incorporate more complex mechanical-, ergonomic-, safety- and experiment-specific considerations in the future as those design parameters are evaluated.

There are limitations to MOCA's current minimal subset of design parameters. First, the ability to re-orient, increase spacing, or stagger modules assumes that modules can be connected in any orientation. This is true for many published modular designs where cables of different lengths can be easily connected to the top of a module, but does not necessarily apply to more sophisticated designs that have embedded printed flex connectors or utilize headgears with pre-determined mounting locations. Second, MOCA does not currently support multiple module shapes within the same probe or different optode layouts on different modules. Third, MOCA's channel count output does not include wavelength count as a multiplier. This approach allows one to quickly scale the channel distribution and channel counts when dual-wavelength or triple-wavelength sources are utilized. Similarly, the n_{SMG} is also defined for a single wavelength. Thus, when estimating the total sampling rate of the probe using multi-wavelength sources, the control unit must cycle through each group multiple times (once for each wavelength). Fourth, MOCA's analysis is based on the coordinates of the center of an optode's active area and does not account for the actual size of the optode package, the shape of the optode's active area, or any master control unit needed to control a series of modules. Despite being able to place optodes near the edge of modules in MOCA, designers may face constraints in practice imposed by the fabrication process due to board materials, sizes, and electrical routing needed to drive these optoelectronics. In general, module shapes with large interior angles allow optodes to be placed closer to the module's perimeter. Fifth, MOCA's

probe-level functions are but one method of interrogating parameters in a systematic way. These functions vary parameters in discrete increments (fixed number of orientations, a set spacing range, and user-defined translation amounts) and therefore only explore a subset of all potential probe layouts. They do not determine an optimal probe configuration—they assist in improving existing probes by adding design constraints (holding module-level parameters constant) and allowing a user to identify design choices that improve performance for their particular application. Finally, MOCA can output 2-D optode layouts but relies on other existing software, such as AtlasViewer [130], to perform 3-D head contour registration. It does, however, automatically add spring relationships to embed modular aspects into an exported probe. For example, the distance between all optodes (both sources and detectors) within a module is fixed, while inter-module channels can vary slightly. This ensures that a physically rigid electronic module does not transform when registered to a surface. In addition, the performance metrics output by MOCA are currently based on a 2-D probe layout and do not account for changes in SDS if the probe is "wrapped" on the 3-D surface of a head [123]. Consequently, 2-D-derived metrics may underestimate the number of channels when a probe is made to conform to the scalp. This may result in an increase in the number of total inter-module channels for a probe. However, by working in 2-D, MOCA can both help unearth design and performance relationships, as well as drastically constrain the vast potential design space by helping researchers converge on the module- and probe-level parameters that most impact performance.

In conclusion, the work in this chapter is an attempt to contribute to the adoption of NIR imaging systems by providing a software platform to systematically investigate the large design space of modularity. While the initial intent of using the modular architecture was to increase channel density in fNIRS probes, the emerging challenge of analyzing and comparing modular-based systems quickly resulted in a project in itself. This tool facilitates the design, adoption, and scalability of optical imaging systems by directly addressing the challenges of working with modular system attributes. As for other attributes, MOCA addresses portability since modular fNIRS systems are built out of lightweight modules that lend themselves to be easily transported. Additionally, by providing a spatial multiplexing strategy that can efficiently sample channels that leverage sources and detectors on neighboring modules, we have also provided the field with a method to increase channel density while still maintaining fast acquisition times. Without addressing the challenges of modular attributes using the capabilities that MOCA provides, we cannot expect the field to easily scale optical imaging systems into future applications efficiently.

CHAPTER 5

Modular Optical Brain Imager (MOBI)

This chapter is the second part of the work addressing the second challenge described in Chapter 1. While Chapter 4 focuses on describing the generalized software pipeline aimed at evaluating, comparing, and optimizing complex modular fNIRS systems, this chapter details our fiber-less, wearable, 3-D aware and modular MOBI system designed with guidance from MOCA. Portability is addressed through a lightweight, battery-operated system that can automatically detect how modules are connected to each other. By leveraging the connection topology and orientation sensors on each module, the MOBI system can internally determine the location of all optodes in a probe, drastically reducing setup times and making the systems easier to use in naturalistic settings. Here, we take portability a step further by creating a system made from flexible-circuit-based modules that conform to the scalp, allowing for long-term wearability in natural settings. Additionally, the high-density attribute is addressed through the implementation of a spatial multiplexing sampling strategy and through the use of inter-module channels, which are source-detector pairs with sources and detectors on neighboring modules.

5.1 Introduction

Neuroimaging techniques have advanced our fundamental understanding of human brain function [19]. However, brain activations often exhibit complex patterns and dynamics that are only apparent when measured in natural environments [20, 19]. Despite making tremendous progress, contemporary neuroimaging techniques such as fMRI [95] and MEG are hindered from studying these advanced dynamics due to their poor portability and immobility during use [21, 22]. Electroencephalogram (EEG), although highly portable, suffers from low spatial resolution com-

pared to fMRI [153, 21]. These inherent disadvantages of the gold standard techniques restrict our current understanding to limited types of stimuli and interactions within confined spaces [20]. In recent years, researchers have turned to fNIRS to address this technological gap [60]. FNIRS is based on the theory of neurovascular coupling [61]. It uses low-power light spectroscopy to measure brain activation and its associated hemodynamics [60]. With its non-invasive nature, the use of fNIRS has increased exponentially [109, 22] to include studies from psychiatric conditions [103, 104] and language [101, 102, 154] to cognitive neurodevelopment [97, 98, 99, 100] and stroke recovery [105], education [155], pain detection [156], and even brain-computer interfaces [106, 107, 108].

Many of these studies using fNIRS have utilized traditional, fiber-based, cart-sized instrumentation [62, 110, 111, 157]. Despite it being an improvement over conventional fMRI and MEG modalities, fiber-based fNIRS systems also quickly reached a limit on portability and channel density due to the use of fragile fiber optic cables [158, 122] and stationary source/detector units [112, 113]. The need to expand toward broader paradigms in unrestricted environments [19] requires the use of portable and wearable systems [115, 20], and the need for wearable systems has led to the increased use of modular architectures [119, 120, 121, 132, 23, 24, 25].

As detailed in Chapter 4, modular fNIRS systems are probes composed of repeating source/detector circuits called modules. Repeating modules not only facilitate and lower fabrication costs but also allow for re-configurability to varying sizes of regions of interest [114]. By using only the minimal number of modules needed for a specific task, modular fNIRS systems drastically improve portability [22]. Additionally, the use of varying SD separations by utilizing both intra- and inter-module (sources and detectors on different modules) pairs provide overlapping channels, improving both spatial resolution and depth specificity (a key parameter in removing systemic physiological signals) [116, 24]. Modern fNIRS systems now leverage a plethora of state-of-the-art design and analysis tools that support the use of modular architecture in natural environments. Optode layout optimizers [128, 130, 129, 127] and modular probe designers [30] ensure application-specific arrangements, motion [124, 125] and coupling [126] artifact correction algorithms allow for improvements in data quality, and faster light-propagation simulation tools [137, 136] facilitate the use and analysis of high-density fNIRS probes.

Despite its increasing adoption, the modular high-density fNIRS architecture also possesses its own set of technical challenges [159, 21] and usability concerns [160, 161]. First, the use of fNIRS in natural settings means subjects will be more mobile, leading to headgear moving and shifting relative to the scalp during use [21, 162]. Current solutions to ensure proper coupling use mechanical components that are cumbersome, require replacements, and add head-borne

weight [163, 119]. Second, the ever-increasing number of optodes in a probe requires very efficient encoding strategies to maintain sufficiently high frame rates to capture the hemodynamic response function (HRF) [117, 157, 164]. Finally, in order to improve accuracy using high-density tomographic analysis, we must be able to know the location of all optodes in a probe prior to and during the use of a system [165]. The most traditional approach is to use expensive hand-held 3-D digitizing systems to record the coordinates of optodes prior to the start of an experiment [159, 23]. More recent solutions leveraging photogrammetry promise to be more portable, but still require a set of external cameras that restrict mobility to areas within the camera's field of view [24, 165].

To address these needs, we have designed a lightweight and re-configurable fNIRS Modular Optical Brain Imager (MOBI) system well-suited for full-head long-term brain monitoring or over a particular ROI. This ultra-compact and fiber-less system addresses optode-to-scalp contact coupling through its shape and board composition. A dual-triangle shape allows for better conforming to a surface, akin to how a triangular mesh accurately represents a 3-D shape, while its flexible-circuit-based board allows the entire module to bend over arbitrary shapes to ensure constant optode-to-scalp contact [163, 133]. Additionally, a dense peer-to-peer (P2P) network allows the system to automatically determine the connection topology between modules of a probe without user input. This facilitates the implementation of a spatial multiplexing encoding strategy to increase a probe's full frame rate. Finally, the wearable MOBI modules each contain 3-D orientation sensors that leverage the connection topology and the module's geometry to automatically determine the location of all sources and detectors without the use of an external hand-held or photogrammetry tracking system. This automatic, independent digitization method shortens setup times, ensures high data quality, and improves accuracy and contrast through tomographic reconstructions.

In this chapter, we introduce our MOBI system. In Section 5.2, we describe our MOBI system design, including details of individual modules as well as supporting components such as the master and trigger boards. We also highlight novel features of our system, including connection topology recognition, inertial measurement unit (IMU)-based optode positioning, and frame rate improvement through spatial multiplexing. Section 5.3 focuses on the characterization of our MOBI module and the validation of its features. We quantify conformability through the use of flexible-circuit-based modules and detail the accuracy of our internal-based optode digitization method. Additionally, we show results from two *in-vivo* experiments and compare MOBI's performance to that of a commercial fNIRS system. Finally, Section 5.4 describes the limitations and assumptions used in our investigation and proposes work to address them in the future.

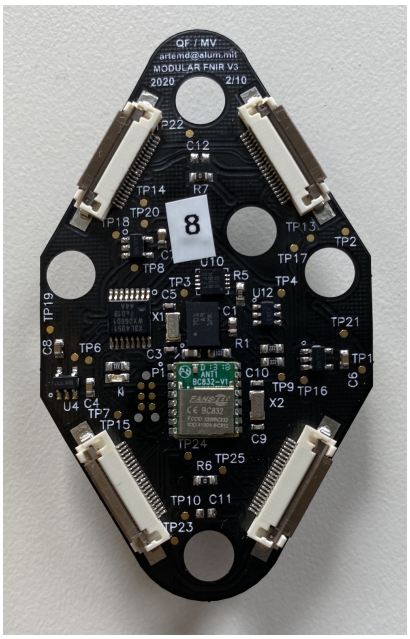

(a)

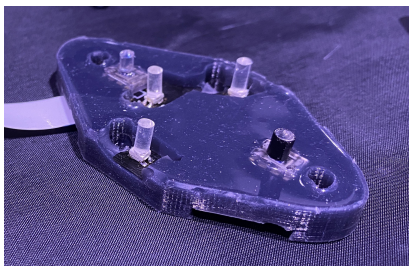

(b)

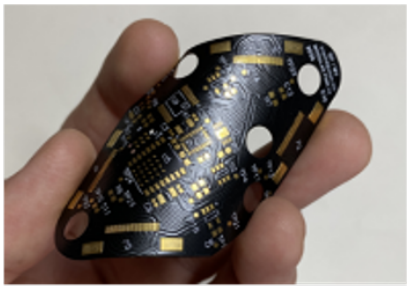

(c)

Figure 5.1: (a) Top side of a Modular Optical Brain Imager (MOBI) module without a silicone cover showing the four flexible printed circuit connectors and 5 hair-acccess holes. (b) Bottom side of a MOBI module with light guides on optodes and black silicone cover of board. (c) Unpopulated flexible-circuit board for a MOBI module.

5.2 Methods

5.2.1 Module design

Our MOBI system is based on double-sided modules manufactured on flexible-circuit-based boards, allowing the modules to bend and conform to the scalp [Figure 5.1(c)]. Each module houses two detectors (OPT101, Texas Instruments, USA) with built-in trans-impedance amplifiers. The 3 dual-wavelength sources (SMT735D/850D, Marubeni, Japan) at 735 and 850 nm are driven from a digital multiplexer (NX3L4051, NXP Semiconductors, Netherlands) with a programmable constant current driver (LT3092, Analog Devices Inc., USA) using a spatial multiplexing encoding strategy (Figure 5.2).

The optode layout results in one 8 mm, one 30 mm, and four 24.5 mm dual-wavelength channels on a single module. A 3 mm diameter light guide (53-833, Edmund Optics, USA) is glued to each optode to focus the emitted and detected light [Figure 5.1(b)]. A 9-axis IMU allows for absolute orientation measurements for each module (BNO055, Bosch Sensortec, Germany). All optodes

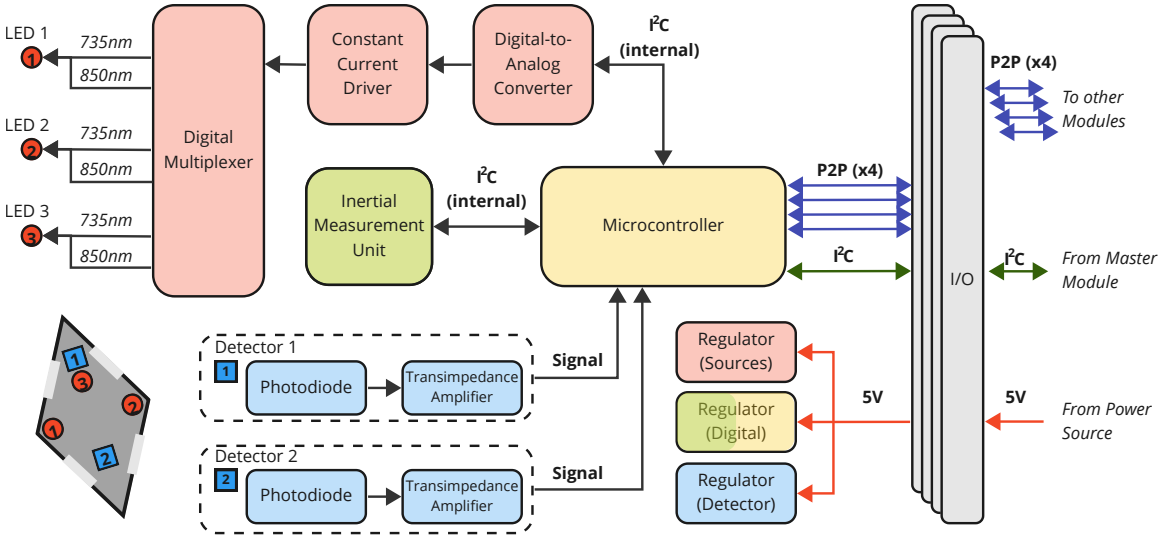

Figure 5.2: Schematic diagram of a single Modular Optical Brain Imager module. The microcontroller uses an internal inter-integrated circuit (I^2C) protocol to communicate with components on a single board. A peer-to-peer (P2P) network allows communication between neighboring modules.

and sensors on the MOBI module are controlled and read by an onboard system-on-a-chip (BC832, Fanstel Corp, USA) with an integrated microcontroller (nRF52832, Nordic Semiconductor, Norway). An internal inter-integrated circuit (I^2C) communication protocol is used to set the current driver and communicate with the onboard IMU (Figure 5.2). Additionally, three low-dropout voltage regulators regulate the power source voltage for the source, detector, and auxiliary measurement components. The microcontroller samples all six dual-wavelength channels, dark measurements, and IMU measurements at a frame rate of 22 Hz.

The five optodes are located on one side of the module—the side that remains in contact with the scalp. All driving electronics are placed on the non-scalp side of the module to assist with heat dissipation and comfort. Triangles are the most efficient shape for tessellating a 3-D surface, thus, the use of a "dual-triangle" shape (two equilateral triangles with 50 mm sides) and a flexible-circuit-based board allows for increased conformity and optode-scalp coupling. MOBI modules have a channel density of 0.56 dual-wavelength channels per square centimeter. The modules are completely encapsulated in flexible black silicone to provide comfort during long-term wear, block stray light, and protect the electronic components during use. Each module has four flexible printed circuit (FPC) connectors that allow multiple modules to be connected using FPC cables of fixed lengths [Figure 5.1(a)]. A P2P serial network allows each module to communicate with up to four

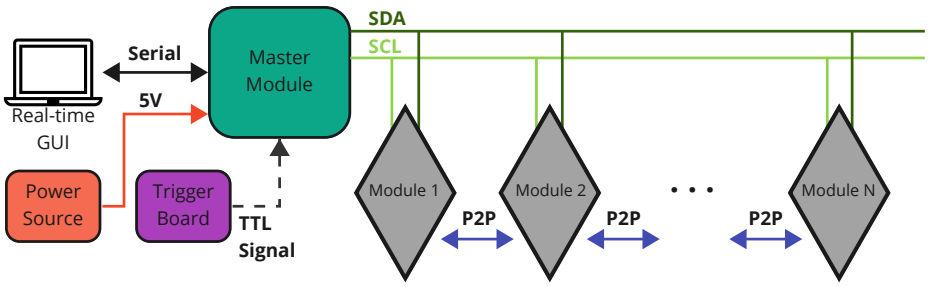

(a)

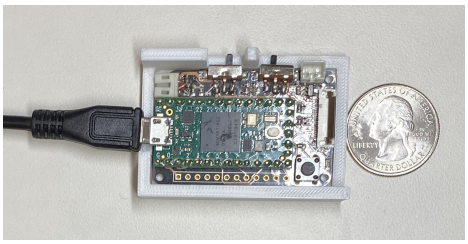

(b)

Figure 5.3: (a) Schematic diagram of a Modular Optical Brain Imager system. An external power source and trigger board are optional. (b) The master module without its cover.

connected neighboring modules. Five 6 mm diameter holes next to each optode are used for hair removal after placement on the scalp. Each module, including the components, light guides, and silicone cover, weighs 14 grams.

5.2.2 System architecture

Our MOBI system consists of a computer, a single master module, and an arbitrary number of MOBI modules connected to each other using FPC cables (Figure 5.3). Optionally, a separate power source and a trigger board can also be connected to the master module to allow synchronization of events during experiments. The master module uses an I^2C communication protocol for power and data acquisition of each module (Figure 5.3(a)). The master module incorporates a USB-based microcontroller development system (Teensy 4.0, PJRC, USA), a voltage regulator, an FPC connector, a Japan Solderless Terminal (JST) connector, and two switches. A micro-USB cable connects the master board to a computer for serial communication. The switches are used to manually select the power source (from micro-USB or an external battery). A 2-pin JST connector allows an external trigger board to be connected for synchronizing auxiliary signals such as exper-

(a)

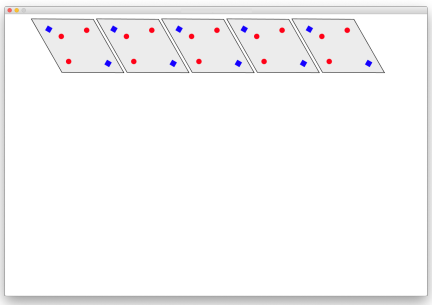

(b)

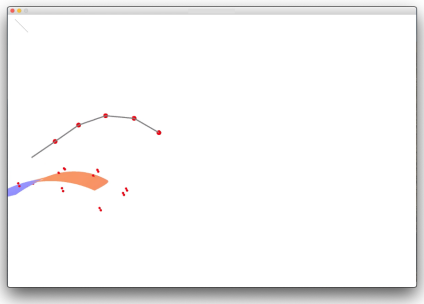

(c)

Figure 5.4: (a) Five modules in a single chain configuration connected to a master module. (b) Modular Optical Brain Imager (MOBI) Graphical User Interface (GUI) displays 5 modules connected. (c) MOBI GUI displays the relative position of each module based on differences in neighboring orientation measurements.

imental triggers. The trigger board is based on a simple microcontroller (Atmega328p, Microchip, USA) and interrupts fNIRS readings from inputted transistor-transistor logic (TTL) signals. The entire trigger board is encased inside a 3-D printer cover. A GUI provides real-time detector and IMU readings. The GUI also provides the ability to change the current source and detector gain of individual optodes. All acquired MOBI data is saved in Shared Near Infrared Spectroscopy Format (SNIRF) [166].

5.2.3 Automatic features

Here, we describe MOBI's automatic features, including connection topology recognition, IMU-based optode positioning, and spatial multiplexing encoding. These complex features are best visualized in our MOBI demo video [167].

5.2.3.1 Connection topology recognition

Our MOBI system has the ability to recognize the connection topology between all modules to determine the number of modules and the orientation of each module in an arbitrary probe. Any two modules can be connected by simply bridging any FPC connections with an FPC cable [Figure 5.4(a)]. Upon start-up, each module samples all four of its P2P communication channels to determine if another module is connected to one or more of its FPC connectors. This sampling of inputs/outputs allows the P2P serial network to automatically determine how each module is laid out relative to others. With the P2P connections identified, the master board can determine the orientation of each module in the probe by simply rotating and translating the module dimensions based on the connection topology [Figure 5.4(b)].

5.2.3.2 IMU-based optode positioning

Additionally, our MOBI system can automatically determine the 3-D position of each source and detector in the probe without the use of an external digitizer. With the connection topology known, the master module can sample the orientation sensors between neighboring modules to create a 3-D spline estimating the shape onto which the probe is placed [Figure 5.4(c)]. The master module then superimposes FPC cable lengths, module geometry, and optode layout within a module to derive the 3-D location of each optode, reducing the need for time-consuming 3-D position measurements. The IMU measurements also permit robust temporal signal rejection through real-time monitoring of optode movements during use.

5.2.3.3 Spatial multiplexing groupings

Finally, our MOBI modules utilize a spatial multiplexing encoding strategy in which sources are grouped into SMG and turned on at the same time [30]. Based on the layout of all the sources and detectors (automatically derived from the connection topology), the master module assigns sources into SMGs to be on simultaneously without cross-talk based on the SNR of the system. In this way, probe layouts that are more spread apart lead to a smaller number of SMGs because the sources are more dispersed. The SMR is defined as the number of sources in a probe divided by the number of SMGs. In this way, spatial multiplexing improves a system's full frame rate by a factor of SMR.

5.2.4 *In-vivo* protocols

The MOBI system was validated against a commercial fiber-based fNIRS system (Brite23, Artinis) through simultaneous measurements during a dual-pressure cuff occlusion experiment on the arm. A single MOBI module and an Artinis probe with a single channel were placed on the underside of the forearm for the cuff occlusion experiment. The upper arm rested at the same height as the heart. Data from the 30 mm channels were simultaneously captured at 10 Hz in a completely dark room. The 100 mmHg (venous) and 220 mmHg (arterial) occlusions lasted 75 seconds each.

Additionally, human brain activity was measured in an adult male in the left motor cortex area during a finger-tapping task. The finger-tapping task consisted of a 10-second task period followed by 20 seconds of rest, repeated 10 times with 60 seconds of baseline rest prior to and at the end of the repeated tasks. Subjects were instructed to sit still with their eyes closed during the entire experiment. During the task period, a verbal command instructed the subjects to tap their right thumb sequentially against their index, middle, ring, and pinky finger, followed by the same sequence mirrored, repeated as fast as possible until instructed to rest. During rest, subjects were instructed to place both hands on their laps. Signals were obtained through a single MOBI module placed over the left motor cortex.

Data from MOBI were converted to SNIRF format using MOCA. Data from Artinis was first converted to the NIRS format using the Artinis software, OxySoft, prior to converting to SNIRF format using HomER [124]. Optical density was converted to hemoglobin concentrations using HomER after applying a 0.01 Hz high-pass and a 0.5 Hz low-pass filter to all channels.

5.3 Results

5.3.1 System characterization

A 20-module full-head MOBI probe results in 372 dual-wavelength channels due to the use of source and detector pairs in between adjacent modules. This increases the achievable channel density to 1.72 channels per square centimeter. Additionally, with MOBI's spatial multiplexing encoding strategy and a SD separation cutoff of 52 mm (where SNR is $>$ 40 dB), this full-head probe results in 14 spatial multiplexing groups and a full frame rate of 4.7 Hz. Each source is driven at 100 mA. The total power draw of the full-head probe is 2.31 W, resulting in a 2.85-hour battery life when a 3.7 V 2000 milliamp-hour (mAh) battery is used.

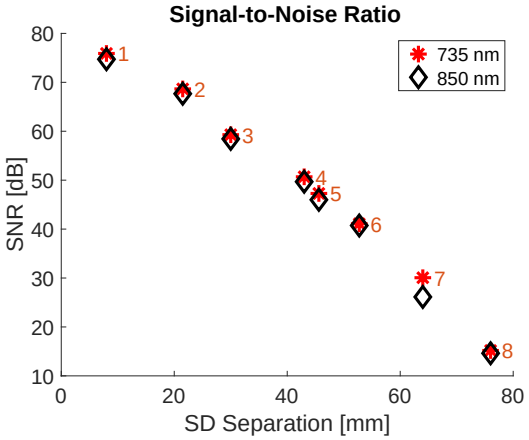

Figure 5.5: Signal-to-noise (SNR) of MOBI modules as source-detector separation increases. Red asterisks indicate SNR for the 735 nm while black diamonds are for the 850 nm wavelength. Orange numbers signify the channel number. Channels 1, 2, and 3 are from sources and detectors on the same module. The large source-detector separations of channels 4-8 are from sources and detectors on different modules.

Table 5.1: The full frame rate of a probe depends on the layout of the modules within a probe. The three layouts in Figure 5.6 result in the channels, groupings, and full frame rates below.

	Layout 1	Layout 2	Layout 3
Number of Modules	5	5	5
Temporal Encoding Full Frame Rate [Hz]	4.4	4.4	4.4
Number of Channels	38	53	55
Number of Spatial Multiplexing Groups	6	7	8
Improvement Ratio (SMR)	2.5	2.14	1.875
Spatial Encoding Full Frame Rate [Hz]	11	9.4	8.25

Figure 5.5 shows the SNR as a function of SD separations. The SD separations were calculated from intra- and inter-module channels using a 3-module probe placed on an optical phantom ($\mu_s^{'} = 4.7\ cm^{-1}$ and $\mu_a = 0.063\ cm^{-1}$ at 830 nm). Each measurement is the average of 10 samples of that channel. Figure 5.5 shows a linearly decreasing SNR as SD separation increases for both wavelengths. The correlation coefficient, R^2, is 0.955 and 0.959 for the 735 and 850 nm wavelengths, respectively. SNR for MOBI modules is greater than 50 dB for SD separations of up to 43 mm.

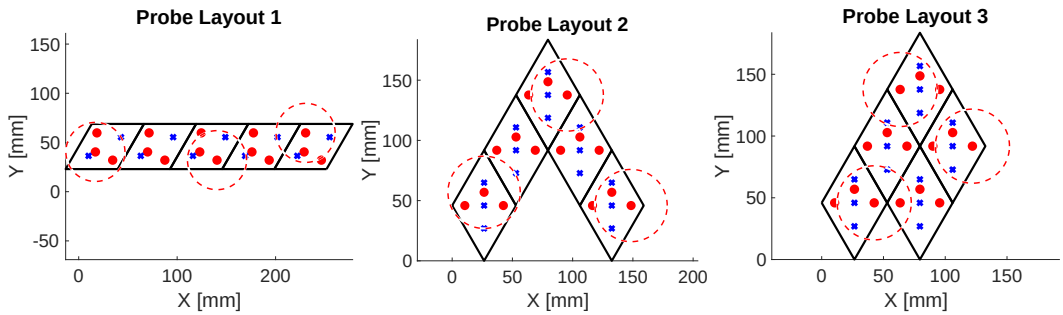

(a) (b) (c)

Figure 5.6: Three example probe layouts all composed from five identical Modular Optical Brain Imager modules. Optodes are represented by small red circles (sources) and blue crosses (detectors). Each layout has multiple spatial multiplexing groups determined based on the global proximity of sources to each other. Red dashed circles show which sources are simultaneously on for the first spatial multiplexing group of each layout.

5.3.2 Spatial multiplexing improvement

The performance results from three different 5-module probe layouts (Figure 5.6) are shown in Table 5.1. When using a temporal encoding strategy, the full frame rate of the probe is determined by the number of sources in the probe since each source is sampled sequentially. Although the temporal encoding full frame rate remains constant at 4.4 Hz, the channel density and the number of spatial multiplexing groups increase from layout 1 to 3 as the layout of the probe becomes denser (Row 3, Table 5.1). Consequently, SMR decreases as the probe layout increases in density, limiting the potential full frame rate performance gain. Layout 1 saw the biggest improvements in full frame rate when converting from a temporal to a spatial encoding strategy. The spatial multiplexing full frame rate was always larger than the temporal encoding full frame rate for all three layouts.

5.3.3 Optode-scalp coupling

A 5-module probe, in a configuration identical to layout 2 in Figure 5.6(b), was placed on a 100 mm radius sphere. The flexible-circuit-based modules were connected using FPC cables using the FPC connectors. The rigid boards were connected using FPC cables glued onto rigid extrusions that represented where the FPC connectors would have been soldered. The component layout between the flexible and rigid boards is identical. The 25 optodes were digitized using a

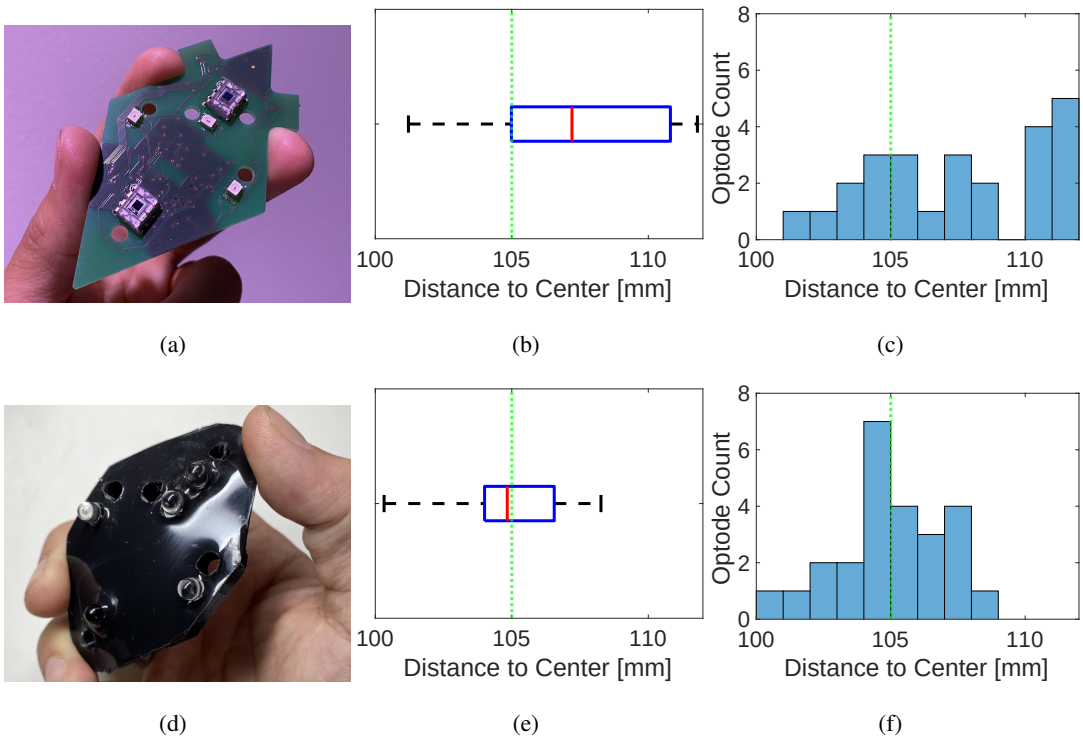

(a) (b) (c)

(d) (e) (f)

Figure 5.7: (a) A rigid-based board showing three sources and two detectors. (b) Boxplot showing the distance from optode locations to the center of the sphere using rigid modules. The red line denotes the average distance of all 25 optodes. The dashed green line represents the expected distance to the center given the 5 mm thickness of the modules. (c) A histogram of the distances reveals that the rigid-based probe does not conform to the sphere, leading to optodes being farther away from the surface, especially those optodes closer to the edge of the module. (d) A flexible-circuit-based board showing three sources and two detectors with light guides. (e) Boxplot showing the distance from the optodes to the center of the sphere of the flexible-circuit-based probe. (f) The histogram of the flexible-circuit-based probe optode distances.

hand-held Polhemus digitizer and the distance to the center of the sphere was calculated for each optode in both probes (Figure 5.7). The digitization was conducted on both flexible-circuit-based and rigid-based modules [Figs. 5.7(a) and 5.7(d)].

Figure 5.7(b) shows the average distance to the center of the sphere for all optodes of a rigid-board-based probe to be 107.5 mm with a range of 10.5 mm. In contrast, the average distance to the center decreases to 104.9 mm with flexible-circuit-based boards that allow the module to conform to the spherical surface [Figure 5.7(e)]. Additionally, the range of distances decreases when using flexible-circuit-based modules. Figure 5.7(c) reveals a skewed left histogram, indicating that optodes near the edges of rigid modules remain farther from the scalp. Figure 5.7(f), however, shows that by using flexible-circuit-based modules, the same optode layout within a module results in optode distance closer to the scalp, indicating the ability of flexible-circuit-based modules to conform to the surface.

5.3.4 Automatic optode positioning

Figure 5.8(b) shows the traditional hand-held-based optode locations against the resulting optode locations using internal orientation sensors. For visibility, the optode locations are displayed over a 100 mm radius sphere. The cyan circles are optode locations averaged across five repetitions of hand-held digitizations. The standard deviation across those five hand-held digitizations was 1.78 mm. Figure 5.8(c) shows the average digitization error over all optodes, defined as the Euclidian distance between the orientation-sensor-based location and the hand-held-based location. The average orientation-based error was 1.4 mm. Figure 5.8(d) shows the same digitization error with optodes grouped by module. For all five modules, the average digitization error was less than 2 mm.

5.3.5 Cuff occlusion results

Figure 5.9 shows the resulting changes in hemoglobin concentrations during the dual-pressure blood cuff occlusion experiment. During venous occlusion, both HbO and HbR increase for both systems [Figs. 5.9(a) and 5.9(b)]. The arterial occlusion resulted in a negative correlation between HbO and HbR, as demonstrated by the horizontal total hemoglobin (HbT) line. Additionally, the MOBI module captured the hyperemic peak typically observed when occlusion is suddenly released.

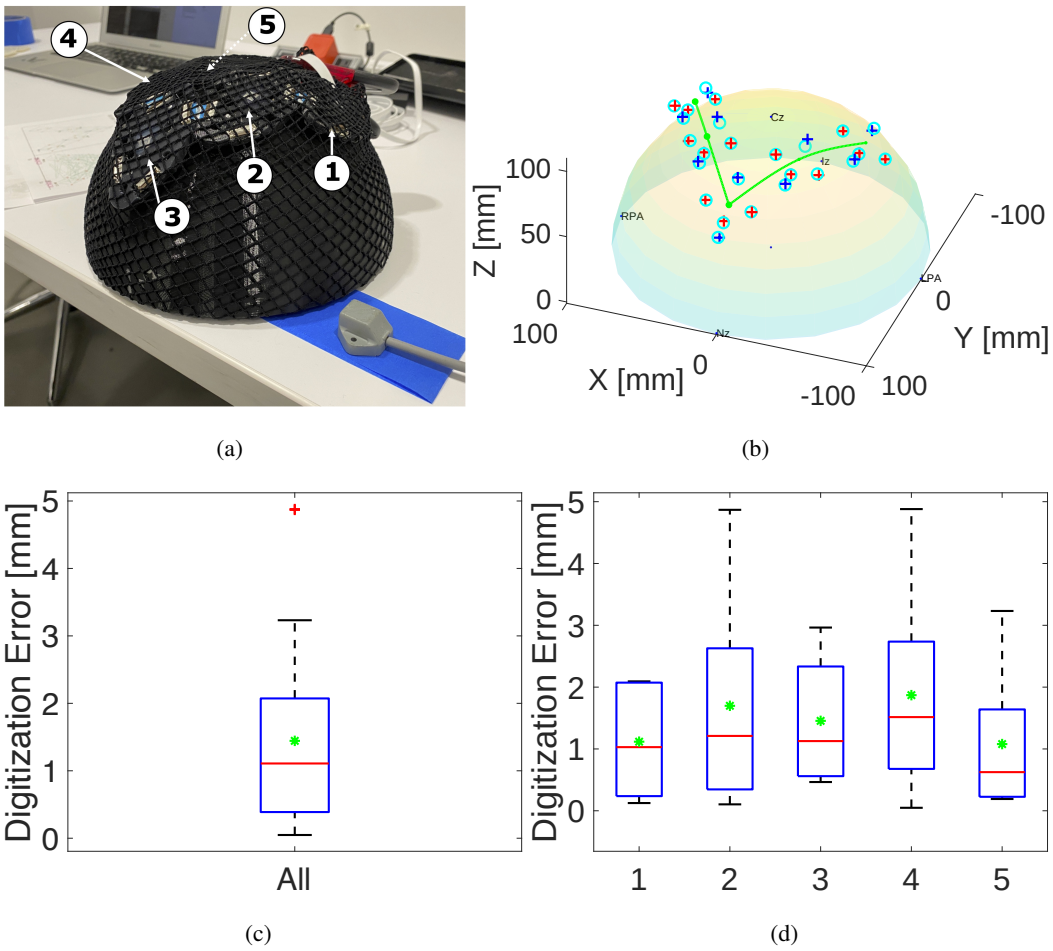

Figure 5.8: (a) Flexible-circuit-based Modular Optical Brain Imager (MOBI) modules arranged in probe layout 2 (from Figure 5.6) on top of a 100 mm radius sphere. (b) Spline model between 5 MOBI modules (green line) from which source (red crosses) and detector (blue crosses) positions are derived. Automatic optode digitization overlaid on manual digitization results (cyan circles). (c) Digitization error distribution averaged over all five modules in the probe. A green asterisk indicates the average digitization error. (d) Digitization errors are grouped by module.

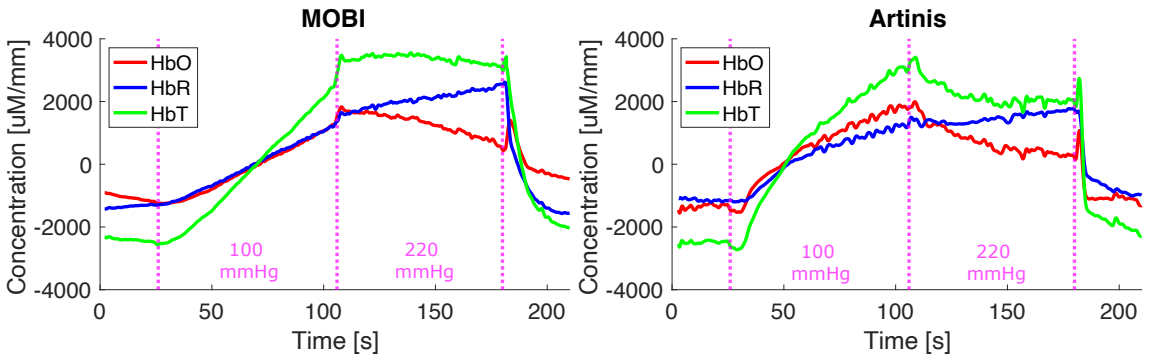

(a) (b)

Figure 5.9: Results from a dual-pressure blood occlusion experiment using (a) a single Modular Optical Brain Imager module and (b) a single Artinis channel placed on the forearm. Venous (100 mmHg) and arterial (220 mmHg) occlusions lasted 75 seconds each prior to release. Oxygenated, deoxygenated, and total hemoglobin concentrations are shows in red, blue, and green lines, respectively.

5.3.6 Finger-tapping results

Figure 5.10 shows the resulting HRF after block-averaging during a finger-tapping experiment. The stimulus lasted 10 seconds with a 20-second break in between, repeated 10 times. A clear hemodynamic response is shown with an increase in HbO of 60 μM approximately 10 seconds after stimulus onset. All channels demonstrated the expected increase in HbO and decrease in HbR, albeit channels over the motor cortex show a larger amplitude response.

5.4 Discussion

While many modular fNIRS systems have brought about advantages such as portability, scalability, and modularity, to our knowledge this is the first 3-D aware and fully flexible-circuit-based system. MOBI's features are especially important for transitioning fNIRS from laboratory/clinical settings to natural environments. With the expected higher physical movements in these new settings, we must find new and simpler methods to ensure optode-to-scalp coupling during use. Additionally, for true wearable commercial adoption, the fNIRS community needs to rely less on expensive and cumbersome technology, such as 3-D tracking systems, for system setup. MOBI's automatic connection topology detection and IMU-based optode positioning do just that—they provide the necessary technical quantification for highly accurate 3-D modeling without the need for

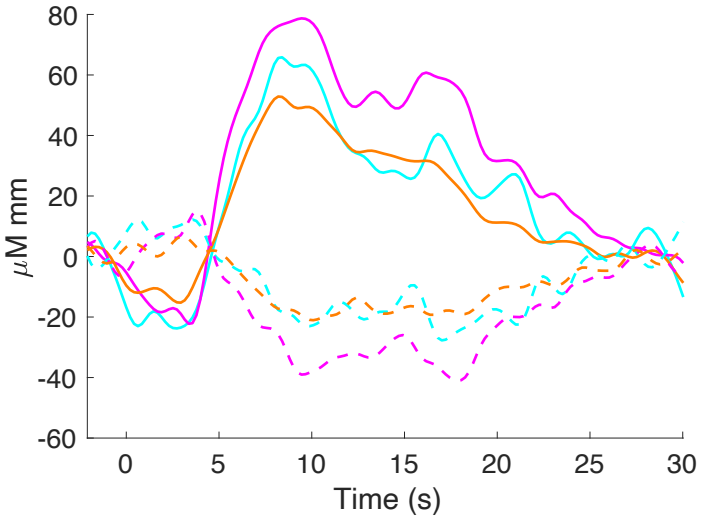

Figure 5.10: Block average results from a finger-tapping experiment with a Modular Optical Brain Imager module placed over the left motor cortex centered on the "C3" landmark defined in the standard 10-20 system. Solid lines are oxygenated and dashed lines are deoxygenated hemoglobin. Magenta, cyan, and orange lines represent different channels within the probe.

lots of user input and knowledge, enabling not only a wearable system but a usable one too.

Additionally, the system's usability is improved without affecting its performance. Figure 5.5 shows MOBI's large dynamic range, an important consideration for modular, full-head systems with multiple channels of various SD separations. A high SNR is achieved for large SD separation while keeping safety considerations in mind. For example, the holes designed into the modules used for clearing hair also provide cooling. The double-sided board design places only optodes on the scalp-facing side, limiting all driving electronics to the non-contact side, allowing for further heat dissipation for long-term wear. With a measured 9.8 mΩ resistance for each module, 75 modules can be theoretically connected prior to the 5 V supply power dropping below the necessary 3.3 V to drive the microcontrollers, far above the approximate 20 modules needed for a full head probe. Excluding the master board and any fabric to further block light, a full-head 20-module probe would weigh 280 grams (about the weight of an average bicycle helmet)—lightweight enough for long-term wear.

Full-head modular probes not only require lightweight modules and large dynamic ranges but also an encoding strategy to ensure fast full frame rates. Figure 5.6 shows how a spatial multiplexing encoding strategy can improve a full probe's sampling rate by leveraging a probe's layout rather than the total number of sources. As long as sources are spatially dispersed based on their

performance, contributions to a detector's readings avoid cross-talk. As the probes become denser and the number of channels increases (Table 5.1, Row 3), the distance between sources decreases, and the number of SMGs must increase to prevent cross-talk. Similarly, as 2-D probes are placed on 3-D surfaces, the Euclidean distance between sources decreases, which may require further SMG refinement. Although spatial multiplexing can be easily implemented and doesn't require extensive hardware, it does require knowledge of the location of all sources and detectors to identify the SMGs for a particular probe—a functionality that many systems currently do not possess without the use of external digitization tools.

In addition to increasing the full frame rate of a probe, modular fNIRS systems must ensure proper source-to-scalp coupling during high-movement use in natural settings. Figure 5.7 compares a rigid board and a flexible-circuit-based board's ability to conform to a surface. Rigid modules have minimal direct contact with the scalp and rely on mechanical/protruding couplers on the optodes or curved board designs tailored toward specific head shapes. Figure 5.7 highlights the source-to-scalp gaps inherent in rigid-board designs. Therefore, designers of rigid boards must balance between designing smaller boards to increase source-scalp coupling or designing larger boards that allow for larger SD separations. Our flexible-circuit-based boards allow for both.

Finally, not only is source-to-scalp coupling important, but an fNIRS system must also constantly measure the position of each optode during use. Figure 5.8 validates the accuracy of our internal IMU-based optode positioning system. It demonstrates that the average error between MOBI's IMU-based optode digitization and the traditional Polhemus-based digitization is only 1.4 mm. The positioning error is less than the variability of repeated handheld-based digitization systems. This method requires knowledge of the probes connection topology, assumes fixed FPC cable lengths, and requires knowledge of the module geometry and optode layout. Although automatic optode digitization can drastically reduce the time it takes to set up fNIRS systems, it does require appropriate hardware support such as a P2P network and orientation sensors on each module. Although we have seen the use of orientation sensors in modular systems for motion artifact correction, to our knowledge, this is the first use of IMUs for internal-based optode positioning and decreasing system setup times.

Figure 5.9 shows the results of validating our MOBI system against a commercial fNIRS system. As expected, both systems show an increase in both HbO and HbR during venous occlusion. When the pressure increases above systolic pressure, we see a negative correlation between HbO and HbR due to the muscles depleting blood oxygen during the occlusion of arterial blood. Finally, the hyperemia peak seen at 180 seconds corresponds to the increase in blood flow that occurs following

arterial occlusion. Not only do both systems capture the same physiological traces, but the traces are consistent with previous research results [25]. Similarly, Figure 5.10 shows the results of a finger-tapping experiment. As expected, the HRF shows an increase in HbO and a decrease in HbR during a task that utilizes the motor cortex. Although we cannot say anything about our system's performance across a population due to it being a study of N=1, these experiments demonstrate that MOBI's ability to extract tissue hemodynamics and brain activity is comparable to existing commercial systems.

Our MOBI system has limitations despite directly addressing many usability concerns of wearable systems. First, spline models onto which optode layouts are superimposed rely on the assumption that the distance between modules is fixed. In MOBI, we use 14 mm length non-stretchable FPC cables that provide a 2 mm gap between modules once connected to the FPC connector. As MOBI samples neighboring IMUs, it fixes the spline distance between modules. Depending on the cap design, this assumption may not hold true for other fNIRS systems (for example, if modules are placed on stretchable fabric). Second, while connecting modules using FPC cables assists with determining the connection topology, it makes it difficult to remove a single module from a dense probe to adjust hair under a particular region. Rather, our MOBI system uses two caps—a sparse mesh cap that holds the probe in place while a user uses the holes to access and adjust hair under optodes, and a second cap placed after hair adjustment to further block stray light. Third, the finger-tapping results were conducted on a subject with short hair. Further investigations into the effect of hair artifacts on signal quality must be performed. Finally, although MOBI data can be saved in the standardized SNIRF format, our data acquisition Processing-based GUI requires users to learn and work in a new interface. Future work includes integrating our work with the open-source middleware Lab Streaming Layer [168] for easier synchronization and recording of fNIRS and auxiliary data.

While many portable, modular, and high-density fNIRS systems have been recently published, in this chapter, we further explored methods to improve on these architectural attributes. The use of lightweight and low-power modules allows the system to be easily carried and powered through a portable battery. We also leverage flexible-circuit boards to allow for conforming to the scalp, which improves optode-scalp coupling by providing comfort for long-term use, making MOBI not just portable but wearable too. The modular-based architecture allows MOBI to be used for full-head studies or over a particular region of interest. When used with MOCA, a user can compare our MOBI system with other existing modular systems, a capability that was not previously available to the community. Finally, we explored the high-density attribute in two ways. First, the

use of IMUs along with an automatic connection topology allows for the location of all sources and detectors to be known during use, allowing for 3-D tomographic reconstructions of brain activations using a high number of channels. Additionally, we support this increase in channel density by introducing a spatial multiplexing encoding strategy to accelerate acquisition times.

CHAPTER 6

Optical Mammography Co-Imager (OMCI)

OMCI is a wide-field diffuse optical tomography breast imaging system designed to be used in conjunction with existing x-ray mammography systems or as a standalone system for DOT. It is assembled on top of a mobile cart, allowing it to be wheeled throughout a clinic. Portability is also addressed through the SLI subsystem, which can be removed and re-attached without the need for re-calibration. In terms of modularity, it integrates four subsystems: a mechanical breast compression stage to resemble clinical mammography, a frequency-domain subsystem for recovering absolute tissue optical properties, a wide-field transmission-based diffuse optical subsystem, and a high-resolution breast surface acquisition system. Although not all identical, each subsystem can be toggled on/off, allowing for OMCI to use only the minimal number of subsystems required for its application. A wide-field illumination and camera-based detection system allow for high-density and high-resolution imaging of large breast tissue volumes, improving acquisition speeds compared to fiber-based systems. This assembly method of building high-density and portable DOI systems promotes scalability through the use of a generic USB communication interface that allows for the simple expansion of future subsystems and/or the ability to upgrade specific subsystem components without affecting the whole. Although OMCI is composed of four separate subsystems working in tandem, in this chapter, we will briefly provide an overall instrument description but will focus on the design and characterization of the dual-camera SLI breast shape acquisition system used for improving diffuse optical tomography image reconstructions.

6.1 Introduction

Breast cancer is the most commonly diagnosed cancer in women worldwide with an estimated 1,918,030 new cases in 2022 in the United States alone [169]. Screening and diagnostics of breast cancer are done through structural or functional breast imaging using multiple breast imaging modalities. X-ray mammography and DBT are the primary breast cancer screening techniques [3] used for early detection to reduce mortality rates [170]. Modalities such as magnetic resonance imaging (MRI) and positron emission tomography (PET) are used less frequently than x-ray due to their high cost and use of radioactive isotopes [3]. Despite its recommendation for screening, not only does x-ray mammography expose patients to ionizing radiation but it also suffers from a high false-positive diagnostic rate [170, 171]. The modality lacks both strong structural contrast between healthy and tumor tissue, and the ability to quantify tissue functions to assess benign versus malignancy [172]. These limitations have led researchers to investigate using DOT techniques to characterize the breast tumor's physiology to lower false-positive diagnoses.

Unlike x-ray mammography, DOT is an imaging modality that uses non-ionizing NIR radiation to yield three-dimensional (3-D) maps of the optical properties of illuminated tissue [16, 70, 173, 15]. Biological tissues' primary absorbers in the spectral window from around 600 to 1000 nm have relatively low absorption, allowing NIR light to penetrate through centimeters of tissues [51]. This allows the quantification of physiological properties such as hemoglobin concentration, blood volume, and blood oxygen saturation [172, 16]. Malignant tumors generally demand a greater blood supply than their surrounding tissues, leading to increased light absorption that can be delineated using spectroscopy and imaging methods, making DOT particularly useful for breast cancer imaging diagnosis [174, 175, 176, 177, 178]. Unfortunately, DOT images are known for low spatial resolution largely caused by the high scattering properties of biological tissues [16].

The low spatial resolution of DOT [179] can be improved by a multi-modal approach with x-ray mammography [180, 181, 71, 146]. The high scattering present in the breast tissue redirects photons to traverse large overlapping probing volumes before their detection, greatly reducing the locality of the measurements and resulting in blurry images. Mathematically, this is reflected as the severe ill-posedness of the inverse problem. Parallel-plate compression of breast tissues has been used in an x-ray mammography scan to minimize overlapping tissues and has also been explored for a number of standalone [177, 182] and multi-modal DOT breast imaging systems [183, 146, 184]. Multi-modal imaging approaches have been developed by leveraging tissue structural priors obtained from high-resolution imaging methods such as magnetic resonance imaging [185, 186] and

ultrasound [187]. These approach leverage the advantages of multiple modalities—they leverage high-quality structural images to constrain the DOT inverse problem for more accurate tissue physiology reconstructions.

Additionally, the DOT reconstruction can also be improved by constraining the inverse problem through more accurate surface representations of the breast. Obtaining breast surface information to aid quantitative analysis of imaging data has garnered interest from a number of applications, including DBT [188] and MRI scans [189, 190]. For multi-modal DOT systems, the 3-D shape of the breast can be estimated using the structural imaging modality such as DBT [191] or MRI [192]. When a 3-D imaging modality is not available, two-dimensional (2-D) mammography [71] has also been used to provide the shape information. In such case, a simple way to recover a 3-D breast surface is to extrude the 2-D breast contour along the compression axis [193, 194], or sweep the 2-D breast contour along the contour line extracted from an orthogonal view [195]. These methods either rely on assumptions about the 3-D location of certain features (e.g. mamilla position) or assume a constant curvature of the breast along the sweeping direction. For more accurate reconstructions of tissue optical properties, especially near the surface, measuring 3-D breast surface accurately can be greatly beneficial.

Accurately acquiring breast 3-D surface shapes has gained clinical acceptance due in large part to the plastic and reconstructive surgery communities [196, 197]. The two prominent techniques for 3-D breast surface imaging are stereophotogrammetry and laser scanning [198]. Stereophotogrammetry works by overlaying multiple images of an object taken from different view angles and triangulating the location of the object based on matching features in the multiple images [199, 200, 201]. In addition to requiring multiple cameras to increase accuracy [202], this technique is also heavily influenced by lighting conditions since features need to be extracted from multiple viewpoints [203]. Another limitation is the "ptosis error" seen during scanning of ptotic or larger breasts [204]. This arises due to the small field of view of stereophotogrammetry systems, leading to inaccuracies in breast surface and volume estimations due to the portions of the breast that are not illuminated. Laser scanning is a surface imaging technique in which rays from a laser beam are reflected off an object and detected by a detector [205]. Although laser-based acquisition systems can produce more accurate surfaces [206], these systems tend to be expensive [207, 208] and require the need for very precise setups [209]. Recently, the use of patterned-lasers and orientation-sensitive detectors has led to an increase in portable 3-D laser scanning devices [210]. While low-cost laser-based depth sensors have been widely deployed in game consoles such as Xbox or PlayStation, they are only designed to achieve relatively low spatial accuracy com-

pared to dedicated 3-D scanners. Still, patterned-laser-based surface acquisition systems generally require a minimum scanner-to-target distance of 35 cm [211, 212]. Additionally, their typical housing is too large to fit between mammography compression plates [212, 189]. Bulky instrumentation and long minimum working distance requirements make stereophotogrammetry and laser scanning techniques infeasible in the confined, low-light mammography setting.

Another widely used 3-D surface acquisition technique is SLI [213, 214]. SLI works by illuminating an object with two-dimensional spatially varying patterns with a projector and capturing images from the illuminated object using cameras [72]. The distortion of the specially designed patterns provides information regarding the shape of the object. Calibration of the camera-projector system is easily done by capturing images of a known planar pattern (e.g. a checkerboard). With the ability to use off-the-shelf components, a simple setup with a single projector and camera, and a robust and simple calibration method, SLI is positioned to provide accurate, fast, and cost-effective breast surface scanning [213]. However, similar to most patterned-laser surface scanners, commercially available SLI systems have long minimal working distance requirements and large assemblies that cannot readily fit within the confined mammography compression plates [214, 188].

Our approach to lowering false-positive diagnoses is two-fold. We first aim to improve DOT reconstruction through more accurate surface representations of the compressed breast. Second, we aim to develop a standalone DOT breast imaging system that leverages structural information through the registration of the DOT reconstruction with prior x-ray mammographies. Our group has primarily focused on the latter through the development of both multi-modal DOT reconstruction algorithms [181] and multi-modal (DOT and DBT) instrumentation that can work independently [215, 216, 217] or in conjunction with existing mammography systems [136, 180]. The approach to build DOT systems that can work independently and integrate with existing mammography systems is commercially intriguing since it can lower acquisition costs and maximize previous investments made into clinical instrumentation. We will take this same approach in our first aim—that is, the SLI surface acquisition system we build will also have the capability to function independently or be easily integrated into existing mammography systems.

In this chapter, we first describe the overall OMCI instrument and its subsystems. We then describe the design of the SLI breast scanner and detail the methods for adaptive illumination for subject-specific skin tones as well as approaches to reduce specular reflection from the compression plates. Next, we compare several traditional surface acquisition methods that leverage mammography images against our SLI-based breast surface acquisition system and quantify the impact of improved breast surface acquisition on the recovery of breast lesions using a series of simulations.

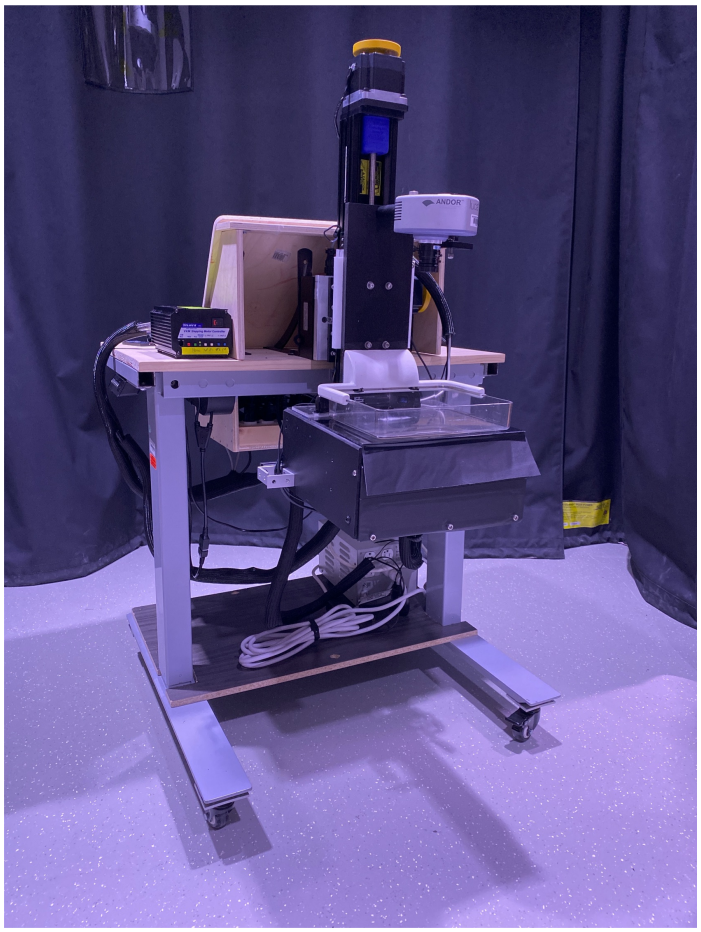

Figure 6.1: A photo of the OMCI system.

Finally, we demonstrate OMCI's use on healthy volunteers.

6.2 Methods

6.2.1 OMCI instrument

OMCI is composed of a linear stage mounted on a vertical rotary stage. The breast is compressed by a pair of acrylic plates, with one plate mounted at the stationary end of a linear stage (MN10-0160-M02-31 BiSlide, Velmex, NY, USA). Under the bottom compression plate is a box that encloses many of the optical components of OMCI. An acrylic mammography compression plate is mounted on the moving gantry of the linear stage, allowing for a plate separation ranging

from 300 mm (fully released) to 0 mm (fully closed). A linear encoder (ETI Systems, Carlsbad, CA, USA) is connected between the pair of compression plates to measure their separation. The entire breast compression assembly is mounted on a rotatory table (306045-1-s-M04-C376, Lintech, Monrovia, CA, USA), controlled by a foot pedal to permit mammography-like lateral-oblique compression. A motor driver interface (VXM-2, Velmex Inc., USA) allows both stages to be actuated independently by their stepper motor (NEMA 34 PK296 Stepper Motor, Oriental Motor Corporation, MA, USA). Two limit switches (BiSlide Push Button, Velmex Inc., NY, USA) confine the translation stage range. A reed switch (L06 Non-Contact Reed Switch, LinTech Motors, CA, USA) is used for homing the rotary stage. Four load sensors (SEN-10245, SparkFun, CO, USA) hold up the bottom compression plate and measure the pressure applied on the breast. This design specifically enables registration of structural information from separately acquired mammography scans with the DOT images using the methods detailed in our previous studies [181].

While the breast is in compression, it is illuminated with an frequency-domain (FD) and a wide-field (WF) subsystem. Bulk tissue properties are determined using a FD subsystem [218] that utilizes two laser modules (HL6750MG and HL8338MG, Thorlabs GmbH, Germany) coupled to bifurcated fiber bundle (BFY400LS02, Thorlabs GmbH, Germany). The frequency multiplexed light is driven into the OMCI box where a dual-axis galvo motor (GVS002, Thorlabs GmbH, Germany) redirects it onto different positions on the bottom of the compressed breast. A fixed detector on the top compression plate directs the light to a frequency-domain detector (C5331-04, Hamamatsu, Japan) for collection. The WF subsystem illuminates the breast from below using a continuous-wave (CW) projector (P300 Neo, Aaxa Technologies, USA) while a EMCCD camera (Andor Luca R, Oxford Instruments, U.K) located above the compression plate samples the dual-wavelength light transmitted through the breast. Both the FD and WF subsystems are controlled through the OMCI GUI written in MATLAB.

6.2.2 Dual-camera SLI breast surface scanning system

The SLI system is embedded between the compression plate to provide accurate measurement of the breast surface [Figure 6.2(c)]. This low-profile SLI scanner has a dimension of $30\times10\times4.8$ cm^3 and is attached to the stationary compression plate, on the side facing the patient's breast [Figure 6.3(a)]. It consists of a central projector (P2-B DLP Pico Projector, AAXA Technologies, Irvine, CA, USA) and two USB cameras (C525, Logitech, Lausanne, Switzerland) to reconstruct a 3-D surface of the compressed breast. The SLI scanner is designed to have a rela-

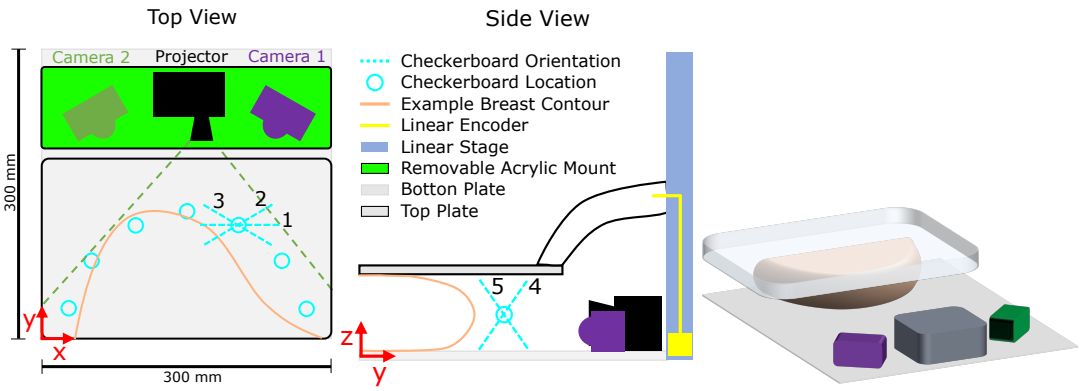

Figure 6.2: (a) Top-view of the breast compression compartment – upper: structured-light imaging system; bottom: horizontal cross-section (orange line) of the compressed breast with blue circles indicating the placement of the checkerboard used for system calibration. Numbers 1-5 indicate the 5 board orientations repeated at each location for calibration. (b) Side-view of the breast compression plates, showing the linear translation stage (blue bar on the right) and a linear encoder (in yellow), and (c) 3-D rendering of the structured-light imaging system, an acrylic bottom plate, and an acrylic compression plate (top).

tively short scanner-to-target distance, typically less than 15 cm, and a vertical profile of less than 3 cm to permit scanning breasts with a wide range of sizes. A laptop is used to control the data acquisition, including illumination pattern generation, projection, camera image acquisition, and translation stage control via an interface written in MATLAB (R2017b, Mathworks, Natick, MA, USA).

Gray-code-based binary patterns [219] are sequentially illuminated onto the breast surface and captured using both USB cameras. These patterns are characterized by their pattern order, P. A pattern set of $P = 3$ results in 3 sequences which are a reflected binary of the previous (“01”, “0110”, and “01100110”). Four bar patterns are created for each sequence (a horizontal black and white bar pattern, a vertical black and white bar pattern, and the complimentary pattern of each) [220]. The digits correspond to the white (“1”) and black (“0”) bars. In addition, a full-bright (white) and full-dark (black) pattern are added to each pattern set. Thus, a pattern set of $P = 3$ results in $4 \times P + 2$ illumination bar patterns. Complimentary Gray-code-based illumination pattern sets are used due to their robustness to decoding errors [221]. The two USB cameras have overlapping field-of-views and sequentially capture images of the breast during each illumination pattern at an exposure time of 250 ms. Dual-camera simultaneous acquisition allows the SLI system

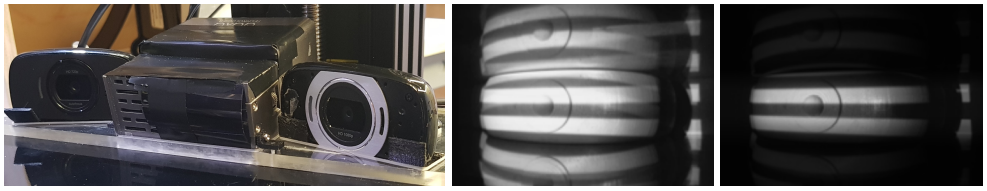

(a) (b) (c)

Figure 6.3: (a) Front-view photo of the structured-light imaging system. Cameras and projectors are embedded in an acrylic mount to prevent the need for re-calibration. (b) Horizontal bar patterns reflecting off the top compression plate and onto the breast show curved illumination bar artifacts when the scaling factor α is set to 1. In (c), we show the same illumination pattern with thickness-informed masking eliminating the curved bar artifacts by cropping the patterns exceeding the breast surface before projection. Additionally, the scaling factor is automatically calculated to prevent camera saturation.

to capture the curved surface of breasts of varied sizes without moving components.

6.2.2.1 Special data acquisition considerations

Skin tone differences are known to affect light-based surface reconstruction accuracy, especially in low-light settings. To account for skin tone variations, the normalized illumination patterns are multiplied by a scaling factor α ranging from 0 to 1 to prevent camera saturation. The scaling factor for a camera is calculated prior to data acquisition by first illuminating a full-bright pattern with $\alpha = 1$ onto the breast and capturing a single image using the camera. If the maximum pixel value of the captured image is above a preset threshold, α is decreased and the breast is re-illuminated with a full-bright pattern multiplied by the new α value. This procedure is repeated until the maximum pixel value of the captured image is less than 95% of the camera's maximum allowable pixel value. This entire procedure takes an estimated 8 seconds to complete and is repeated for each camera.

Additionally, specular reflections from the acrylic compression plates, shown in Figure 6.3(b), can produce vertically mirrored breast surfaces. To minimize such specular reflection, we use dynamic pattern masking based on real-time separation readings provided by a linear encoder. By limiting the vertical span of the illumination patterns, the patterns are projected onto the compressed breast surface without generating strong direct specular reflections from the top and bottom compression plates, as shown in Figure 6.3(c).

6.2.2.2 SLI system calibration and re-projection errors

A standard SLI camera-projector calibration is performed prior to image acquisition and is described in detail in [221]. For each camera-projector pair, a checkerboard pattern is fully illuminated in multiple positions and the corner locations are estimated in the projector's default coordinate system using a robust pixel classification algorithm [222]. The camera and projector's intrinsic parameters (optical center and focal lengths) are estimated using a calibration method described in [223] by fixing a world coordinate system to the calibration checkerboard plane.

The projector's extrinsic parameters (rotation and translation from camera to projector) are calculated using a simple stereo camera calibration [224] that treats the projector as a secondary camera. This results in a rotation matrix and a translation vector relating the camera's coordinates to the projector's coordinates. Once the 3-D coordinates of all the corners of the checkerboard are computed using the camera's (and projector's) intrinsic and extrinsic parameters, the corners are "reprojected" onto all the images for which they appear. The re-projection error is defined as the average distance between the re-projected corner locations and the actual corner location.

6.2.2.3 SLI system acquisition

The same acquisition procedures are used for both calibrating the system and acquiring breast shape measurements (Figure 6.4). A single acquisition refers to the image capture of all illumination patterns by both cameras. Camera-projector calibration requires an acquisition at each checkerboard position. During breast measurements, the acquisition is preceded by the determination of the saturation scaling factor α and masking of the patterns. Patterns during calibration are not masked since the calibration is done with the system fully uncompressed.

6.2.3 Alternative breast surface reconstruction methods for assessing SLI surface accuracy

To evaluate the accuracy of the SLI system, we compare its output against alternative surface acquisition methods. Each method estimates the surface of a 3-D breast derived from a DBT scan.

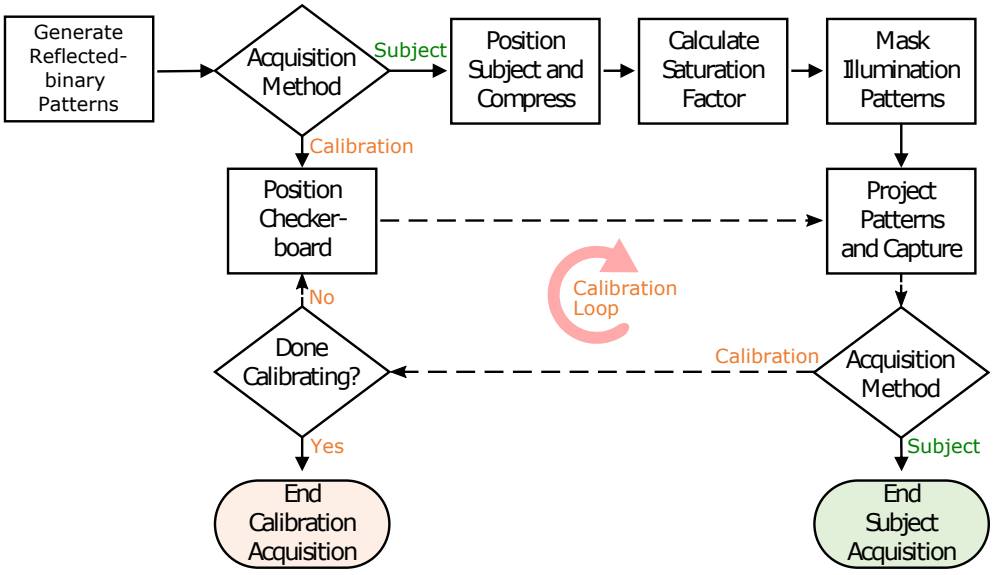

Figure 6.4: Flow chart of image acquisition for both subject measurements and system calibration. Subject measurements calculate a saturation scaling factor and mask the illumination patterns prior to projecting patterns. System calibration measurements do not mask the illumination patterns and project at full intensity. The calibration loop (dashed lines) is repeated for each location and orientation of the calibration checkerboard.

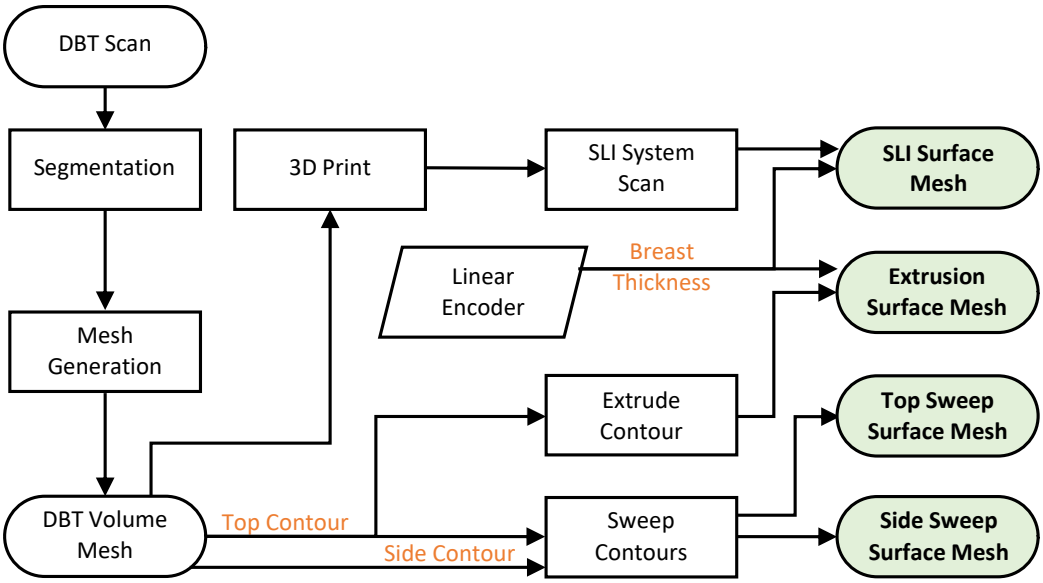

Figure 6.5: Generation of breast surface meshes using multiple acquisition methods. The digital breast tomosynthesis (DBT) volumetric mesh is created from segmented scans. The extrusion surface mesh is created by extruding the top contour to the breast thickness. The top and side contours of the DBT mesh are swept to create top and side surface meshes. The structured-light imaging mesh is created by scanning a 3-D printed breast phantom and trimming the resulting point cloud using the linear encoder measurements. The surface estimation error is calculated for each of the surface meshes by comparing the surface estimations to the DBT mesh. All surface meshes are converted to volumetric meshes for validating the effect of surface estimation methods on inclusion reconstruction.

6.2.3.1 Reference breast phantom fabrication

Figure 6.5 shows the process of creating surface meshes from DBT scans. Scans were obtained from radiology data from The Cancer Genome Atlas (TCGA) breast Invasive Carcinoma collection [225], available freely through The Cancer Imaging Archive [226]. The scan (ID: TCGA-AO-A03M) was chosen due to its large size and complex surface structure, allowing us to highlight the limitations of low field-of-view acquisition methods as well as traditional shape estimation methods that simply sweep a single breast contour. Digital Imaging and Communications in Medicine (DICOM) slices were segmented into breast and non-breast regions using ITK-SNAP [227]. Segmented slices were converted to a volumetric image and then into a 3-D mesh using a MATLAB toolbox Iso2Mesh [136] [Figure 6.6(a)].

6.2.3.2 Single and double contour sweep-based surfaces

Three alternative surface estimation methods are employed in addition to the SLI surface acquisition method. These three methods use spline models of the DBT breast contours from two different planes (Figure 6.2). The extrusion method creates a surface mesh by extruding the x/y breast contour in the z direction to the thickness of the DBT breast measured by the linear encoder [Figure 6.6(b)]. The second and third methods utilize a curve-based sweep, in which a profile (shape) follows a path (contour) to create a 3-D model. In the "top-sweep" method, the x/y breast contour profile is swept along the y/z breast contour path [Figure 6.6(c)]. Similarly, the "side-sweep" method uses the y/z breast contour as the profile and the x/y breast contour as the path [Figure 6.6(d)]. In both sweep methods, the profile normal is kept constant.

6.2.3.3 Structured-light imaging surface mesh generation

The SLI system estimates the surface of the compressed breast from the captured images while the breast is illuminated with Gray-code sequence patterns. Each camera-projector pair's extrinsic parameters are used to generate a point cloud in each camera's reference frame using Scan3d-Capture [73] [Figure 6.6(e)]. The alignment of each camera-projector pair point cloud is done by a rigid transformation of each point cloud to the projector's coordinates. The point clouds are then down-sampled using a box grid filter and merged to a single point with normal properties averaged [228]. Denoising is then performed to remove outliers [229]. The point cloud is trimmed in the z direction to the height of the DBT breast measured by the linear encoder [Figure 6.6(f)]. The trimmed point cloud is first converted to a mesh using a crust algorithm [230] prior to being

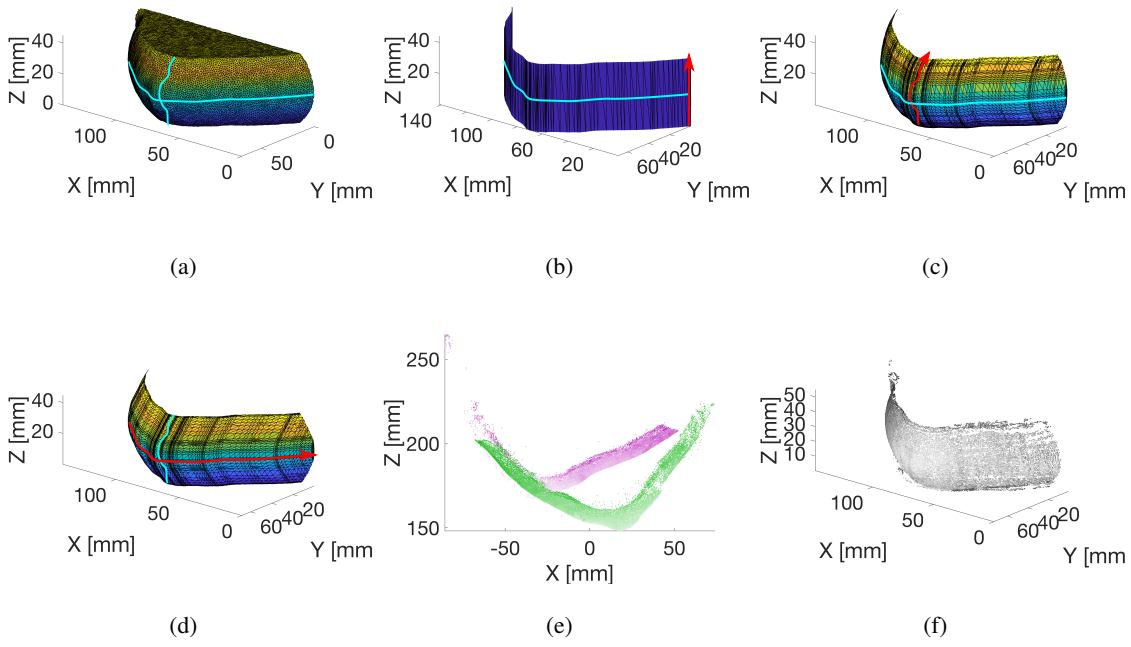

Figure 6.6: (a) Surface mesh of a digital breast tomosynthesis (DBT) model. Blue cyan lines show the x/y and y/z breast contours from the top and side views. (b) Estimate of the DBT surface using the extrusion method in which the contour (cyan) is extruded to the thickness of the breast along the z axis. (c) The top-sweep method uses the x/y contour as the profile (cyan) and the y/z contour as the path to sweep (red). (d) The side-sweep method uses the y/z contour as the profile (cyan) and the x/y contour as the path to sweep (red). (e) point clouds from both camera-projector pairs were generated by scanning a 3-D printed model of the DBT breast using the structured-light imaging system. The green (Camera 1) and magenta (Camera 2) point clouds are in the respective camera coordinates. (f) Merged and denoised point cloud in the projector's coordinates.

cropped by a bounding-box mesh with height matching the breast thickness to form a closed surface mesh.

6.2.3.4 Surface estimation error

The surface estimation error, E_s, of each surface estimation method is computed by comparing the nodes in each surface mesh to the nodes in the DBT mesh. The residual for each node in the surface mesh is the shortest distance from that node to the DBT mesh. The SLI output mesh is linearly translated (rotation and translation only) into the projector's frame using the projector's extrinsic parameters prior to determining residuals. E_s is defined as the average residual of all nodes for a particular surface estimation method.

6.2.4 Evaluation of the impact of surface errors on DOT image reconstructions

Simulations were conducted to evaluate the impact of surface estimation accuracy on DOT reconstruction accuracy for inclusions of various depths. Breast surface meshes were converted to volumetric meshes with optical inclusions and the mean squared error of wide-field DOT reconstructions was calculated for each estimation method.

6.2.4.1 Assessment of reconstruction accuracy

The effect of different surface estimations on lesion reconstruction was quantified using simulations of CW pattern-illumination sources. A 5 mm radius spherical inclusion was added at the mid-plane of each volumetric mesh at distances of 5 to 45 mm away from the nipple. The x and z coordinates of the inclusion were fixed at 68 and 22 mm, respectively. The forward simulation was conducted on a ground truth volumetric mesh consisting of the DBT volumetric mesh and a spherical inclusion. The non-linear image reconstruction of tissue properties was calculated using an iterative Gauss-Newton method in which a series of corrective terms were added to an initial guess. The reconstruction resulted in distributions, $\mu_{\mathrm{a}i}$, representing the resulting 3-D absorption coefficient (μ_a) maps at the i^{th} node for each simulated tumor location and surface model.

6.2.4.2 Reconstruction error assessment

We use mean squared error (MSE) to determine the accuracy of the image reconstruction resulting from each breast mesh. To compute the MSE, we first interpolate the reconstructed absorption map, μ_a, to the DBT mesh, and then subtract the interpolated μ_a at each node i, with the

corresponding ground truth absorption value defined on the same node, expressed as

$$\mathrm{MSE} = \frac{1}{N}\sum_{i=1}^{N}(\mu_{\mathrm{a}i} - \mu_{\mathrm{a}0i})^2, \tag{6.1}$$

where N is the total node number; $\mu_{\mathrm{a}i}$ and $\mu_{\mathrm{a}0i}$ define the recovered and ground truth μ_a values, respectively, at the i^{th} node in the DBT mesh.

6.3 Results

Results from the characterization of the SLI subsystem are broken down into three parts. We will first report the projector and camera re-projection errors of our SLI calibration using the calibration checkerboard. We then quantify the error of surface estimation methods in estimating the surface shape of the DBT breast. Finally, we show the effect of different surface estimation methods on optical property reconstruction using simulations of continuous wave pattern-illumination sources.

6.3.1 Camera-projector calibration and surface acquisition

Our dual-camera SLI system was calibrated in a dark room using a checkerboard with 5×7 internal corners with 1×1 cm^2 black and white squares. The calibration checkerboard was printed and adhered to a black Delrin surface to ensure it remained planar. To account for varying breast shapes and curvatures, the checkerboard was placed at 7 locations. At each location, camera images were captured for 5 board orientations: 1) normal to the y-axis [see Figure 6.2(a)], 2) rotated left and 3) rotated right by 30 degrees relative to the x-axis, and 4) tilted forward and 5) tilted backward by 30 degrees in the y/z plane [Figure 6.2(b)]. This results in a total of $7 \times 5 = 35$ checkerboard positions within the camera and projector field-of-views (Figure 6.2). Each rotation and tilt was measured manually using a printed protractor. The projector's resolution is 1280×720 pixels and the resolution of the cameras is 1600×896 pixels. Using a Gray-code of bit-length $P = 9$, we acquire $P \times 4 + 2 = 38$ images (see Section 6.2.2) at each board orientation/position placement. An exposure time of 0.25 seconds per image per camera results in a total one-time calibration time of $38 \times 7 \times 5 \times 2 \times 0.25 = 665$ seconds. The first camera-projector pair (Camera 1 with projector) resulted in a camera and projector re-projection error of 0.4089 and 0.2282 pixels, respectively. The second camera-projector pair resulted in a camera re-projection error of 0.4368 pixels and a projector re-projection error of 0.2889 pixels.

Table 6.1: Mean and standard deviation of the residuals of each point in a surface estimation mesh compared to the original digital breast tomosynthesis breast mesh.

	Extrusion	Top-Sweep	Side-Sweep	SLI
Surface estimation error, E_s [mm]	6.8353	0.3772	0.4726	0.2543
Standard deviation [mm]	2.8671	0.3029	0.3370	0.2723

A re-calibration is only necessary when the relative position of the cameras and projector is changed. Once calibrated, the SLI system can acquire a surface scan in about 35 seconds, including 16 seconds for adaptively adjusting the intensity scaling factor α for both cameras (see Section 6.2.2.1 for details) and 19 seconds for image acquisition ($38 \times 2 \times 0.25 = 19$ s).

6.3.2 Surface estimation errors

The DBT breast model was 3-D printed (Ender 5, Creality, China) with a 0.1 mm layer height using white PLA filament. The 3-D printed DBT breast was placed in between the compression plates, compressed to the thickness of the printed DBT phantom, and scanned using the dual-camera SLI system. The saturation scaling factors α were automatically determined using twenty iterations, resulting in a $\alpha = 0.8$ for both cameras. The two point clouds from each camera-projector pair were transformed to the projector's coordinates, down-sampled, and merged prior to being denoised with the number of nearest neighbor points set to four and the outlier threshold set to one standard deviation from the mean of the average distance to those four neighboring points. The resulting point cloud from the SLI system scan has 35,256 points.

Table 6.1 shows the mean and standard deviation of the residual of all the nodes in the estimated breast surface mesh. The z-extrusion method (EXT) results in the largest error (E_s) of all compared methods. While the top-sweep, side-sweep, and SLI methods all had similar standard deviations, the SLI method resulted in the smallest E_s.

6.3.3 Mean square error of optical property reconstruction

DOT reconstructions were performed using our in-house data analysis toolbox, Redbird-m [54]. An L-curve analysis [231] is used to determine the regularization parameter as 3.16×10^{-10}, which is fixed over 10 Gauss-Newton iterations. The absorption coefficient of the spherical inclusion was set to be twice ($\mu_a = 0.016$/mm) that of the background tissue ($\mu_a = 0.008$/mm). The reduced scattering coefficient μ_s' was set to 1 mm^{-1} for both breast and inclusion tissues. A set of 32 (16 vertical, 16 horizontal) moving-bar source patterns [27] covering an area of 40×40 mm^2

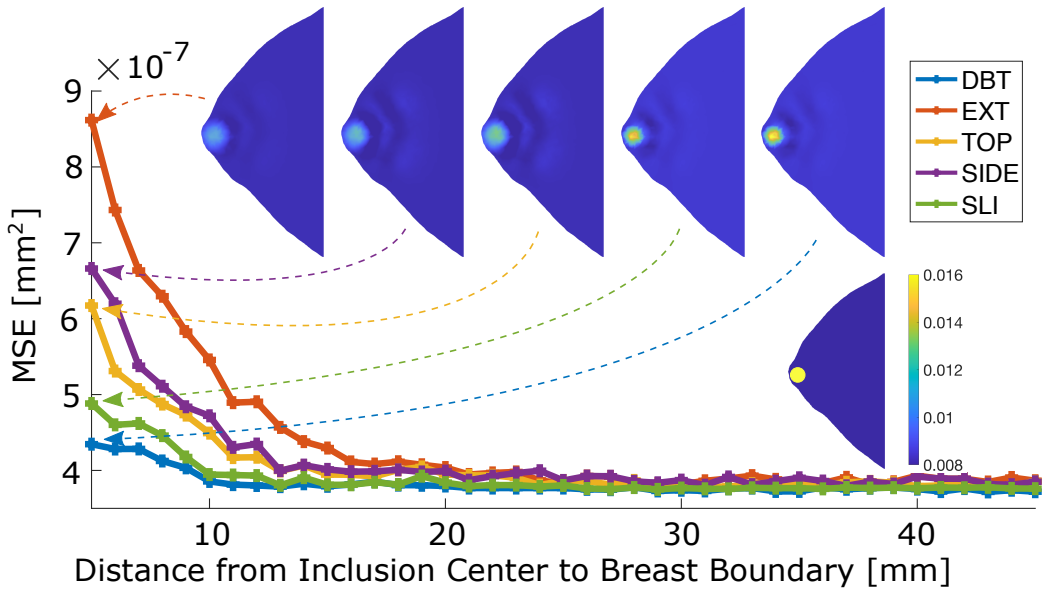

Figure 6.7: A comparison between the mean squared error (MSE) of the reconstructed absorption map using 4 estimated surfaces (EXT - z-axis extrusion, TOP - sweeping x/y contour along y/z contour, SIDE – sweeping y/z contour along x/y contour, and SLI – surface acquired from our structured-light imaging system) as well as the ground truth digital breast tomosynthesis surface. A 1 cm diameter spherical inclusion is moved away from the breast surface at various depths between 5 and 45 mm in 1 mm increments. Image slices (in x/y plane) of the reconstructed absorption coefficient (μ_a in mm^{-1}) (top-row) and the ground truth μ_a (bottom-right) are shown as insets.

was centered at the spherical inclusion. Iso2Mesh [136] was used to interpolate nodal values from the reconstructed mesh to the ground truth mesh based on linear interpolation in order for all reconstructed meshes to have the same number of nodes.

The MSE errors from these reconstructed images are summarized in Figure 6.7, showing the effect of different surface estimation methods on the accuracy of optical property recovery. Overall, surface mesh accuracy appears to have a notable impact on relatively shallow tumors, with a depth of less than 25 mm. MSE values obtained using the SLI method closely follow those using the ground truth DBT mesh for most inclusion depths. The top- and side-sweep-based meshes followed similar trends, however, reporting higher errors compared to SLI especially when the tumor is relatively shallow. The maximum MSE value for the SLI mesh at a distance of 5 mm from the surface (4.89×10^{-7} mm^2) was 23% higher than the maximum MSE value for the DBT mesh (4.35×10^{-7} mm^2). In contrast, the single-axis-extrusion method MSE was nearly twice higher (8.62×10^{-7} mm^2) than that from the DBT mesh. Although the DBT and SLI mesh MSEs plateau to their minimum around 15 mm from the surface, top-, side-, and extrusion-based mesh MSEs continue to decrease until a depth of 25 mm. Beyond the depth of 25 mm, the errors between different methods become minimal.

6.3.4 Full system *in-vivo* patient results

Figure 6.8 shows the results from an OMCI full system acquisition on a healthy subject. The images were provided by Edward Xu, who acquired the data from an Institutional Review Board (IRB) approved study at Massachusetts General Hospital (MGH) in Danvers, MA. Figure 6.8(a) shows the breast mesh generated using the SLI subsystem. In particular, the SLI subsystem was able to capture the patient's nipple as well as the amount of breast surface in contact with the top and bottom compression plates. In Figure 6.8(b), we overlay the SLI breast mesh nodes onto the acquired image from the Andor camera positioned above the top compression plate. A black cloth was placed around the breast to mask any illumination from the CW system that was outside the breast profile. Notably, the breast nodes follow the contour of the breast. Finally, in Figure 6.8(c), we show the results of HbT concentration of a healthy volunteer breast. The bulk optical properties were obtained using the radio frequency (RF) subsystem while the CW pattern-based reconstruction was constrained by the SLI mesh.

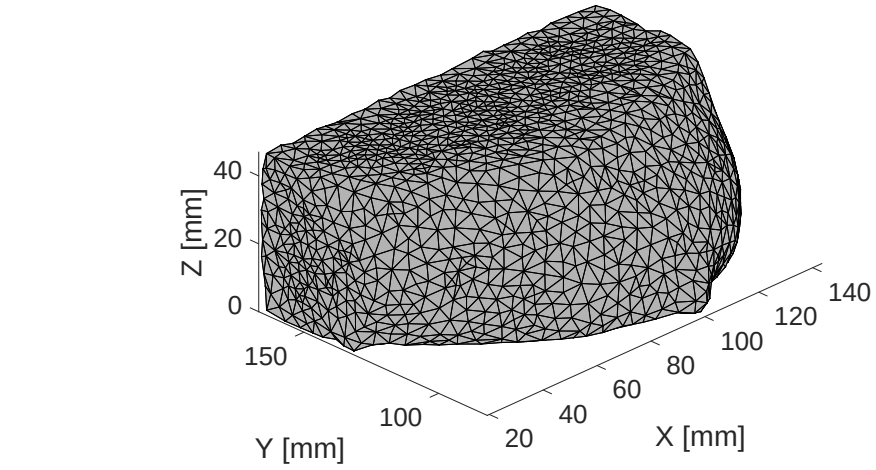

(a)

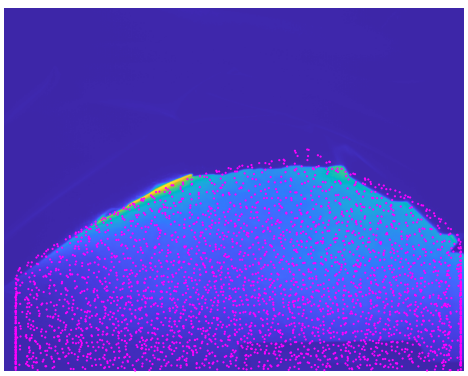

(b)

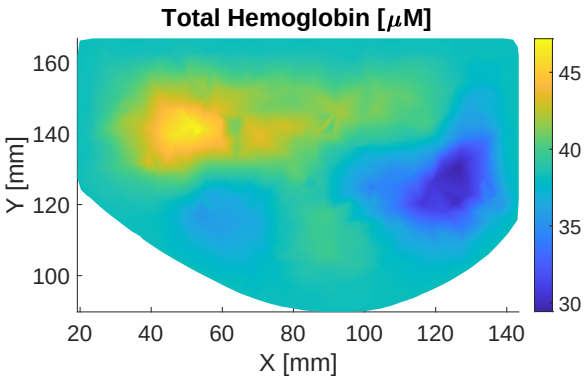

(c)

Figure 6.8: (a) Resulting breast mesh from using the structured-light imaging (SLI) subsystem on a healthy subject. (b) The SLI mesh overlaid on the acquired Andor camera image. Red dots correspond to nodes in the SLI mesh. (c) Total hemoglobin concentration results when all four subsystems work in tandem. Results courtesy of Edward Xu.

6.4 Discussion

The camera and projector re-projection errors in Section 6.3.1 represent an average error of fewer than 0.5 pixels in estimating the corner locations of a calibration checkerboard placed between 50 and 250 mm away [Figure 6.2(b)] from the projector for all 35 checkerboard positions. Although the same illumination patterns and calibration checkerboard positions were used to calibrate each camera-projector pair, we find a slightly better calibration accuracy when the projector is paired with Camera 1 since Camera 1 is closer to the projector's lens (Figure 6.2). The discrepancy in the re-projection errors of the two pairs is due in part to the asymmetry of the dual-camera setup. The asymmetry arises from the projector offset relative to its housing, making one camera closer to the projector than the other [Figure 6.2(a)].

From Table 6.1, the single-axis extrusion method resulted in the highest surface error because it does not account for the curvature of the breast in the y/z plane [Figure 6.6(b)]. Table 6.1 indicates that, on average, points in the extrusion-method-derived surface estimation mesh are approximately 6.84 mm away from the DBT mesh. The top- and side-sweep methods decrease the surface estimation error by incorporating a second breast contour from the y/z plane [Figures 6.6(c) and 6.6(d)]. Both methods improve the accuracy of surface estimations by approximating the 3-D curvature of the breast. We want to point out that both top-sweep and side-sweep methods require an additional camera to obtain two orthogonal views of the breast [232], which does not necessarily lead to simplified hardware compared to the SLI setup considering the mounting space constraints and lighting conditions [188]. While also requiring two cameras, our mammography-tailored SLI system can produce sub-millimeter resolution of the surface compared to the reference DBT breast model based on Table 6.1.

Our results also demonstrated that the improvement in surface estimation accuracy can lead to improved DOT reconstruction accuracy. Figure 6.7 shows using breast surfaces derived from SLI can accurately recover the absorption profile compared to those recovered using the ground-truth (DBT) mesh at most tested tumor depths. For superficial/shallow ($<$ 10 mm) tumors, the top- and side-sweep surface estimation methods followed similar trends to each other, reporting MSEs about 50% higher compared to those from using ground-truth (DBT) surface models, and about 30% higher than those from using SLI surfaces. As expected, the effect of the surface accuracy decreases as the inclusion is moving further away ($>$ 25 mm) from the skin.

Despite the ability to produce sub-millimeter resolution of breast surfaces in poorly lit and confined mammography-like settings, both our SLI system and our analysis have limitations.

Firstly, the span of the output point cloud from our SLI system is limited to the area of the breast that is well-illuminated by the projector. As a result, tissue boundaries near the chest wall or those in direct contact with the compression plate may not be well covered due to the limited angles of the projector/camera line-of-sight. Still, for DOT of a compressed breast, capturing a significant portion of the front-facing breast tissue as our system does, provides quantitative differences in reconstructions, as shown above. Future improvement of this system should consider using more compact, wide-angle projectors, higher resolution cameras, and patterns with higher order binary codes to both expand the field-of-view and increase the point cloud resolution. Secondly, a 3-D printed breast model was used to experimentally compare different shape acquisition methods. Different choices of extruder sizes, filament colors, and printing techniques could impact the surface texture of the printed phantom and slightly alter the surface estimation errors. Finally, the quantification of reconstruction errors was based on simulations using a single set of pre-determined breast models, tumor size and shape, tumor contrast, and wide-field pattern size. An experimental validation using heterogeneous phantoms may produce more realistic comparisons.

OMCI is a very complex DOI system, on par with state-of-the-art commercially available mammography systems. The challenge is to make these sophisticated systems scalable through creative explorations of portability, modularity, and high-optode-density architectural attributes. A few aspects made our standalone DOI system portable. Not only was the system assembled on a movable chassis with wheels, but its dimensions were also chosen to fit within doors to allow for the system to be mobile within clinics. Additionally, the SLI subsystem was designed to be easily dismounted and re-mounted without the need to re-calibrate. Each of the four subsystems connects to a single laptop through a USB bus, allowing researchers to easily add new subsystems in the future. Not only can individual systems be upgraded or swapped out as needed, but the OMCI GUI can selectively toggle subsystems on/off to decrease acquisition times when not all subsystems are needed. Additionally, the design of each subsystem allows OMCI to be used as a platform for investigating reconstruction algorithms through simple adjustments such as varying the SLI or CW illumination patterns, varying the RF source locations using the galvos, or easily changing the wavelengths used for bulk-property estimation. Finally, the high-density architecture attribute was explored through wide-field trans-illumination and camera-based imaging. Rather than individual sources and detectors, OMCI can probe large areas more efficiently, decreasing the time the patient's breast is in compression. At the same time, the accuracy of these high-density measurements is improved through the use of the SLI subsystem to constrain the reconstruction with high-resolution breast shape meshes.

CHAPTER 7

3-D printable optical phantoms

Scalability of DOI systems is attained not merely by technological advances that address architectural attributes, but through facilitating the validation of new DOI systems. While the systems in Chapters 3, 5, and 6 provide strong evidence of the benefits of improving portability, modularity, and high-optode-density in complex DOI and NIRS systems, Chapter 4 and this chapter focus on providing the community with frameworks to facilitate the exploration of these architectural attributes in the long term. In this chapter, we present the initial progress towards developing a standardized method to create geometrically complex phantoms to validate the expected performance of new DOI systems. Through filament characterization processes and creative slicing methods, we are taking the first step in standardizing and automating the manually-intense process of fabricating optical phantoms.

7.1 Introduction

In order to evaluate the performance of the NIR diffuse optical imaging and spectroscopy systems we have built, we need to use phantoms. Phantoms are physical samples carefully made to mimic the optical properties of human tissues [37]. By imaging these objects of known optical properties, we can evaluate the accuracy of a new system by comparing its result against existing systems. Creating these phantoms is complex: not only do you need to create recipes that lead to desired optical properties, but phantoms must also be manufactured in specific geometries tailored to what the DOI system will measure. To address the optical properties, phantom makers tend to focus on mimicking the absorption coefficient (μ_a) and the reduced scattering coefficient ($\mu_s^{'}$) of biological tissue [39] by using mixtures of scattering agents and absorbing pigments with a clear

base [40, 41]. The shape of the phantom is typically created using traditional fabrication techniques, either mold casting [42] or spin coating [44].

Traditionally, as DOI was in its infancy, these methods sufficed for simple phantoms. However, these methods fall short of supporting complex geometries. As new DOI systems are developed to image the brain [233, 234] and the breast, we will need to evaluate their performance with phantoms that have complex structural and physiological properties. While some phantom makers use intricate methods and procedures to develop geometrically complex phantoms [43], these phantoms take days to manufacture, require lots of equipment and expertise, and the manual process leads to geometry and optical property variations due to human variability. Thus, to support the system development, calibration, and testing of new imaging methods [235, 236] (like the DOI systems developed in this dissertation), we need a new method to manufacture phantoms with spatially varying optical properties and anatomically accurate geometries.

Rather than add structure-generating methods to traditional phantom making, we propose a method to add customizable optical properties to a digital fabrication method that is already engineered to produce arbitrary geometry—fused-deposition modeling (FDM). FDM is a form of 3-D printing that creates a 3-D object by adding solid material layer-by-layer [41]. While traditional 3-D printing uses a single filament material to generate a 3-D object, we proposed the mixing of grey (absorbing), white (scattering), and transparent (base) filament colors to produce the desired optical properties.

3-D printing for phantom development allows for customizable properties using raw printing materials and the creation of spatially varying optical properties within a 3-D printed phantom. This allows the creation of a wide range of phantoms with precisely known optical properties, geometries, and inclusions of various resolutions (size, shape, depth). Most significantly, the design of a 3-D printed standardized calibration phantom for DOT minimizes geometry and optical property variations due to human variability. In this way, researchers can manufacture identical phantoms using *in-situ* materials with resolutions limited only by their 3-D printer, effectively allowing independent DOT systems to be characterized by the same exact phantom.

In this chapter, we will detail our method to develop 3-D printed phantoms. We will first describe a workflow to characterize new filaments to account for variations in lots of the same color filament. We then show details of a slicer with the ability to slice an assembly of multiple standard tessellation language (STL) files. The slicer is able to assign filament ratios (tissue types) to each individual STL, allowing the printer to adjust the mixing ratio of the extruder as it prints embedded inclusions into the large geometric print. Finally, in order to encourage the use of our method, we

will disclose a list of lessons learned to help others attempt to replicate our phantoms.

7.2 3-D Printing Hardware

This project utilizes an experimental FDM multi-material 3-D printer (QuadFusion, M3D). This marlin-based printer has an extrusion bar-based frame and uses stepper motors to control motion. The extrusion head is composed of small stepper motors to guide four filaments through a metal nozzle with a polytetrafluoroethylene (PTFE) insert. The PTFE insert is a cylindrical piece with 4 milled holes that extend from end to end. Mixing occurs in the nozzle tip. Due to the need to mix filaments into one nozzle exit, we used polyethylene terephthalate glycol (PETG) instead of the standard PLA filament. PLA is the most popular thermoplastic for 3-D printing because of its cost, ease of print (it is semi-flexible and very forgiving), and it does not off-gas any fumes. However, PLA is difficult to mix with other materials due to its limited temperature range. At high temperatures (above 200° Celsius), PLA releases water which causes a high-pressure build-up in nozzles. To resist the higher temperate and water, PETG is used. PETG is more viscous at higher temperatures, allowing it to easily fuse with other PETG filaments.

7.3 Filament Characterization

The filament profiles are the derived settings used for a particular filament spool. Although the majority of printing settings are consistent across PETG filaments, certain features must be accounted for, particularly, the extrusion multiplier (EM) and retraction amount. EM is a setting used to account for variability in extrusion amounts. An EM of 1 means that 1 mm of filament is extruded for every 1 mm requested. Due to the filament path (the Bowden tube, motor teeth, varying temperatures), certain filaments in certain printers may require over- or under-extrusion to extrude the correct amount of filament. The retraction amount is the amount of filament to pull back up into the nozzle as the print head moves in between printing paths. When this value is too low, you will see “stringing” in prints from the oozing of material while the head is in motion. Too much retraction and the printer will not print the first few millimeters upon restarting since the nozzle is empty of filament.

To account for variations in filaments of the same color by the same manufacturer, we have developed a method to characterize filaments and create filament profiles for each spool of filament. In fairness, the variability in the extrusion multiplier is not entirely due to the manufacturer. The

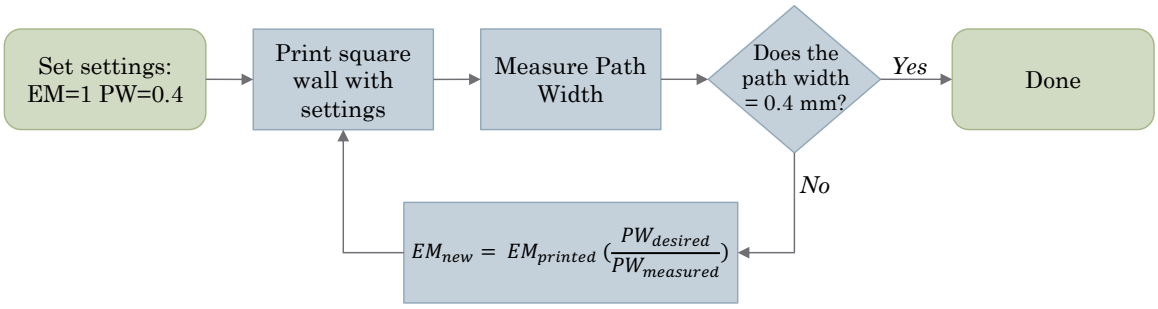

(a)

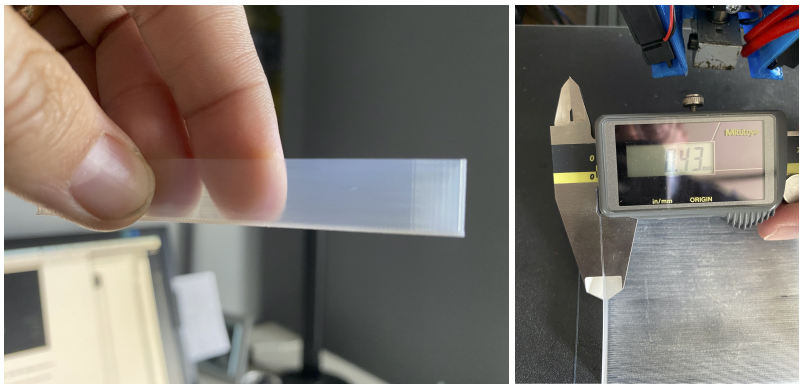

(b) (c)

Figure 7.1: (a) Flowchart showing how to use measured path widths to adjust extrusion multiplier values when characterizing filaments. (b) Printed square wall using clear filament. (c) Caliper measurements show over-extrusion.

QuadFusion head is a complex head that requires filaments to be driven through curved paths and high pressure that result in friction. We calculate filament-specific EMs for each spool used in our printer by printing a square wall with the thickness of a single path width (PW). We then calculate the new EM based on the desired path width and the actual path width of the print using the formula $EM_{new} = EM_{printed} \times (PW_{desired}/PW_{measured})$. The steps are outlined in Figure 7.1(a).

A 3-D printed tissue type is simply a mixing ratio of multiple characterized filament profiles. While one filament profile informs of the settings for printing a single filament, we have to create combined printing settings when mixing multiple filaments (tissue types). This is done as a weighted average of the settings scaled by the mixing ratios. For example, if white, grey, black, and clear filaments each have extrusion multipliers of 1, 0.98, 1, and 0.9, respectively, and we want to mix them in a 30/20/0/50 ratio, then the final extrusion multiplier would

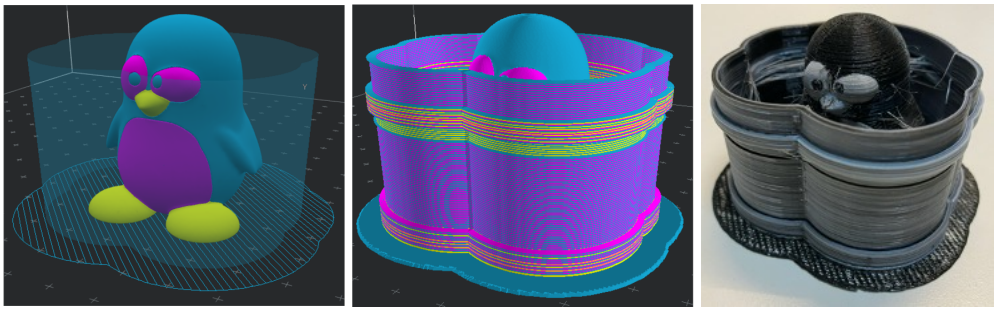

(a) (b) (c)

Figure 7.2: The "caging" purge method (a) An example penguin composed of three different tissue types. (b) The same penguin model with the cage shown. The colors of the cage indicate the colors on that segment of the print. (c) Resulting 3-D printed penguin.

be $(1 \times 30 + 0.98 \times 20 + 1 \times 0 + 0.9 \times 50)/(30 + 20 + 0 + 50) = 0.946$. Similarly, the extrusion motors are driven at scaled rates based on the filament mixing ratio.

7.4 Multi-filament Slicing Artifacts for Purging Nozzle During Tissue Transitions

One difficulty in fused multi-material 3-D printing not found in single filament printing is the need to purge the nozzle in between changing mixing ratios for different tissue types on the same layer. For example, if we want two separate mixing ratios for concentric rods, the nozzle needs to be purged in between printing the outside color ratio and printing the inside color ratio. Purging refers to the extrusion of sacrificial filament when the outputted mixed filament is transitioning between two different ratios (tissue types).

We have implemented a "caging" method in which a cage is built around the print to purge the nozzle. The method is an extension of the "brim" artifact commonly used to help prints adhere to the print bed. Essentially, at every layer, concentric shapes around the model are printed for each ratio. This allows the nozzle to fully transition to a new mixing ratio prior to continuing the print. This results in a "cage" of sacrificial filament around the print.

7.5 Lessons learned for use of PETG in filament mixing

The use of PETG filament, a "caging" purging method, mixed filament ratio-based extrusion multipliers, and an experimental FDM 3-D printer has taught us many lessons. To facilitate future researchers in this space, here is a list of lessons learned and pitfalls to avoid.

- BED MATERIAL: PETG sticks very well to the printing bed. The use of sacrificial generic blue painter's tape on the print bed will facilitate removal by removing the print from the bed by pulling on the tape itself.
- BED LEVELING: Add a decent gap between the nozzle and the bed. Typical 3-D printers level the bed by using a single sheet of regular printing paper as the unit of measure between the nozzle and the print bed. To account for the "gooey"-ness of PETG, use 3 sheets of paper.
- BED TEMPERATURE: Start the bed temperature around 80° C. Do not heat above 100° C. Higher bed temperatures are better for bed adhesion, but PETG already adheres pretty well. Consider decreasing the space between the nozzle and the bed before increasing the bed temperature.
- NOZZLE TEMPERATURE: PETG prints between 230 and 250° C. However, PTFE (which is what the tube that aligns the filaments prior to being mixed in the nozzle is made of) has a melting point between 250 and 260° C. Start at 230° C and do some test prints. If you hear a knocking noise during printing, your extruder is skipping, and you should increase the nozzle temperature by 5° C.
- RETRACTION SPEEDS: Do not retract PETG at high speeds. Set the retraction speed to around 25 mm/s. The retraction distance should be set to about 3 or 4 millimeters for direct drive extruders. With PETG, the retraction speed is more important than distance. If you still have oozing and stringing, try lowering the retraction speed.
- TRAVEL SPEED: One more parameter that will help in reducing oozing is the travel speed. PETG tends to drip from the tip of the nozzle, especially if the nozzle temperature is high. To combat this, try increasing the travel speed to reduce the time the printer is not actively extruding.
- PRINT SPEED: PETG is very sensitive to print speed. Printing too fast results in poor layer adhesion, extruder skipping, and low print quality. Printing too slow results in deformed parts,

stringing, and oozing. A good place to start is between 50 and 55 mm/s. We suggest 25 mm/s for the first layer and the outer wall, while travel moves should be as fast as possible, at least 120 mm/s, to avoid oozing.

- FANS: We recommend printing without fans for the first two layers. All other layers should have the fan running at 100%.

CHAPTER 8

Conclusions

This dissertation was an attempt to scale the advantages of DOI by addressing certain architectural limitations of modern imaging systems, namely portability, modularity, and optode density. We believe that the system features that arise through exploring these architectural attributes contribute to increasing the number of applications of DOI across populations and settings. By developing hardware and software frameworks that simplify the design and analysis of complex imaging systems, we can more easily manage the growing number of components, subsystems, and computational needs of modern imaging systems, enabling their scalability.

First, we designed, built, and characterized three NIR DOI systems—MOXI, MOBI, and OMCI. Our exploration of the challenge to improve the portability of traditional oximeters led to the development of a mobile-phone-based pulse oximeter, MOXI, that leverages optical sensors and computational resources embedded inside already ubiquitous mobile phones. By using a mobile application to calculate, display, and store oxygenation readings, we developed a way to easily distribute our oximetry system to many users while at the same time providing a way to easily share information with remote stakeholders. Our wearable functional brain imaging system, MOBI, was not only portable but also wearable. The portability of this neuroimaging system was increased through its use of lightweight flexible-circuit boards and low-power components that allowed the system to be battery-powered. MOBI also attempted to facilitate the use of the complex modular architecture by implementing an automatic connection topology detection method that requires no user input, freeing a user to focus on the use of a system rather than its setup. The use of the modular architecture also permitted a higher-density probe through the use of channels with sources and detectors on neighboring modules. Moreover, we mitigated the expected disadvantage that comes with the use of high-density probes (longer acquisition times) through the introduction of a spatial

multiplexing encoding strategy to improve full probe frame rates. Finally, by designing OMCI as a collection of multiple subsystems, we were able to build a sophisticated, standalone, optical mammography system that can be easily wheeled throughout a clinic. Portability was further augmented through a design that allowed the SLI subsystem to be removed and re-attached without the need to re-calibrate, and through the development of an OMCI GUI that allows for the control of all subsystems from a single laptop. This assembly method incorporates a modular attribute into complex DOT systems by allowing the ability to test, upgrade, and swap out individual imaging subsystems, permitting users the ability to constantly use the latest version of components. Additionally, its modular design elevates OMCI to a research platform by allowing simple changes of its settings such as alternate CW illumination patterns or different RF source positions. Lastly, OMCI directly implements high-optode-density imaging through wide-field illumination and camera-based detection, allowing for the imaging of large volumes without increasing acquisition times.

Although our systems implemented features that addressed portability, modularity, and optode density, our explorations quickly led to unanticipated challenges that arose when we adopted these architectural attributes. For example, as we were designing a modular fNIRS system, we were required to make many design decisions early in the process, such as the module shape, the module dimensions, the number of sources and detectors within a module, and the layout of those optodes. We learned that scalability could not be enabled without a systematic method to tackle the complexity of designing in the modular architecture space. MOCA is the answer to this emerging challenge, providing fNIRS developers with a systematic yet easy-to-use software platform to navigate the large design space of modular fNIRS probes and provide metrics-based guidance. MOCA simplifies the design problem with module-level parameters such as size, shape, and optode layout as well as probe-level parameters such as the maximum source-to-detector separation and ROI geometry to characterize a modular probe. It offers the ability to perform operator-guided sweeping of probe parameters such as orientation, spacing, and module staggering offset, helping designers explore alternative designs that potentially improve upon existing probes or outline spectra of trade-offs. MOCA is quantitative, guided by application-specific fNIRS performance metrics, including channel distribution, average brain sensitivity, and spatial multiplexing groups, making it possible for quantitative characterization and comparison between various design decisions. Similarly, we unearthed an unanticipated challenge when validating our newly developed systems. Although the method to validate new instruments is identical, each new system requires system-specific anatomical phantoms with optical properties tailored toward its application. If we expect scalability of DOI to occur through the development of new imaging systems, we must also support the field through

the development of geometrically accurate phantoms that allow researchers to easily validate the performance of these systems. In Chapter 7, we detailed a method for characterizing new filaments for use in multi-material fusion-based 3-D printing. We also show a modified brim method for efficiently purging filament when a print changes between mixing ratios on a single layer. Through this process, we show how we can design and set up the fabrication of anatomically complex optical phantoms for validating arbitrary DOI systems, including the three systems developed for this dissertation.

Due to their potential advantage, the field has trended towards adopting and improving portability, modularity, and high-optode-density features in diffuse optical systems. The work in this dissertation is heavily influenced by that trend. However, these three attributes are not the only attributes that contribute to the scalability of optical systems, and thus, we cannot over-generalize the benefits we have reported. There are a plethora of attributes such as cost, interoperability, and ease of manufacture that contribute to the potential of optical imaging to scale, and each likely has unanticipated challenges that will arise as those architectural attributes are adopted. Therefore, the field needs to not only expect and address those emerging challenges, but we also need to address the limitations of the work in this dissertation. For example, MOXI is intended to address a challenge with neonate mortality rates but has only been tested in adult subjects. It first needs to be validated on neonates before being deployed for use in a LMIC. Despite demonstrating preliminary *in-vivo* results, MOBI still requires work. Not only does it need a complete headgear design to mount all the modules together, but the robustness of the FPC cables also needs to be tested in high-motion environments. Additionally, the results shows were acquired on a subject with short hair. In order to be truly portable, MOBI needs to both improve its SNR as well as find hardware and/or software methods to deal with the notorious hair artifacts present in all fNIRS measurements. Similarly, the *in-vivo* results presented for OMCI were done on a small number of volunteers. Further studies using a larger sample size need to be conducted to increase our confidence in the performance of this system. Moreover, our software frameworks also have limitations. MOCA currently implements default parameters that are biased based on the current literature. To truly provide a comprehensive design platform, ergonomic, usability, and communication considerations should also be codified and implemented. Additionally, our 3-D printing method needs a thorough investigation of the variability and accuracy of the optical properties resulting from the mixed filaments, including the effect of different slicing properties such as infill patterns and layer heights.

The aim of this dissertation was to contribute to the enablement of scalability of optical imaging and spectroscopy systems by exploring varied implementations of architectural attributes

of portability, modularity, and optode density. We first identified three modern application, user, and setting-specific grand challenges that would demonstrate the potential broad application of NIR imaging. We then designed, developed, and validated three imaging systems that incorporated implementations of architectural attributes, including a mobile-phone-based pulse oximeter, a modular neuroimaging instrument, and a standalone DOT system. Additionally, we developed two workflows to address two unanticipated challenges that arose when adopting these attributes. Through demonstrating technical implementations and through developing frameworks and methods that assist researchers in the initial design and the final validation of optical systems, we expect to attract more research interest in scaling optical imaging methods. We invite researchers to accelerate the investigation and creation of the next generation of optical systems through the use of our tools and the incorporation of our lessons to advance the state-of-the-art of NIR DOI systems.

REFERENCES

[1] Elizabeth A. Krupinski and Yulei Jiang. Anniversary Paper: Evaluation of medical imaging systems. *Medical Physics*, 35(2):645–659, 2008.

[2] Richard B Gunderman. *X-ray vision: the evolution of medical imaging and its human significance*. Oxford University Press, 2012.

[3] Béatrice Lauby Secretan, Chiara Scoccianti, and Dana Loomis. Breast-Cancer Screening — Viewpoint of the IARC Working Group. *New England Journal of Medicine*, 372(24):2353–2358, 2015.

[4] Marcel Beister, Daniel Kolditz, and Willi A Kalender. Iterative reconstruction methods in X-ray CT. *Physica Medica*, 28(2):94–108, 2012.

[5] Cynthia H McCollough, Shuai Leng, Lifeng Yu, and Joel G Fletcher. Review: Dual-and Multi-Energy CT. *RSNA Radiology*, 276(3):637–653, 2015.

[6] Regina J. Hooley, Melissa A. Durand, and Liane E. Philpotts. Advances in digital breast tomosynthesis. *American Journal of Roentgenology*, 208(2):256–266, 2017.

[7] John K Iglehart. The New Era of Medical Imaging — Progress and Pitfalls. *New England Journal of Medicine*, 354(26):2822–2828, 2006.

[8] Paul Suetens. *Fundamentals of medical imaging*. Cambridge University Press, 3rd edition, 2017.

[9] Frederic H. Fahey. Data acquisition in PET imaging. *Journal of Nuclear Medicine Technology*, 30(2):39–49, 2002.

[10] Donald B. Plewes and Walter Kucharczyk. Physics of MRI: A primer. *Journal of Magnetic Resonance Imaging*, 35(5):1038–1054, 2012.

[11] Vincent Chan and Anahi Perlas. *Basics of Ultrasound Imaging*, pages 13–19. Springer New York, New York, NY, 2011.

[12] Eugenio Picano. Sustainability of medical imaging. *BMJ*, 328(7439):578–580, 2004.

[13] Jørgen Arendt Jensen. Medical ultrasound imaging. *Progress in Biophysics and Molecular Biology*, 93(1-3):153–165, 2007.

[14] Qinghua Huang and Zhaozheng Zeng. A Review on Real-Time 3D Ultrasound Imaging Technology. *BioMed Research International*, 2017:6027029, 2017.

[15] Yoko Hoshi and Yukio Yamada. Overview of diffuse optical tomography and its clinical applications. *Journal of Biomedical Optics*, 21(9):091312, 2016.

[16] D A Boas, D H Brooks, E L Miller, C A DiMarzio, M Kilmer, R J Gaudette, and Quan Zhang. Imaging the body with diffuse optical tomography. *IEEE Signal Processing Magazine*, 18(6):57–75, 2001.

[17] Gary D. Luker and Kathryn E. Luker. Optical imaging: Current applications and future directions. *Journal of Nuclear Medicine*, 49(1):1–4, 2008.

[18] Victor T. C. Tsang, Xiufeng Li, and Terence T. W. Wong. A Review of Endogenous and Exogenous Contrast Agents Used in Photoacoustic Tomography with Different Sensing Configurations. *Sensors (Basel, Switzerland)*, 20(19), sep 2020.

[19] James E. Crum. Future Applications of Real-World Neuroimaging to Clinical Psychology. *Psychological Reports*, 124(6):2403–2426, 2021.

[20] Joanne L. Park, Paul A. Dudchenko, and David I. Donaldson. Navigation in real-world environments: New opportunities afforded by advances in mobile brain imaging. *Frontiers in Human Neuroscience*, 12(September):1–12, 2018.

[21] Fabian Herold, Patrick Wiegel, Felix Scholkmann, Angelina Thiers, Dennis Hamacher, and Lutz Schega. Functional near-infrared spectroscopy in movement science: a systematic review on cortical activity in postural and walking tasks. *Neurophotonics*, 4(4):041403, 2017.

[22] Meryem A. Yücel, Juliette J. Selb, Theodore J. Huppert, Maria Angela Franceschini, and David A. Boas. Functional Near Infrared Spectroscopy: Enabling routine functional brain imaging. *Current Opinion in Biomedical Engineering*, 4:78–86, 2017.

[23] Hubin Zhao, Sabrina Brigadoi, Danial Chitnis, Enrico De Vita, Marco Castellaro, Samuel Powell, Nicholas L. Everdell, and Robert J. Cooper. A wide field-of-view, modular, high-density diffuse optical tomography system for minimally constrained three-dimensional functional neuroimaging. *Biomedical Optics Express*, 11(8):4110, 2020.

[24] Ernesto E. Vidal-Rosas, Hubin Zhao, Reuben Nixon-Hill, Greg Smith, Luke Dunne, Samuel Powell, Robert J. Cooper, and Nicholas L. Everdell. Evaluating a new generation of wearable high-density diffuse optical tomography (HD-DOT) technology via retinotopic mapping in the adult brain. *Optics InfoBase Conference Papers*, 8(2):1–24, 2021.

[25] Guangda Liu, Wenjie Cui, Xinlei Hu, Ruolan Xiao, Shang Zhang, Jing Cai, Jiqing Qiu, and Yuan Qi. Development of a miniaturized and modular probe for fNIRS instrument. *Lasers in Medical Science*, 37(4):2269–2277, 2022.

[26] Ruoyang Yao, Xavier Intes, and Qianqian Fang. Direct approach to compute Jacobians for diffuse optical tomography using perturbation Monte Carlo-based photon "replay". *Biomedical Optics Express*, 9(10):4588, 2018.

[27] Ruoyang Yao, Qi Pian, and Xavier Intes. Wide-field fluorescence molecular tomography with compressive sensing based preconditioning. *Biomed. Opt. Express*, 6(12):4887–4898, dec 2015.

[28] Qi Pian, Ruoyang Yao, Lingling Zhao, and Xavier Intes. Hyperspectral time-resolved wide-field fluorescence molecular tomography based on structured light and single-pixel detection. *Optics Letters*, 40(3):431, feb 2015.

[29] Saving Lives at Birth. A Grand Challenge for Development, 2021.

[30] Morris Vanegas, Miguel Mireles, and Qianqian Fang. MOCA: a systematic toolbox for designing and assessing modular functional near-infrared brain imaging probes. *Neurophotonics*, 9(01):1–23, 2022.

[31] John G. Webster, John W. Clark, Michael R. Neuman, Walter H. Olson, Robert A. Peura, Frank P. Primiano, Melvin P. Siedband, and Lawrence A. Wheeler. *Medical instrumentation: Application and design*. John Wiley and Sons, Ltd, 4th edition, 2010.

[32] Lihong V. Wang and Hsin-I Wu. *Biomedical Optics: Principles and Imaging*. John Wiley and Sons, Ltd, 2009.

[33] Ashley J Welch, Martin J C van Gemert, and Willem M Star. Definitions and overview of tissue optics. In *Optical-thermal response of laser-irradiated tissue*, pages 27–64. Springer, 2010.

[34] D. F. Swinehart. The Beer-Lambert law. *Journal of Chemical Education*, 39(7):333–335, 1962.

[35] Miguel Adrián Mireles Núñez. *Hybrid Diffuse Optics For Translational Oncology and Nano-Biophotonics: Towards a Theranostic Approach For Emerging Cancer Therapies*. PhD thesis, Barcelona Institute of Science and Technology, 2018.

[36] Wei Du, Ying Wang, Qingming Luo, and Bi-Feng Liu. Optical molecular imaging for systems biology: from molecule to organism. *Analytical and bioanalytical chemistry*, 386(3):444–457, oct 2006.

[37] Brian W Pogue and Michael S Patterson. Review of tissue simulating phantoms for optical spectroscopy, imaging and dosimetry. *Journal of Biomedical Optics*, 11(4):1–16, jul 2006.

[38] T. Binzoni, T. S. Leung, A. H. Gandjbakhche, D. Rüfenacht, and D. T. Delpy. The use of the Henyey-Greenstein phase function in Monte Carlo simulations in biomedical optics. *Physics in Medicine and Biology*, 51(17), 2006.

[39] Laura A Dempsey, Melissa Persad, Samuel Powell, Danial Chitnis, and Jeremy C Hebden. Geometrically complex 3D-printed phantoms for diffuse optical imaging. *Biomedical optics express*, 8(3):1754–1762, feb 2017.

[40] Jeremy C Hebden, David J Hall, Michael Firbank, and David T Delpy. Time-resolved optical imaging of a solid tissue-equivalent phantom. *Applied Optics*, 34(34):8038–8047, 1995.

[41] Erbao Dong, Zuhua Zhao, Minjie Wang, Yanjun Xie, Shidi Li, Pengfei Shao, Liuquan Cheng, and Ronald X Xu. Three-dimensional fuse deposition modeling of tissue-simulating phantom for biomedical optical imaging. *Journal of Biomedical Optics*, 20(12):1–10, nov 2015.

[42] Camerin Hahn and Sima Noghanian. Heterogeneous Breast Phantom Development for Microwave Imaging Using Regression Models. *International Journal of Biomedical Imaging*, 2012:803607, 2012.

[43] AT Mobashsher and AM Abbosh. Three-Dimensional Human Head Phantom With Realistic Electrical Properties and Anatomy. *IEEE Antennas and Wireless Propagation Letters*, 13:1401–1404, 2014.

[44] Jihoon Park, Yunjin Bae, Youngwoo Bae, Heesung Kang, Kyoung-Joung Lee, and Byungjo Jung. Fabrication of double layer optical tissue phantom by spin coating method: mimicking epidermal and dermal layer. In *Proc.SPIE*, volume 8583, feb 2013.

[45] Akira Ishimaru. Wave Propagation and Scattering in Random Media. IEEE Press, 1997.

[46] S R Arridge and M Schweiger. Image reconstruction in optical tomography. *Philosophical transactions of the Royal Society of London. Series B, Biological sciences*, 352(1354):717–726, jun 1997.

[47] Oliver Dorn. A transport-backtransport method for optical tomography. *Inverse Problems*, 14(5):1107, 1998.

[48] Caigang Zhu and Quan Liu. Review of Monte Carlo modeling of light transport in tissues. *Journal of Biomedical Optics*, 18(5):50902, may 2013.

[49] B C Wilson and G Adam. A Monte Carlo model for the absorption and flux distributions of light in tissue. *Medical physics*, 10(6):824–830, 1983.

[50] Erik Alerstam, Tomas Svensson, and Stefan Andersson-Engels. Parallel computing with graphics processing units for high-speed Monte Carlo simulation of photon migration. *Journal of biomedical optics*, 13(6):60504, 2008.

[51] A P Gibson, J C Hebden, and S R Arridge. Recent advances in diffuse optical imaging. *Physics in Medicine and Biology*, 50(4):R1–R43, 2005.

[52] S R Arridge. Optical tomography in medical imaging. *Inverse Problems*, 15(2):R41–R93, 1999.

[53] Q Fang and D A Boas. Monte Carlo simulation of photon migration in 3D turbid media accelerated by graphics processing units. *Opt Express*, 17(22):20178–20190, 2009.

[54] Qianqian Fang, Stefan A Carp, Juliette J. Selb, Richard H. Moore, Daniel B. Kopans, Eric L. Miller, Dana H. Brooks, and David A. Boas. A multi- modality image reconstruction platform for diffuse optical tomography. In *OSA Biomedical Optics (BIOMED)*, 2008.

[55] Thomas A Neff. Routine Oximetry: A Fifth Vital Sign? *Chest*, 94(2):227, 1988.

[56] Paul Aaron Bohn. *Mobile phone pulse oximeter*. PhD thesis, Northeastern University, 2015.

[57] James E Sinex. Pulse oximetry: Principles and limitations. *The American Journal of Emergency Medicine*, 17(1):59–66, 1999.

[58] Santiago Lopez. Pulse Oximeter Fundamentals and Design. Technical report, Freescale Semiconductor, Inc., 2012.

[59] Edward D. Chan, Michael M. Chan, and Mallory M. Chan. Pulse oximetry: Understanding its basic principles facilitates appreciation of its limitations. *Respiratory Medicine*, 107(6):789–799, 2013.

[60] David A. Boas, Clare E. Elwell, Marco Ferrari, and Gentaro Taga. Twenty years of functional near-infrared spectroscopy: Introduction for the special issue. *NeuroImage*, 85(1):1–5, 2014.

[61] Marco Ferrari and Valentina Quaresima. A brief review on the history of human functional near-infrared spectroscopy (fNIRS) development and fields of application. *NeuroImage*, 63(2):921–935, 2012.

[62] Felix Scholkmann, Stefan Kleiser, Andreas Jaakko Metz, Raphael Zimmermann, Juan Mata Pavia, Ursula Wolf, and Martin Wolf. A review on continuous wave functional near-infrared spectroscopy and imaging instrumentation and methodology. *NeuroImage*, 85:6–27, 2014.

[63] Paola Pinti, Ilias Tachtsidis, Antonia Hamilton, Joy Hirsch, Clarisse Aichelburg, Sam Gilbert, and Paul W Burgess. The present and future use of functional near-infrared spectroscopy (fNIRS) for cognitive neuroscience. *Annals of the New York Academy of Sciences*, 1464(1):5–29, mar 2020.

[64] S C Bunce, M Izzetoglu, K Izzetoglu, B Onaral, and K Pourrezaei. Functional near-infrared spectroscopy. *IEEE Engineering in Medicine and Biology Magazine*, 25(4):54–62, 2006.

[65] M Izzetoglu, S C Bunce, K Izzetoglu, B Onaral, and a. K Pourrezaei. Functional brain imaging using near-infrared technology. *IEEE Engineering in Medicine and Biology Magazine*, 26(4):38–46, 2007.

[66] D T Delpy, M Cope, P van der Zee, S Arridge, Susan Wray, and J Wyatt. Estimation of optical pathlength through tissue from direct time of flight measurement. *Physics in Medicine and Biology*, 33(12):1433–42, 1988.

[67] Stéphane Perrey. Non-invasive NIR spectroscopy of human brain function during exercise. *Methods*, 45(4):289–299, 2008.

[68] J P Culver, V Ntziachristos, M J Holboke, and a G Yodh. Optimization of optode arrangements for diffuse optical tomography: A singular-value analysis. *Optics letters*, 26(10):701–703, 2001.

[69] Per Christian Hansen. *Rank-Deficient and Discrete Ill-Posed Problems*. Society for Industrial and Applied Mathematics, Philadelphia, PA, 1998.

[70] Hamid Dehghani, Subhadra Sri Nivasan, Brian W. Pogue, and Adam Gibson. Numerical modelling and image reconstruction in diffuse optical tomography. *Philosophical Transactions of the Royal Society A: Mathematical, Physical and Engineering Sciences*, 367(1900):3073–3093, 2009.

[71] Bin Deng, Dana H. Brooks, David A. Boas, Mats Lundqvist, and Qianqian Fang. Characterization of structural-prior guided optical tomography using realistic breast models derived from dual-energy x-ray mammography. *Biomedical Optics Express*, 6(7):2366–2379, 2015.

[72] Jason Geng. Structured-light 3D surface imaging: a tutorial. *Advances in Optics and Photonics*, 3(2):128, 2011.

[73] Daniel Moreno and Gabriel Taubin. Simple, accurate, and robust projector-camera calibration. In *Proceedings - 2nd Joint 3DIM/3DPVT Conference: 3D Imaging, Modeling, Processing, Visualization and Transmission*, pages 464–471. IEEE, 2012.

[74] World health organization. Neonatal and perinatal mortality. *World Health Organisation*, 99:1–75, 2006.

[75] Monica Alexander and Leontine Alkema. Global estimation of neonatal mortality using a Bayesian hierarchical splines regression model. *Demographic Research*, 38(1):335–372, 2018.

[76] Martin W. Weber, John B. Carlin, Salvacion Gatchalian, Deborah Lehmann, Lulu Muhe, and E. Kim Mulholland. Predictors of neonatal sepsis in developing countries. *Pediatric Infectious Disease Journal*, 22(8):711–716, 2003.

[77] A F Ouro-Bang'na Maman, K Tomta, S Ahouangbévi, and M Chobli. Deaths associated with anaesthesia in Togo, West Africa. *Tropical Doctor*, 35(4):220–222, oct 2005.

[78] A J Heywood, I H Wilson, and J R Sinclair. Perioperative mortality in Zambia. *Annals of the Royal College of Surgeons of England*, 71:354–358, 1989.

[79] Young-Jin Jung, Manuela Roman, Jennifer Carrasquilla, Sarah J Erickson, and Anuradha Godavarty. Portable Wide-Field Hand-Held NIR Scanner. *Proceedings of SPIE*, 8572(i):1–9, 2013.

[80] W Karlen, G Dumont, C Petersen, J Gow, J Lim, J Sleiman, and J M Ansermino. Human-Centered Phone Oximeter Interface Design For The Operating Room: Pulse Oximeter Interfaced to a Mobile Device for Anesthesia Monitoring in the Developing World. In *Healthinf 2011: Proceedings of the International Conference on Health Informatics*, number July in 1, pages 433–438, 2011.

[81] J. Hudson, S. M. Nguku, J. Sleiman, W. Karlen, G. A. Dumont, C. L. Petersen, C. B. Warriner, and J. M. Ansermino. Usability testing of a prototype phone Oximeter with healthcare providers in high- and low-medical resource environments. *Anaesthesia*, 67(9):957–967, 2012.

[82] Robert A. Malkin. Barriers for medical devices for the developing world. *Expert Review of Medical Devices*, 4(6):759–763, 2007.

[83] Jacob Poushter. Smartphone Ownership and Internet Usage Continues to Climb in Emerging Economies. *Pew Research Center*, pages 1–45, 2016.

[84] Joseph Bailey, Michael Fecteau, and Noah L. Pendleton. Wireless Pulse Oximeter. *The Degree of Bachelor of Science*, page 80, 2008.

[85] Elmar Laistler, Barbara Dymerska, Jürgen Sieg, Sigrun Goluch, Roberta Frass-Kriegl, Andre Kuehne, and Ewald Moser. In vivo MRI of the human finger at 7 T. *Magnetic resonance in medicine*, 79(1):588–592, jan 2018.

[86] Steven Jacques, Ting Li, and Scott Prahl. MCXYZ.c, 2013.

[87] Sanathana Konugolu Venkata Sekar, Marco Pagliazzi, Eugènia Negredo, Fabrizio Martelli, Andrea Farina, Alberto Dalla Mora, Claus Lindner, Parisa Farzam, Núria Pérez-Álvarez, Jordi Puig, Paola Taroni, Antonio Pifferi, and Turgut Durduran. In Vivo, Non-Invasive Characterization of Human Bone by Hybrid Broadband (600-1200 nm) Diffuse Optical and Correlation Spectroscopies. *PloS one*, 11(12):e0168426–e0168426, dec 2016.

[88] S A Prahl. A compendium of tissue optical properties, 2012.

[89] George M Hale and Marvin R Querry. Optical Constants of Water in the 200-nm to 200-μm Wavelength Region. *Applied Optics*, 12(3):555–563, 1973.

[90] R L P van Veen, H.J.C.M. Sterenborg, A Pifferi, A Torricelli, and R Cubeddu. Determination of VIS- NIR absorption coefficients of mammalian fat, with time- and spatially resolved diffuse reflectance and transmission spectroscopy. In *Biomedical Topical Meeting*, OSA Technical Digest, page SF4, Miami Beach, Florida, 2004. Optical Society of America.

[91] Steven L Jacques and Daniel J McAuliffe. The Melanosome: Threshold Temperature For Explosive Vaporization and Internal Absorption Coefficient During Pulsed Laser Irradiation. *Photochemistry and Photobiology*, 53(6):769–775, jun 1991.

[92] Steven L Jacques. Optical properties of biological tissues: a review. *Physics in Medicine and Biology*, 58(11):R37–R61, 2013.

[93] Alrick B Hertzman. The blood supply of various skin areas as estimated by the photoelectric plethysmograph. *American Journal of Physiology-Legacy Content*, 124(2):328–340, 1938.

[94] Mohamed Elgendi. On the analysis of fingertip photoplethysmogram signals. *Current cardiology reviews*, 8(1):14–25, feb 2012.

[95] Sebastian Heinzel, Florian B. Haeussinger, Tim Hahn, Ann Christine Ehlis, Michael M. Plichta, and Andreas J. Fallgatter. Variability of (functional) hemodynamics as measured with simultaneous fNIRS and fMRI during intertemporal choice. *NeuroImage*, 71:125–134, 2013.

[96] Nicole M. McDonald and Katherine L. Perdue. The infant brain in the social world: Moving toward interactive social neuroscience with functional near-infrared spectroscopy. *Neuroscience and Biobehavioral Reviews*, 87(December 2017):38–49, 2018.

[97] Richard N. Aslin, Mohinish Shukla, and Lauren L. Emberson. Hemodynamic Correlates of Cognition in Human Infants. *Annual Review of Psychology*, 66(1):349–379, 2015.

[98] Ross E. Vanderwert and Charles A. Nelson. The use of near-infrared spectroscopy in the study of typical and atypical development. *NeuroImage*, 85:264–271, 2014.

[99] Teresa Wilcox and Marisa Biondi. fNIRS in the developmental sciences. *Wiley Interdisciplinary Reviews: Cognitive Science*, 6(3):263–283, 2015.

[100] Mojtaba Soltanlou, Maria A. Sitnikova, Hans Christoph Nuerk, and Thomas Dresler. Applications of functional near-infrared spectroscopy (fNIRS) in studying cognitive development: The case of mathematics and language. *Frontiers in Psychology*, 9(APR), 2018.

[101] Valentina Quaresima, Silvia Bisconti, and Marco Ferrari. A brief review on the use of functional near-infrared spectroscopy (fNIRS) for language imaging studies in human newborns and adults. *Brain and Language*, 121(2):79–89, 2012.

[102] Sonja Rossi, Silke Telkemeyer, Isabell Wartenburger, and Hellmuth Obrig. Shedding light on words and sentences: Near-infrared spectroscopy in language research. *Brain and Language*, 121(2):152–163, 2012.

[103] Ann-Christine Ehlis, Sabrina Schneider, Thomas Dresler, and Andreas J Fallgatter. Application of functional near-infrared spectroscopy in psychiatry. *NeuroImage*, 85:478–88, 2014.

[104] Vijay Kumar, Venkataram Shivakumar, Harleen Chhabra, Anushree Bose, Ganesan Venkatasubramanian, and Bangalore N. Gangadhar. Functional near infra-red spectroscopy (fNIRS) in schizophrenia: A review. *Asian Journal of Psychiatry*, 27(2017):18–31, 2017.

[105] Muyue Yang, Zhen Yang, Tifei Yuan, Wuwei Feng, and Pu Wang. A systemic review of functional near-infrared spectroscopy for stroke: Current application and future directions. *Frontiers in Neurology*, 10(FEB):1–14, 2019.

[106] Noman Naseer and Keum Shik Hong. fNIRS-based brain-computer interfaces: A review. *Frontiers in Human Neuroscience*, 9(JAN):1–15, 2015.

[107] Sangtae Ahn and Sung C. Jun. Multi-modal integration of EEG-fNIRS for brain-computer interfaces – Current limitations and future directions. *Frontiers in Human Neuroscience*, 11(October):1–6, 2017.

[108] Keum Shik Hong, M. Jawad Khan, and Melissa J. Hong. Feature Extraction and Classification Methods for Hybrid fNIRS-EEG Brain-Computer Interfaces. *Frontiers in Human Neuroscience*, 12(June):1–25, 2018.

[109] Valentina Quaresima and Marco Ferrari. A mini-review on functional near-infrared spectroscopy (fNIRS): Where do we stand, and where should we go? *Photonics*, 6(3):87, 2019.

[110] Adam T. Eggebrecht, Silvina L. Ferradal, Amy Robichaux-Viehoever, Mahlega S. Hassanpour, Hamid Dehghani, Abraham Z. Snyder1, Tamara Hershey, and Joseph P. Culver. Mapping distributed brain function and networks with diffuse optical tomography. *Nature Photonics*, 8(6):448–454, 2014.

[111] Muriah D. Wheelock, Joseph P. Culver, and Adam T. Eggebrecht. High-density diffuse optical tomography for imaging human brain function. *Review of Scientific Instruments*, 90(5):1–24, 2019.

[112] Artinis. OxyMon Cart fNIRS System, 2017.

[113] TechEn. NIRSOptix CW6 System, 2018.

[114] Hubin Zhao and Robert J. Cooper. Review of recent progress toward a fiberless, whole-scalp diffuse optical tomography system. *Neurophotonics*, 5(01):1, 2017.

[115] Adrian Curtin and Hasan Ayaz. The Age of Neuroergonomics: Towards Ubiquitous and Continuous Measurement of Brain Function with fNIRS. *Japanese Psychological Research*, 60(4):374–386, 2018.

[116] Nicholas M. Gregg, Brian R. White, Benjamin W. Zeff, Andrew J. Berger, and Joseph P. Culver. Brain specificity of diffuse optical imaging: improvements from superficial signal regression and tomography. *Frontiers in Neuroenergetics*, 2(July):1–8, 2010.

[117] A Maki, Y Yamashita, Y Ito, E Watanabe, Y Mayanagi, and H Koizumi. Spatial and temporal analysis of human motor activity using noninvasive NIR topography. *Medical physics*, 22(12):1997–2005, dec 1995.

[118] Daniel Chitnis, Robert J. Cooper, Laura Dempsey, Samuel Powerll, Simone Quaggia, David Highton, Clare Elwell, Jeremy C. Hebden, and Nicholas L. Everdell. Functional imaging of the human brain using a modular , fibre-less , high-density diffuse optical tomography system. *Biomedical optics express*, 7(10):4275–4288, 2016.

[119] Alexander von Luhmann, Heidrun Wabnitz, Tilmann Sander, and Klaus-Robert Müller. M3BA : A Mobile , Modular , Multimodal Biosignal Acquisition Architecture for Miniaturized EEG-NIRS-Based Hybrid BCI and Monitoring. *IEEE Transactions on Biomedical Engineering*, 64(6):1199–1210, 2017.

[120] R Zimmermann, F Braun, T Achtnich, Olivier Lambercy, Roger Gassert, and M Wolf. Silicon photomultipliers for improved detection of low light levels in miniature near-infrared spectroscopy instruments. *Biomedical optics express*, 4(5):659–666, 2013.

[121] Tsukasa Funane, Takashi Numata, Hiroki Sato, Shinsuke Hiraizumi, Yuichi Hasegawa, Hidenobu Kuwabara, Kiyoshi Hasegawa, and Masashi Kiguchi. Rearrangeable and exchangeable optical module with system-on-chip for wearable functional near-infrared spectroscopy system. *Neurophotonics*, 5(01):1, 2017.

[122] Hubin Zhao, Sabrina Brigadoi, Reuben Hill, Greg Smith, Luke Dunne, Elisabetta Maria Frijia, Samuel Powell, Nick L. Everdell, and Robert Cooper. Advances in wearable high-density diffuse optical tomography: first applications of a new commercial technology and development of an infant-specific research device. In *Clinical and Preclinical Optical Diagnostics II*, page 110742. Optica Publishing Group, 2019.

[123] Hubin Zhao, Elisabetta M Frijia, Vidal Rosas, Liam Collins-jones, Greg Smith, Reuben Nixon-hill, Samuel Powell, Nicholas L Everdell, and Robert J Cooper. Design and validation of a mechanically flexible and ultra-lightweight high-density diffuse optical tomography system for functional neuroimaging of newborns. *Neurophotonics*, 8(1):1–18, 2021.

[124] Theodore J Huppert, Solomon G Diamond, Maria Angela Franceschini, and David A Boas. HomER: a review of time-series analysis methods for near-infrared spectroscopy of the brain. *Applied optics*, 48(10):280–298, 2009.

[125] Hendrik Santosa, Xuetong Zhai, Frank Fishburn, and Theodore Huppert. The NIRS Brain AnalyzIR toolbox. *Algorithms*, 11(5), 2018.

[126] Samuel Montero Hernandez and Luca Pollonini. NIRSplot: A tool for quality assessment of fNIRS scans. In *Biophotonics Congress: Biomedical Optics*, 2020.

[127] Sabrina Brigadoi, Domenico Salvagnin, Matteo Fischetti, and Robert J. Cooper. Array Designer: automated optimized array design for functional near-infrared spectroscopy. *Neurophotonics*, 5(03):1, 2018.

[128] A. Machado, Z. Cai, G. Pellegrino, O. Marcotte, T. Vincent, J. M. Lina, E. Kobayashi, and C. Grova. Optimal positioning of optodes on the scalp for personalized functional near-infrared spectroscopy investigations. *Journal of Neuroscience Methods*, 309(November 2017):91–108, 2018.

[129] Guilherme Augusto Zimeo Morais, Joana Bisol Balardin, and João Ricardo Sato. FNIRS Optodes' Location Decider (fOLD): A toolbox for probe arrangement guided by brain regions-of-interest. *Scientific Reports*, 8(1):1–11, 2018.

[130] Christopher M. Aasted, Meryem A. Yücel, Robert J. Cooper, Jay Dubb, Daisuke Tsuzuki, Lino Becerra, Mike P. Petkov, David Borsook, Ippeita Dan, and David A. Boas. Anatomical guidance for functional near-infrared spectroscopy: AtlasViewer tutorial. *Neurophotonics*, 2(2):020801, 2015.

[131] Morris D. Vanegas and Qianqian Fang. Modular Optode Configuration Analyzer. `github.com/COTILab/MOCA`, 2020.

[132] Dominik Wyser, Olivier Lambercy, Felix Scholkmann, Martin Wolf, and Roger Gassert. Wearable and modular functional near-infrared spectroscopy instrument with multidistance measurements at four wavelengths. *Neurophotonics*, 4(4), 2017.

[133] Thomas Muehlemann, Daniel Haensse, and Martin Wolf. Wireless miniaturized in-vivo near infrared imaging. *Optics Express*, 16(14):10323, 2008.

[134] Bertan Hallacoglu, Jason W. Trobaugh, Kate L. Bechtel, and Chandran V. Seshagiri. Blood phantom verification of a new compact DOT system. In *Biomedical Optics Congress 2016*, 2016.

[135] Tomoyuki Hiroyasu, Tomoya Yoshida, and Utako Yamamoto. Investigation of regions of interest (ROI) through the selection of optimized channels in fNIRS data. In *2015 IEEE Congress on Evolutionary Computation (CEC)*, pages 764–768. IEEE, 2015.

[136] Qianqian Fang and David A. Boas. Tetrahedral mesh generation from volumetric binary and grayscale images. In *Proceedings - 2009 IEEE International Symposium on Biomedical Imaging: From Nano to Macro, ISBI 2009*, pages 1142–1145, 2009.

[137] Michael Jermyn, Hamid Ghadyani, Michael A. Mastanduno, Wes Turner, Scott C. Davis, Hamid Dehghani, and Brian W. Pogue. Fast segmentation and high-quality three-dimensional volume mesh creation from medical images for diffuse optical tomography. *Journal of Biomedical Optics*, 18(8):1–11, 2013.

[138] Mateo Calderon-Arnulphi, Ali Alaraj, and Konstantin V Slavin. Near infrared technology in neuroscience: past, present and future. *Neurological research*, 31(6):605–614, 2009.

[139] Gentaro Taga, Fumitaka Homae, and Hama Watanabe. Effects of source-detector distance of near infrared spectroscopy on the measurement of the cortical hemodynamic response in infants. *Neuroimage*, 38(3):452–460, 2007.

[140] Sarah Lloyd-Fox, Anna Blasi, and C E Elwell. Illuminating the developing brain: the past, present and future of functional near infrared spectroscopy. *Neuroscience and Biobehavioral Reviews*, 34(3):269–284, 2010.

[141] Andrew Winslow. An Optimal Algorithm for Tiling the Plane with a Translated Polyomino. In Khaled Elbassioni and Kazuhisa Makino, editors, *Algorithms and Computation*, pages 3–13, Berlin, Heidelberg, 2015. Springer Berlin Heidelberg.

[142] Hanan Samet. *The Design and Analysis of Spatial Data Structures*, volume 85. Addison-Wesley, Reading, MA, 1990.

[143] Takahiko Kamae. A systematic method of finding all directed circuits and enumerating all directed paths. *IEEE Transactions on Circuit Theory*, 14(2):166–171, 1967.

[144] Gary E. Strangman, Zhi Li, and Quan Zhang. Depth Sensitivity and Source-Detector Separations for Near Infrared Spectroscopy Based on the Colin27 Brain Template. *PLoS ONE*, 8(8), 2013.

[145] Sabrina Brigadoi and Robert J. Cooper. How short is short? Optimum source–detector distance for short-separation channels in functional near-infrared spectroscopy. *Neurophotonics*, 2(2):025005, 2015.

[146] Qianqian Fang, Stefan A Carp, Juliette Selb, Greg Boverman, Quan Zhang, B Daniel, Richard H Moore, Eric L Miller, Dana H Brooks, and David A Boas. Combined Optical Imaging and Mammography of the Healthy Breast: Optical Contrast Derived From Breast Structure and Compression. *IEEE Transactions on Medical Imaging*, 28(1):30–42, 2009.

[147] Qianqian Fang. Mesh-based Monte Carlo method using fast ray-tracing in Plücker coordinates. *Biomed. Opt. Express*, 1(1):165–175, aug 2010.

[148] Anh Phong Tran, Shijie Yan, and Qianqian Fang. Improving model-based functional near-infrared spectroscopy analysis using mesh-based anatomical and light-transport models. *Neurophotonics*, 7(1):1–18, 2020.

[149] Eiji Okada and David T. Delpy. Near-infrared light propagation in an adult head model II Effect of superficial tissue thickness on the sensitivity of the near-infrared spectroscopy signal. *Applied Optics*, 42(16):2915, 2003.

[150] Carmen E. Sanchez, John E. Richards, and C. Robert Almli. Age-specific MRI templates for pediatric neuroimaging. *Developmental Neuropsychology*, 37(5):379–399, 2012.

[151] John T. McConville, Charles E. Clauser, Thomas D. Churchill, Jaime Cuzzi, and Ints Kaleps. Aerospace Medical Report: Anthropometric Relationships of Body and Body Segment Moments of Inertia. Technical report, Johnson Space Center, 1980.

[152] Gowerlabs. Gowerlabs, 2019.

[153] Parikshat Sirpal, Ali Kassab, Philippe Pouliot, and Dang Khoa Nguyen. fNIRS improves seizure detection in multimodal EEG-fNIRS recordings. *Journal of Biomedical Optics*, 24(05):1, 2019.

[154] Eric S. Jackson, Sobana Wijeakumar, Deryk S. Beal, Bryan Brown, Patricia Zebrowski, and John P. Spencer. A fNIRS Investigation of Speech Planning and Execution in Adults Who Stutter. *Neuroscience*, 406:73–85, 2019.

[155] Guilherme Brockington, Joana Bisol Balardin, Guilherme Augusto Zimeo Morais, Amanda Malheiros, Roberto Lent, Luciana Monteiro Moura, and Joao R. Sato. From the laboratory to the classroom: The potential of functional near-infrared spectroscopy in educational neuroscience. *Frontiers in Psychology*, 9(OCT):1–7, 2018.

[156] Daniel Lopez-Martinez, Ke Peng, Arielle Lee, David Borsook, and Rosalind Picard. Pain Detection with fNIRS-Measured Brain Signals: A Personalized Machine Learning Approach Using the Wavelet Transform and Bayesian Hierarchical Modeling with Dirichlet Process Priors. In *2019 8th International Conference on Affective Computing and Intelligent Interaction Workshops and Demos, ACIIW 2019*, pages 304–309, 2019.

[157] N. L. Everdell, A. P. Gibson, I. D.C. Tullis, T. Vaithianathan, J. C. Hebden, and D. T. Delpy. A frequency multiplexed near-infrared topography system for imaging functional activation in the brain. *Review of Scientific Instruments*, 76(9):1–6, 2005.

[158] Manob Jyoti Saikia, Walter G. Besio, and Kunal Mankodiya. WearLight: Toward a Wearable, Configurable Functional NIR Spectroscopy System for Noninvasive Neuroimaging. *IEEE Transactions on Biomedical Circuits and Systems*, 13(1):91–102, 2019.

[159] Paola Pinti, Clarisse Aichelburg, Sam Gilbert, Antonia Hamilton, Joy Hirsch, Paul Burgess, and Ilias Tachtsidis. A Review on the Use of Wearable Functional Near-Infrared Spectroscopy in Naturalistic Environments. *Japanese Psychological Research*, 60(4):347–373, 2018.

[160] Nathan W Moon, Paul MA Baker, and Kenneth Goughnour. Designing wearable technologies for users with disabilities: Accessibility, usability, and connectivity factors. *Journal of Rehabilitation and Assistive Technologies Engineering*, 6:205566831986213, 2019.

[161] Hasan Ayaz, Wesley B. Baker, Giles Blaney, David A. Boas, Heather Bortfeld, Kenneth Brady, Joshua Brake, Sabrina Brigadoi, Erin M. Buckley, Stefan A. Carp, Robert J. Cooper, Kyle R. Cowdrick, Joseph P. Culver, Ippeita Dan, Hamid Dehghani, Anna Devor, Turgut Durduran, Adam T. Eggebrecht, Lauren L. Emberson, Qianqian Fang, Sergio Fantini, Maria Angela Franceschini, Jonas B. Fischer, Judit Gervain, Joy Hirsch, Keum-Shik Hong, Roarke Horstmeyer, Jana M. Kainerstorfer, Tiffany S. Ko, Daniel J. Licht, Adam Liebert, Robert Luke, Jennifer M. Lynch, Jaume Mesquida, Rickson C. Mesquita, Noman Naseer, Sergio L. Novi, Felipe Orihuela-Espina, Thomas D. O'Sullivan, Darcy S. Peterka, Antonio Pifferi, Luca Pollonini, Angelo Sassaroli, João Ricardo Sato, Felix Scholkmann, Lorenzo Spinelli, Vivek J. Srinivasan, Keith St. Lawrence, Ilias Tachtsidis, Yunjie Tong, Alessandro Torricelli, Tara Urner, Heidrun Wabnitz, Martin Wolf, Ursula Wolf, Shiqi Xu, Changhuei Yang, Arjun G. Yodh, Meryem A. Yücel, and Wenjun Zhou. Optical imaging and spectroscopy for the study of the human brain: status report. *Neurophotonics*, 9(S2):1–65, 2022.

[162] Stéphane Perrey. Possibilities for examining the neural control of gait in humans with fNIRS. *Frontiers in Physiology*, 5(May):10–13, 2014.

[163] Christian H Bartkowski, Jessica Gemignani, Randall L Barbour, Klaus-dieter Lang, Von Krshiwoblozki, René Vieroth, Christian Dils, Erik Jung, and Christoph H Schmitz. Variable Source Emitter Smart Textile Headgear Design for Functional Near Infrared Spectroscopy. In *IEEE Engineering in Medicine and Biology*, number July in 1, 2019.

[164] K Alper, Yun Miao, and Valencia Koomson. Design of a miniaturized frequency domain near infrared spectroscopy instrument with validation in solid phantoms and human tissue. *Journal of Near Infrared Spectroscopy*, 0(0):1–11, 2022.

[165] Ilaria Mazzonetto, Marco Castellaro, Robert J. Cooper, and Sabrina Brigadoi. Smartphone-based photogrammetry provides improved localization and registration of scalp-mounted neuroimaging sensors. *Scientific Reports*, 12(1):1–14, 2022.

[166] SNIRF. Shared Near Infrared Format, 2021.

[167] Morris D. Vanegas. Modular Optical Brain Imager Demo. MorrisVanegas.com/MOBIdemo/, 2020.

[168] Christian Kothe. Lab Streaming Layer (LSL).

[169] Rebecca L. Siegel, Kimberly D. Miller, Hannah E. Fuchs, and Ahmedin Jemal. Cancer statistics, 2022. *CA: A Cancer Journal for Clinicians*, 72(1):7–33, 2022.

[170] Laszlo Tabar, Ming Fang Yen, Bedrich Vitak, Hsiu Hsi Tony Chen, Robert A. Smith, and Stephen W. Duffy. Mammography service screening and mortality in breast cancer patients: 20-year follow-up before and after introduction of screening. *Lancet*, 361(9367):1405–1410, 2003.

[171] Joann G. Elmore, Mary B. Barton, Victoria M. Moceri, Sarah Polk, Philip J. Arena, and Suzanne W. Fletcher. Ten-year risk of false positive screening mammograms and clinical breast examinations. *New England Journal of Medicine*, 338(16):1089–1096, 1998.

[172] Daniel Richard Leff, Oliver J. Warren, Louise C. Enfield, Adam Gibson, Thanos Athanasiou, Darren K. Patten, Jem Hebden, Guang Zhong Yang, and Ara Darzi. Diffuse optical imaging of the healthy and diseased breast: A systematic review. *Breast Cancer Research and Treatment*, 108(1):9–22, 2008.

[173] Yukio Yamada and Shinpei Okawa. Diffuse optical tomography: Present status and its future. *Optical Review*, 21(3):185–205, 2014.

[174] Yihan Wang, Songpeng Li, Yirong Wang, Qiang Yan, Xin Wang, Yudong Shen, Zhiqiang Li, Fei Kang, Xu Cao, and Shouping Zhu. Compact fiber-free parallel-plane multi-wavelength diffuse optical tomography system for breast imaging. *Optics Express*, 30(5):6469, 2022.

[175] Hamed Vavadi, Chen Xu, Atahar Mostafa, and Quing Zhu. Automated data selection method for diffuse optical tomography to improve the robustness of breast cancer detection. *Optics InfoBase Conference Papers*, 7(10):387–397, 2014.

[176] Molly L. Flexman, Hyun K. Kim, Jacqueline E. Gunther, Emerson A. Lim, Maria C. Alvarez, Elise Desperito, Kevin Kalinsky, Dawn L. Hershman, and Andreas H. Hielscher. Optical biomarkers for breast cancer derived from dynamic diffuse optical tomography. *Journal of Biomedical Optics*, 18(9):096012, 2013.

[177] Regine Choe, Soren D Konecky, Alper Corlu, Kijoon Lee, Turgut Durduran, David R Busch, Saurav Pathak, Brian J Czerniecki, Julia Tchou, Douglas L Fraker, Angela Demichele, Britton Chance, Simon R Arridge, Martin Schweiger, Joseph P Culver, Mitchell D Schnall, Mary E Putt, Mark A Rosen, and Arjun G Yodh. Differentiation of benign and malignant breast tumors by in-vivo three-dimensional parallel-plate diffuse optical tomography. *Journal of biomedical optics*, 14(2):24020, 2009.

[178] Paola Taroni, Alessandro Torricelli, Lorenzo Spinelli, Antonio Pifferi, Francesco Arpaia, Gianmaria Danesini, and Rinaldo Cubeddu. Time-resolved optical mammography between 637 and 985 nm: Clinical study on the detection and identification of breast lesions. *Physics in Medicine and Biology*, 50(11):2469–2488, 2005.

[179] Ang Li, Jing Liu, Wendy Tanamai, Richard Kwong, Albert E Cerussi, and J Bruce. Assessing the spatial extent of breast tumor intrinsic optical contrast using ultrasound and diffuse optical spectroscopy. *Journal of Biomedical Optics*, 13(3):1–8, 2010.

[180] Bernhard B. Zimmermann, Bin Deng, Bhawana Singh, Mark Martino, Juliette Selb, Qianqian Fang, Amir Y. Sajjadi, Jayne Cormier, Richard H. Moore, Daniel B. Kopans, David A. Boas, Mansi A. Saksena, and Stefan A. Carp. Multimodal breast cancer imaging using coregistered dynamic diffuse optical tomography and digital breast tomosynthesis. *Journal of Biomedical Optics*, 22(4):046008, 2017.

[181] Bin Deng, Maxim Fradkin, Jean-Michel Rouet, Richard H. Moore, Daniel B. Kopans, David A. Boas, Mats Lundqvist, and Qianqian Fang. Characterizing breast lesions through robust multimodal data fusion using independent diffuse optical and x-ray breast imaging. *Journal of Biomedical Optics*, 20(8):080502, 2015.

[182] J. P. Culver, R. Choe, M. J. Holboke, L. Zubkov, T. Durduran, A. Slemp, V. Ntziachristos, B. Chance, and A. G. Yodh. Three-dimensional diffuse optical tomography in the parallel plane transmission geometry: Evaluation of a hybrid frequency domain/continuous wave clinical system for breast imaging. *Medical Physics*, 30(2):235–247, 2003.

[183] Quing Zhu and Steven Poplack. A review of optical breast imaging: Multi-modality systems for breast cancer diagnosis. *European Journal of Radiology*, 129:109067, 2020.

[184] Venkataramanan Krishnaswamy, Kelly E. Michaelsen, Brian W. Pogue, Steven P. Poplack, Ian Shaw, Ken Defrietas, Ken Brooks, and Keith D. Paulsen. A digital x-ray tomosynthesis coupled near infrared spectral tomography system for dual-modality breast imaging. *Optics Express*, 20(17):19125, 2012.

[185] Fadi El-Ghussein, Michael A Mastanduno, Shudong Jiang, Brian W Pogue, and Keith D Paulsen. Hybrid photomultiplier tube and photodiode parallel detection array for wideband optical spectroscopy of the breast guided by magnetic resonance imaging. *Journal of Biomedical Optics*, 19(1):11010, aug 2013.

[186] Vasilis Ntziachristos, A G Yodh, Mitchell D Schnall, and Britton Chance. MRI-Guided Diffuse Optical Spectroscopy of Malignant and Benign Breast Lesions. *Neoplasia*, 4(4):347–354, 2002.

[187] Quing Zhu, Poornima U Hegde, Andrew Ricci, Mark Kane, Edward B Cronin, Yasaman Ardeshirpour, Chen Xu, Andres Aguirre, Scott H Kurtzman, Peter J Deckers, and Susan H Tannenbaum. Early-Stage Invasive Breast Cancers: Potential Role of Optical Tomography with US Localization in Assisting Diagnosis. *Radiology*, 256(2):367–378, aug 2010.

[188] Alejandro Rodríguez-Ruiz, Greeshma A. Agasthya, and Ioannis Sechopoulos. The compressed breast during mammography and breast tomosynthesis: In vivo shape characterization and modeling. *Physics in Medicine and Biology*, 62(17):6920–6937, 2017.

[189] Matthew J. Pallone, Steven P. Poplack, Hima Bindu R. Avutu, Keith D. Paulsen, and Richard J. Barth. Supine breast MRI and 3D optical scanning: A novel approach to improve tumor localization for breast conserving surgery. *Annals of Surgical Oncology*, 21(7):2203–2208, 2014.

[190] C. Gallego Ortiz and A. L. Martel. Automatic atlas-based segmentation of the breast in MRI for 3D breast volume computation. *Medical Physics*, 39(10):5835–5848, 2012.

[191] Qianqian Fang, Juliette Selb, Stefan A Carp, Gregory Boverman, Eric L Miller, Dana H Brooks, Richard H Moore, Daniel B Kopans, and David A Boas. Combined Optical and X-ray Tomosynthesis Breast Imaging. *Radiology*, 258(1):89–97, jan 2011.

[192] Ben Brooksby, Brian W. Pogue, Shudong Jiang, Hamid Dehghani, Subhadra Srinivasan, Christine Kogel, Tor D. Tosteson, John Weaver, Steven P. Poplack, and Keith D. Paulsen. Imaging breast adipose and fibroglandular tissue molecular signatures by using hybrid MRI-guided near-infrared spectral tomography. *Proceedings of the National Academy of Sciences of the United States of America*, 103(23):8828–8833, 2006.

[193] Julia Krüger, Jan Ehrhardt, Arpad Bischof, and Heinz Handels. Breast compression simulation using ICP-based B-spline deformation for correspondence analysis in mammography and MRI datasets. *Medical Imaging 2013: Image Processing*, 8669(March 2013):86691D, 2013.

[194] Carl L Kalbhen, John J Mcgill, Paul M Fendley, Kevin W Corrigan, and Juan Angelats. Mammographic Determination of Breast Volume: Comparing Different Methods. *American Journal of Roentgenology*, 173(6):1643–1649, 1999.

[195] Yasuyo Kita, Ralph Highnam, and Michael Brady. Correspondence between different view breast x-rays using a simulation of breast deformation. *Proceedings of the IEEE Computer Society Conference on Computer Vision and Pattern Recognition*, pages 700–707, 1998.

[196] Jessica B. Chang, Kevin H. Small, Mihye Choi, and Nolan S. Karp. Three-Dimensional Surface Imaging in Plastic Surgery: Foundation, Practical Applications, and beyond. *Plastic and Reconstructive Surgery*, 135(5):1295–1304, 2015.

[197] Albert Losken, Hisham Seify, Donald D. Denson, Alfredo A. Jr Paredes, and Grant W. Carlson. Validating Three-Dimensional Imaging of the Breast. *Annals of Plastic Surg*, 54(5):471–476, 2005.

[198] Jiqiao Yang, Run Zhang, Jiani Shen, Yuanyuan Hu, and Qing Lv. The Three-Dimensional Techniques in the Objective Measurement of Breast Aesthetics. *Aesthetic Plastic Surgery*, 39(6):910–915, 2015.

[199] Xiangyang Ju, Helga Henseler, Matthew Jian qiao Peng, Balvinder S. Khambay, Arup K. Ray, and Ashraf F. Ayoub. Multi-view stereophotogrammetry for post-mastectomy breast reconstruction. *Medical and Biological Engineering and Computing*, 54(2-3):475–484, 2016.

[200] Greg M. Galdino, Maurice Nahabedian, Michael Chiaramonte, Jason Z. Geng, Stanley Klatsky, and Paul Manson. Clinical applications of three-dimensional photography in breast surgery. *Plastic and Reconstructive Surgery*, 110(1):58–70, 2002.

[201] Qianqian Fang. Quantitative diffuse optical tomography using a mobile phone camera and automatic 3D photo stitching. In *Biomedical Optics and 3-D Imaging*, page BSu3A.96. Optica Publishing Group, 2012.

[202] Helga Henseler, J Smith, A Bowman, BS Khambay, Xiangyang Ju, Ashraf F. Ayoub, and Arup K. Ray. Investigation into variation and errors of a three-dimensional breast imaging system using multiple stereo cameras. *Journal of Plastic, Reconstructive and Aesthetic Surgery*, 65(12), 2012.

[203] Helga Henseler, BS Khambay, A Bowman, J Smith, J Paul Siebert, S Oehler, X Ju, A Ayoub, and AK Ray. Investigation into accuracy and reproducibility of a 3D breast imaging system using multiple stereo cameras. *Journal of Plastic, Reconstructive and Aesthetic Surgery*, 64(5), 2011.

[204] Maurice Y. Nahabedian and Gregory Galdino. Symmetrical breast reconstruction: Is there a role for three-dimensional digital photography? *Plastic and Reconstructive Surgery*, 112(6):1582–1590, 2003.

[205] Laszlo Kovacs, Alexander Yassouridis, Alexander Zimmermann, Gernot Brockmann, Antonia Wöhnl, Matthias Blaschke, Maximilian Eder, Katja Schwenzer-Zimmerer, Robert Rosenberg, Nikolaos A. Papadopulos, and Edgar Biemer. Optimization of 3-Dimensional Imag-

ing of the Breast Region With 3-Dimensional Laser Scanners. *Annals of Plastic Surgery*, 56(3):229–236, 2006.

[206] Laszlo Kovacs, Maximilian Eder, Regina Hollweck, Alexander Zimmermann, Markus Settles, Armin Schneider, Kristian Udosic, Katja Schwenzer-Zimmerer, Nikolaos A Papadopulos, and Edgar Biemer. New Aspects of Breast Volume Measurement Using 3-Dimensional Surface Imaging. *Annals of Plastic Surgery*, 57(6):602–610, 2006.

[207] Laszlo Kovacs, Maximilian Eder, Regina Hollweck, Alexander Zimmermann, Markus Settles, Armin Schneider, Matthias Endlich, Andreas Mueller, Katja Schwenzer-Zimmerer, Nikolaos A. Papadopulos, and Edgar Biemer. Comparison between breast volume measurement using 3D surface imaging and classical techniques. *Breast*, 16(2):137–145, 2007.

[208] Martin C. Koch, Boris Adamietz, Sebastian M. Jud, Peter A. Fasching, Lothar Haeberle, Stefan Karbacher, Klaus Veit, Ruediger Schulz-Wendtland, Michael Uder, Matthias W. Beckmann, Mayada R. Bani, Katharina Heusinger, Christian R. Loehberg, and Alexander Cavallaro. Breast volumetry using a three-dimensional surface assessment technique. *Aesthetic Plastic Surgery*, 35(5):847–855, 2011.

[209] J. Grant Thomson, Yuen Jong Liu, Richard J. Restifo, Brian D. Rinker, and Andrew Reis. Surface area measurement of the female breast: Phase I. validation of a novel optical technique. *Plastic and Reconstructive Surgery*, 123(5):1588–1596, 2009.

[210] Susan C Kuzminsky and Megan S Gardiner. Three-dimensional laser scanning: potential uses for museum conservation and scientific research. *Journal of Archaeological Science*, 39(8):2744–2751, 2012.

[211] Ametek. HandySCAN 3D Technical Specifications, 2002.

[212] Artec3D. Artec Leo Technical Specifications, 2022.

[213] Di Yang, Dayong Qiao, and Changfeng Xia. Curved light surface model for calibration of a structured light 3D modeling system based on striped patterns. *Optics Express*, 28(22):33240, 2020.

[214] Song Zhang. High-speed 3D shape measurement with structured light methods: A review. *Optics and Lasers in Engineering*, 106:119–131, 2018.

[215] Stefan A Carp, Tina Kauffman, Qianqian Fang, Elizabeth Rafferty, Richard Moore, Daniel Kopans, and David Boas. Compression-induced changes in the physiological state of the breast as observed through frequency domain photon migration measurements. *Journal of Biomedical Optics*, 11(6):64016, 2006.

[216] S A Carp, J Selb, Q Fang, R Moore, D B Kopans, E Rafferty, and D A Boas. Dynamic functional and mechanical response of breast tissue to compression. *Optics Express*, 16(20):16064, sep 2008.

[217] Stefan A Carp, Amir Y Sajjadi, Christy M Wanyo, Qianqian Fang, Michelle C Specht, Lidia Schapira, Beverly Moy, Aditya Bardia, David A Boas, and Steven J Isakoff. Hemodynamic signature of breast cancer under fractional mammographic compression using a dynamic diffuse optical tomography system. *Biomedical Optics Express*, 4(12):2911, dec 2013.

[218] Bernhard B Zimmermann, Qianqian Fang, David A Boas, and Stefan A Carp. Frequency domain near-infrared multiwavelength imager design using high-speed, direct analog-to-digital conversion. *Journal of Biomedical Optics*, 21(1):1–8, 2016.

[219] Seiji Inokuchi, K Sato, and F Matsuda. Range-imaging system for 3-D object recognition. In *Proceedings of the International Conference on Pattern Recognition*, pages 806–808, 1984.

[220] Seppe Sels, Bart Ribbens, Steve Vanlanduit, and Rudi Penne. Camera Calibration Using Gray Code. *Sensors*, 19(2), 2019.

[221] Daniel Moreno and Gabriel Taubin. Scan3d-Capture, 2012.

[222] Yi Xu and Daniel G. Aliaga. Robust pixel classification for 3D modeling with structured light. *Proceedings - Graphics Interface*, pages 233–240, 2007.

[223] Z Zhang. A flexible new technique for camera calibration. *IEEE Transactions on Pattern Analysis and Machine Intelligence*, 22(11):1330–1334, nov 2000.

[224] Jean-Yves Bouguet. *Camera calibration tool box for matlab*. Natick, Massachusetts, United State, 2004.

[225] W. Lingle, B. J. Erickson, M. L. Zuley, R. Jarosz, E. Bonaccio, J. Filippini, and N. Gruszauskas. Radiology Data from The Cancer Genome Atlas Breast Invasive Carcinoma [TCGA-BRCA] collection., 2016.

[226] Kenneth Clark, Bruce Vendt, Kirk Smith, John Freymann, Justin Kirby, Paul Koppel, Stephen Moore, Stanley Phillips, David Maffitt, Michael Pringle, Lawrence Tarbox, and Fred Prior. The cancer imaging archive (TCIA): Maintaining and operating a public information repository. *Journal of Digital Imaging*, 26(6):1045–1057, 2013.

[227] Paul A. Yushkevich, Joseph Piven, Heather Cody Hazlett, Rachel Gimpel Smith, Sean Ho, James C. Gee, and Guido Gerig. User-guided 3D active contour segmentation of anatomical structures: Significantly improved efficiency and reliability. *NeuroImage*, 31(3):1116–1128, 2006.

[228] François Pomerleau, Francis Colas, Roland Siegwart, Stéphane Magnenat, François Pomerleau, Francis Colas, Roland Siegwart, Stéphane Magnenat, Comparing Icp, and Francis Colas Roland. Comparing ICP variants on real-world data sets Open-source library and experimental protocol To cite this version : HAL Id : hal-01143458 Comparing ICP Variants on Real-World Data Sets. *Autonomous Robots*, 34(3):133–148, 2013.

[229] Radu Bogdan Rusu, Zoltan Csaba Marton, Nico Blodow, Mihai Dolha, and Michael Beetz. Towards 3D Point cloud based object maps for household environments. *Robotics and Autonomous Systems*, 56(11):927–941, 2008.

[230] Nina Amenta, Marshall Bern, and Manolis Kamvysselis. A New Voronoi-Based Surface Reconstruction Algorithm. In *Proceedings of the 25th Annual Conference on Computer Graphics and Interactive Techniques*, SIGGRAPH '98, pages 415–421, New York, NY, USA, 1998. Association for Computing Machinery.

[231] Per Christian Hansen. Analysis of Discrete Ill-Posed Problems by Means of the L-Curve. *SIAM Review*, 34(4):561–580, 1992.

[232] Marta Pinto, Ruby Egging, Alejandro Rodríguez-Ruiz, Koen Michielsen, and Ioannis Sechopoulos. Compressed breast shape characterization and modelling during digital breast tomosynthesis using 3D stereoscopic surface cameras. In *15th International Workshop on Breast Imaging*, page 38, 2020.

[233] Jeremy C Hebden, Adam Gibson, Rozarina Md Yusof, Nick Everdell, Elizabeth M C Hillman, David T Delpy, Simon R Arridge, Topun Austin, Judith H Meek, and John S Wyatt. Three-dimensional optical tomography of the premature infant brain. *Physics in Medicine and Biology*, 47(23):4155–4166, 2002.

[234] Arno Villringer and Britton Chance. Non-invasive optical spectroscopy and imaging of human brain function. *Trends in Neurosciences*, 20(10):435–442, 1997.

[235] Albert E Cerussi, Robert Warren, Brian Hill, Darren Roblyer, Anais Leproux, Amanda F Durkin, Thomas D O'Sullivan, Sam Keene, Hosain Haghany, Timothy Quang, William M Mantulin, and Bruce J Tromberg. Tissue phantoms in multicenter clinical trials for diffuse optical technologies. *Biomedical optics express*, 3(5):966–971, may 2012.

[236] Phuong Diep, Sanjana Pannem, Jordan Sweer, Justine Lo, Michael Snyder, Gabriella Stueber, Yanyu Zhao, Syeda Tabassum, Raeef Istfan, Junjie Wu, Shyamsunder Erramilli, and Darren Roblyer. Three-dimensional printed optical phantoms with customized absorption and scattering properties. *Biomedical optics express*, 6(11):4212–4220, oct 2015.